Model Predictive Control for Robust Power and Thermal Management of Connected and Electrified Vehicles

by

Qiuhao Hu

A dissertation submitted in partial fulfillment
of the requirements for the degree of
Doctor of Philosophy
(Naval Architecture and Marine Engineering)
in The University of Michigan
2023

Doctoral Committee:

Professor Jing Sun, Chair
Professor Heath Hofmann
Professor Ilya Kolmanovsky
Assistant Research Scientist Mohammad Reza Amini
Julia Buckland Seeds, Ford Motor Company
Ashley Wiese, Ford Motor Company

Qiuhao Hu

qhhu@umich.edu

ORCID iD: 0000-0003-2491-6956

To my mother, Yaqin Qiu

ACKNOWLEDGEMENTS

I would like to express my deepest gratitude to many individuals who helped me during my Ph.D. life, and this dissertation will not be possible without their generous efforts.

First of all, I'm extremely grateful to my advisor and chair of my committee, Prof. Jing Sun, for her invaluable patience and feedback. She is a really brilliant person and a respected expert in broad fields. I am glad to have the opportunity joining her group and it is my honor to work with her. Over the past five years, she provided me with extensive knowledge and expertise, which not only deepened my understanding in my research area, but also built up my academic skills and integrity. In my work and life, I always have her support, which helps me through the most challenging time. Every thing I learned from her will be my lifelong wealth and inspire me to pursue higher targets in my future life.

Next, I wish to extend special thanks to Prof. Ilya Kolmanovsky and Dr. Reza Amini, who provided me with many valuable advises and guidance during my Ph.D. program. I learned a lot from them of being a passionate and independent researcher. I would like to sincerely express my appreciation to my collaborators from industry, Dr. Julia Buckland Seeds and Dr. Ashley Wiese. They are both considerate and responsible people, who offered me valuable opportunities to work in industry. These experience broaden my horizon and shaped me to think the problem from a practical point of view.

Furthermore, I would like to thank every member in Race Lab for their support

and encouragement. Particularly, I would like to thank Dr. Hao Wang, Dr. Kai Wu, and Dr. Ziyou Song, who offer me a lot help, particularly at the beginning stage of my Ph.D. life, which help me adapt to the new environment.

Finally, I would like to express my deepest gratitude to my mother, who always encourages me to be a better person and pursue my dream.

TABLE OF CONTENTS

LIST OF FIGURES

Figure

LIST OF TABLES

Table

LIST OF APPENDICES

Appendix

LIST OF ABBREVIATIONS

BSFC Brake Specific Fuel Consumption

BN Bayesian Network

CAV Connected and Automated Vehicle

COP Coefficient of Performance

DP Dynamic Programming

EMS Energy Management Strategy

EV Electric Vehicle

HEV Hybrid Electric Vehicle

HVAC Ventilation and Air Conditioning

iPTM Integrated Power and Thermal Management

MPC Model Predictive Control

MH-MPC Multi-horizon Model Predictive Control

NEDC New European Driving Cycle

NN Neural Network

OHE Out heat exchanger

OPP Optimal Operating Points

PMP Pontryagin's Minimum Principle

RPM Round per Minute

SOC State of Charge

TMS Thermal Management System

UDDS Urban Dynamometer Driving Schedule

V2I/V2V Vehicle-to-Infrastructure/Vehicle

ABSTRACT

Integrated power and thermal management (iPTM) of electrified vehicles, such as hybrid electric vehicles (HEVs) and electric vehicles (EVs), can significantly improve their energy efficiency. In addition, with the emergence of connected vehicles (CVs), new opportunities open up for vehicle enhanced situational awareness, including the growing availability of preview/forecast of future vehicle speed and load. Model predictive control (MPC) is appealing for iPTM because of its ability to handle state and input constraints, approximate optimal control, and incorporate preview information. In the application of MPC to iPTM, however, different timescales of power and thermal subsystems present special challenges. Specifically, with the conventional MPC, fast sampling required by the fast dynamics and the long prediction horizon dictated by the slow dynamics lead to a large computational effort, which is difficult to accommodate in computationally constrained automotive processors. To this end, this dissertation develops novel multi-horizon MPC-based iPTM approaches for connected and electrified vehicles.

The proposed multi-horizon model-predictive control (MH-MPC)leverages multi-fidelity models and preview information over a short receding and a long shrinking horizon to balance a trade-off between performance and computational efficiency. Compared to the conventional MPC-based approaches with a short prediction horizon and terminal cost, the MH-MPC improves fuel/energy efficiency to a level comparable to Dynamic Programming (DP) while still being computationally affordable.

A statistical sensitivity analysis over real-world city driving cycles is conducted to demonstrate the robustness of MH-MPC to moderate levels of uncertainty in the long-term preview.

To complement the proposed MH-MPC approach. A data-driven multi-range vehicle speed prediction strategy is developed for arterial corridors with signalized intersections, providing vehicle speed prediction for short, medium, and long ranges. The short-range prediction is informed through V2V/I communications. The medium-range prediction is realized using a Neural Network (NN), while the long-range speed profile is predicted based on a Bayesian Network (BN). The predictions are incorporated into MH-MPC for iPTM of connected vehicles, and energy efficiency improvement is observed.

Moreover, an integrated spatio-temporal framework is proposed in this dissertation for multi-range traction power and speed prediction for CVs. The proposed framework leverages the historical and real-time data to predict traction loads. The spatio-temporal framework is combined with MPC-based iPTM to investigate the impact of uncertainties for a commercial electric vehicle. To improve the robustness of the algorithm in the presence of uncertainties, a location-dependent constraint strategy is proposed and integrated into the MPC-based thermal management strategy. The simulation results show a reduction of energy consumption for thermal management without degrading the capacity of enforcing the thermal constraints.

Finally, the dissertation explores the synergy between battery thermal management and battery charging in an EV. An MPC-based approach is applied to minimize the energy used for battery thermal management and optimize fast charging time. An adaptive strategy is developed to adjust the weight of the two competing objectives in the MPC cost function to manage the trade-off between energy consumption and charging time. The sensitivity of the proposed MPC-based battery thermal management (BTM) strategy to uncertainties in the fast charging station availability is also

investigated. For a commercial EV model, the simulation results show a decrease in the charging time achieved by optimally performing BTM at the cost of negligibly higher battery thermal management energy usage.

CHAPTER I

Introduction

1.1 Background & Motivation

1.1.1 Energy Management Strategy of HEVs and EVs

In the last several decades, concerns about the energy crisis and climate change have driven the development of vehicle powertrain technologies, among which hybrid electric vehicles (HEVs) and battery electric vehicles (EVs) have become increasingly prominent in the marketplace [1, 2]. Compared with conventional internal combustion engine vehicles, HEVs provide a reduction in fuel consumption and air pollution emissions, because of the capacity to recuperate a part of kinetic energy in braking phases, and due to an additional resource being available to more efficiently meet the vehicle power demands [3, 4]. On the other hand, EVs mainly offer the advantages of zero emissions and reducing greenhouse gases, e.g., CO_2 [5], and lower maintenance and operating costs [6].

For HEVs, achieving the aforementioned benefits crucially rely on the proper design of energy management strategies (EMS). For different HEV architectures, their EMS can be generally thought of as providing power/torque split selection, which determines the power flow from different resources (e.g., engine and electric motor) to satisfy the load requirement and improve the overall energy efficiency

of the vehicle [7, 8]. The existing EMS are based on either heuristic methods or optimization-based methods. The heuristic strategies are typically formalized as Boolean or fuzzy rules [9, 10], where no future driving information is required. The optimization-based strategies, on the other hand, can be classified into (i) offline approaches, e.g. Dynamic Programming (DP) [11, 12] and Pontryagin's Maximum Principle (PMP) [8, 13, 14], and (ii) online approaches, e.g., model predictive control (MPC) [15, 16, 17, 18]. The optimization-based strategies typically rely on future vehicle preview information, including vehicle speed, traction power demand, and thermal loads. This preview information has often been the missing piece for implementing optimization-based EMS.

1.1.2 Connected Vehicles Technologies Enabled Vehicle Speed Prediction

The capability of predicting future vehicle speed enables also a preview of traction power demand and some of the thermal loads (e.g., electric battery heat load) needed by EMS of electrified vehicles [19, 20, 21, 22]. The prediction of traction power demand and thermal loads for vehicles operating in highly dynamic and uncertain traffic environments is challenging and can be subject to large uncertainties. With the emergence of connected vehicles (CVs), new opportunities have been opened up for enhanced situational awareness [23, 24] through onboard sensing and data exchanges with surrounding vehicles and infrastructures.

Many CV-related technologies, such as eco-driving [19], platooning [25], cooperative adaptive cruise control [24], and eco-cooling/heating [26, 27], can benefit from look-ahead information beyond the range of their onboard sensors. When assessing the energy efficiency of CVs, this look-ahead information has often been assumed either to be known a priori for a given driving cycle or be made available over a short-range using learning-based [16, 28] or model-based techniques [29, 30, 31]. While some studies have investigated long-range vehicle speed prediction, those results have

mainly focused on the average vehicle speed on highways [32, 33], over road segments [34, 35, 36] without intersections or at the city-scale traffic level [37], at a fixed location [38], or for a single private vehicle [39].

Achieving reliable speed and load predictions for CVs, especially in arterial corridors with signalized intersections, is challenging due to the (i) highly dynamic and stochastic nature of traffic, (ii) wide range of dynamic characteristics of CVs and associated systems, and (iii) non-uniform distribution of CVs and varying levels of availability of infrastructure-based sensors. In addition, the processes in CVs evolve over timescales spanning from milliseconds (e.g., onboard planning and computation), to seconds (e.g., traction power), to minutes (e.g., thermal loads), and potentially hours (e.g., battery charging) [40, 41, 42]. Hence preview information over different prediction horizons with different levels of requirements for fidelity and accuracy is needed for energy and mobility optimization.

1.1.3 Integrated Power and Thermal Management for HEVs and EVs

Although promising benefits have been reported using various EMS, most of the existing work has been based on the assumption that vehicular power and thermal systems (e.g., engine, battery, and electric motor) operate at normal temperature and their thermal responses are managed by separate thermal management systems. In [43, 44, 45], it has been demonstrated that the thermal management of HEVs, including engine cooling, cabin and battery heating/cooling, and aftertreatment system, has a significant impact on the overall vehicle energy efficiency. For example, at cold ambient temperature, the engine temperature drops quickly when the vehicle operates in the electric mode (i.e., engine off mode) and the decreased temperature can degrade the engine performance once it is turned on [46, 47]. Furthermore, the cold engine and ambient temperatures affect the aftertreatment system, leading to an interaction between fuel economy and emission reduction at low ambient temper-

atures [48].

Thermal management is also of great importance for EVs, as the thermal management system (TMS) consumes a considerable amount of energy and thus, reduces the driving range of the vehicle [49, 50, 51, 52]. The EV TMS includes heating/cooling, ventilation, and air conditioning systems that maintain components onboard in their desired and safe thermal states. Among them, cabin and battery temperature regulation is crucial for EVs, as the battery is subject to performance degradation or lifespan reduction when operating outside their desired temperature window, while over/under heating and cooling of the cabin impact passengers' comfort and customer satisfaction. The study in [49] shows that the driving range reduction of Nissan Leaf over the New European driving cycle (NEDC) can be up to 9% and 22% under cooling and heating scenarios, respectively, due to the operation of the TMS system. According to the test conducted at Argonne National Laboratory [53], the use of a ventilation and air conditioning system (HVAC) can reduce the driving range up to 59%.

While efficient thermal management has a significant impact on the energy efficiency of HEVs and EVs, the integrated power and thermal management (iPTM) has been the subject of only a few recent studies [54, 55, 56, 57, 58, 59]. In these articles, the conventional EMS designed for normal operating conditions is typically extended to handle iPTM with additional thermal states. In [54], the influence of the cold start on fuel consumption was studied using DP. In [60], a thermal state representing the engine temperature was considered, and PMP was applied to a two-state model. Although DP can provide a global optimal solution for thermal management, its high computational cost and the requirement of accurate vehicle speed prediction limit its practical use in vehicles. PMP-based approaches, on the other hand, reduce the computational demand as compared to DP and can be implemented online with real-time adaptation. PMP was applied in [57] to satisfy the emission requirements

and provide a sub-optimal solution for fuel consumption. In [61], PMP was applied to minimize energy consumption while maintaining battery temperature within a desired range. Although benefits have been reported using PMP, deriving solutions based on rigorous/non-heuristic application of PMP to systems with state constraints is challenging from both theoretical and computational standpoints.

Optimizing vehicle charging performance, particularly under fast charging conditions, is another area that has not been fully explored. Although the battery charging performance is much influenced by the battery's thermal state, only a few recent works aim to improve the battery's fast charging performance by exploiting the coupling of battery charging power and thermal behavior [62, 63]. In [62], an optimal BTM was developed to reduce the charging time in cold ambient. The simulation results illustrated that for a cold battery, performing thermal pre-conditioning for the battery prior to charging increases the charging power, and thus reduces the charging time. Moreover, the optimization results presented in [62] reveal a trade-off among traveling time, energy efficiency, and charging cost. In [63], an optimal scheduling strategy was proposed for charging an EV to minimize the charging cost and charging time, by leveraging vehicle-to-grid connectivity. The charging power degradation caused by low ambient temperature was also considered in [63] to avoid a lower final state-of-charge (SOC). Unlike cold ambient conditions, which restrict the battery charging power and thus extend the charging time, hot ambient conditions reduce the heat rejection capacity of the battery and its cooling system. If the heat generation due to fast charging exceeds this reduced cooling capacity, the charging rate has to be throttled to keep the battery within acceptable temperature limits, thereby slowing charging and forcing trade-offs between charging time and target battery SOC.

1.1.4 Model Predictive Control for iPTM of HEVs and EVs

MPC is appealing for iPTM because of its ability to handle state and input constraints, approximate optimal control, and incorporate preview information. In [64], MPC was applied to minimize the energy consumption for battery cooling. To reduce the loss of optimality due to the finite prediction horizon, the terminal cost was computed offline through stochastic dynamic programming to approximate the cost-to-go from the end of the prediction horizon to infinity. The use of such terminal cost improved energy efficiency without increasing computational load. In [65], a stochastic MPC was applied to battery thermal management. The strategy exploited a Markov chain representation of future vehicle speed and acceleration inferred using data from standard driving cycles. Energy efficiency improvement was shown as compared to the alternative frozen-in-time prediction of vehicle speed and acceleration. However, the use of a short prediction horizon (3 sec) was necessary to make the problem computationally tractable. Given the slow dynamics of thermal systems, it was argued that the use of a longer horizon has the potential to provide larger improvement [66, 67]. MPC was also used in [26, 68, 69] to leverage the vehicle speed preview to minimize the energy consumption of the climate control system. In these studies, the energy saving was achieved mainly by leveraging the inherent coupling between the onboard HVAC system efficiency and the vehicle speed, as the increase in the ram air flow speed facilitates the heat exchange in the HVAC condenser.

Although some benefits have been reported by applying MPC to iPTM of HEVs and EVs, there are still two main challenges:

- the coupling between power and thermal dynamics that respond over different timescales,
- uncertainties associated with vehicle speed forecast that can influence the MPC performance unfavorably.

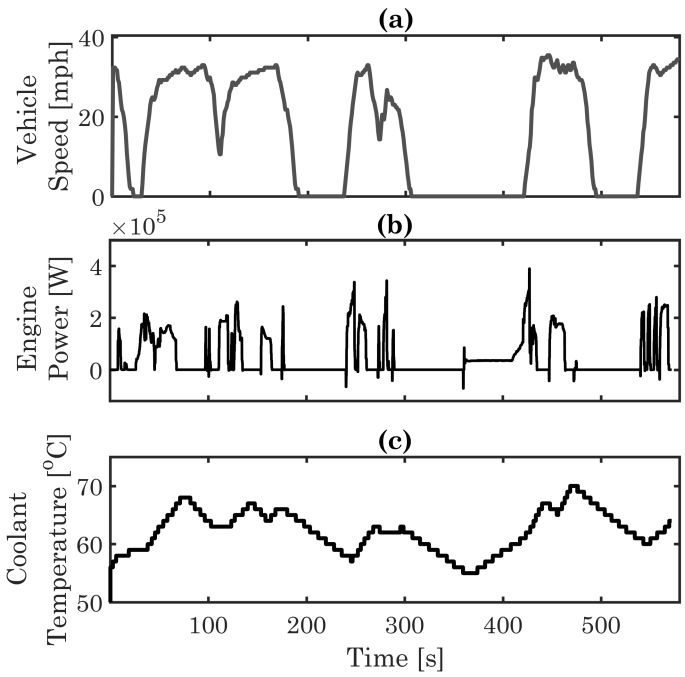

Figure 1.1: Time-scale separation between power and thermal systems in an HEV: (a) vehicle speed, (b) engine power, and (c) engine coolant temperature. Data collected from a test HEV.

Fig. 1.1 highlights the timescale separation between power and thermal systems of an HEV using the data collected from a test vehicle. As can be seen, the response of engine power (Fig. 1.1-(b)) is relatively fast, e.g., within $1 - 3$ s time constant. On the other hand, the engine coolant temperature (Fig. 1.1-(c)) which represents the thermal dynamics of the combustion engine, responds much slower with a time constant in the order of 30 s. Despite their different response timescales, the power and thermal dynamics are strongly coupled. Fig. 1.1 shows that when the engine is used to meet the driver traction power demand, the engine coolant temperature increases simultaneously.

When MPC is applied to such multi-timescale systems, the slower dynamics often dictate that a relatively long prediction horizon be used and the fast dynamics define the minimum sampling rate. This combination leads to a large computational footprint. To address that issue, a commonly used approach is to exploit the singular

perturbation theory [70], in which a system with explicit timescale separation in the dynamics is decomposed into two reduced-order subsystems with different timescales, see [71, 72, 73, 74]. "Fast" and "slow" MPCs are designed and applied to control fast and slow dynamics, respectively.

An alternative approach for dealing with multi-timescale systems is hierarchical MPC (H-MPC) [67, 75, 76, 77, 78, 79]. Unlike the decentralized fast-slow MPC approach based on the singular perturbation theory that does not necessarily require communication between the slow and fast MPCs [72], an H-MPC computes the optimal reference values for the "slow" dynamics over a relatively long prediction horizon. Then, a tracking problem is solved over a much shorter prediction horizon to track the planned references and compute the control commands. For example in [67, 75], an H-MPC implements an economic MPC in the top, scheduling-layer, with a long prediction horizon and a long sampling period, and a tracking MPC is used in the lower, piloting layer. Both scheduling and piloting MPCs were implemented using a receding horizon scheme. Despite the relatively long prediction horizon considered at the top layer of H-MPC, satisfying the terminal constraint (e.g., charge-sustaining condition) at the end of the operation cannot be guaranteed. Such a design requirement is of great importance for iPTM.

As an example, consider an energy management strategy for hybrid electric vehicles (HEVs), where the objective is to minimize fuel consumption over the entire trip, subject to a battery charge sustainability constraint that needs to be enforced at the end of the trip. If a conventional receding horizon MPC with a finite horizon is used for energy management of HEVs, this battery charge sustainability constraint is often enforced by adding a terminal penalty on the deviation of the battery state-of-charge (SOC) from its reference value—which is often set to be a constant value—at the end of the prediction horizon [18, 80]. Given the finite horizon of the MPC, such a terminal penalty in the cost may limit the practical range of the battery SOC,

forcing the HEV powertrain to operate in a narrow and less efficient region [81]. This problem is common in mission-based applications, where a specific mission/task needs to be accomplished over a finite time duration while having limited onboard energy resources. The multi-timescale dynamics and mission-based nature of an iPTM operation motivate the development of a novel optimization-based method to facilitate energy management, which is one of the main focuses of this study.

Another challenge of iPTM is due to the uncertainties associated with vehicle speed forecasts. As discussed above, the relatively slow dynamics of thermal systems call for a longer prediction horizon to achieve the desired performance, which typically leads to larger uncertainty in predicting the vehicle speed over the prediction horizon. In [66, 67], it has been demonstrated that errors in vehicle speed prediction can be detrimental to achieving the optimal performance of the power and thermal management, as the errors lead to extra energy consumption or violation of battery temperature constraint. Therefore, assessing and improving the robustness of the MPC-based iPTM with respect to the uncertainties associated with vehicle speed prediction is another focus of this dissertation.

1.2 Main Contributions

This dissertation aims at bridging the research gap in the power and thermal management design of HEVs and EVs for enhanced energy efficiency. The main contributions are summarized in the following:

1. A novel multi-horizon MPC (MH-MPC) is developed for coupled power and thermal systems and demonstrated for iPTM of HEVs operating in a connected traffic environment. The MH-MPC exploits multi-range prediction and optimization over a short receding horizon and a long shrinking horizon with different accuracies and resolutions. Simulation results of applying MH-MPC to a

power-split HEV demonstrated improved performance as compared to conventional MPC with a battery charge sustaining terminal penalty.

2. A data-driven multi-range vehicle speed prediction strategy is proposed and demonstrated for urban corridors with signalized intersections. The proposed strategy exploits historical traffic data collected from connected vehicles to provide a prediction of vehicle speed over short-, medium- and long-range. The effectiveness of the proposed vehicle speed prediction framework was demonstrated by exploiting it for vehicle speed preview in the MH-MPC scheme used for HEV iPTM. The simulation results show that by incorporating the medium- and long-range speed preview, the MH-MPC achieves a fuel consumption close to the offline Dynamic Programming solution.

3. The MPC-based approach is applied to iPTM of EVs for increasing the driving range and enforcing the thermal constraints. The key features in vehicle speed and vehicle traction power prediction that have a significant impact on the MPC-based iPTM performance are identified. The proposed strategy is evaluated using real-world drive cycles and a location-dependent thermal constraint handling strategy is developed to improve the robustness of the controller in presence of uncertainties.

4. The MPC-based iPTM is expanded to optimize charging time and energy consumption for battery thermal management of EVs. The proposed method achieves a target battery state-of-charge (SOC) within the required time while enforcing the power, and thermal constraints of power and thermal loops. Leveraging the preview information, the simulation results show that the proposed MPC-based strategy can reduce the charging time via pre-cooling the battery before the start of the charging event. Moreover, an adaptive strategy is developed for adjusting the weight on the charging time in the MPC stage cost to

manage the trade-off between charging time and battery thermal management energy consumption.

1.3 Dissertation Outline

The dissertation is organized as follows:

In Chapter II, the details of the models of the thermal and power subsystems, representative of an HEV and an EV used in this research, are described. The models of the HEV powertrain system developed based on a power-split HEV configuration will be used in Chapter III and IV, and EV models will be used in Chapter V and Chapter VI.

In Chapter III, a novel multi-horizon MPC (MH-MPC) strategy is proposed for the iPTM of HEVs operating in a connected traffic environment. The MH-MPC is compared with a conventional MPC to show the benefits of the proposed methods from the perspectives of energy efficiency and computational footprint. Moreover, we present the sensitivity analysis of the proposed MH-MPC to uncertainties in vehicle speed preview and discuss the MH-MPC robustness.

In Chapter IV, the data-driven multi-range vehicle speed prediction strategies are introduced, including the long-range speed prediction based on the Bayesian network and the medium-range prediction based on Neural Network. Next, the MPC algorithm developed for minimizing the fuel consumption of HEVs is presented and the simulation results of iPTM that incorporate the proposed speed prediction strategy are reported.

In Chapter V, the MPC-based iPTM is expanded to EVs for improving energy efficiency and enforcing the constraints in power and thermal loops. The MPC results with different prediction horizons are analyzed to identify the key speed/traffic features. Then, the impact of uncertainties in the speed predictions on the optimal iPTM performance is quantified. Finally, the developed MPC-based thermal man-

agement strategy is evaluated using real-world traffic data, and a location-dependent constraint strategy handling is proposed to improve the robustness of the algorithm against the uncertainties in speed preview.

In Chapter VI, a multi-objective MPC strategy is proposed to minimize charging time and energy consumption for battery thermal management of an EV. A sensitivity analysis is conducted to evaluate the performance of the controller, and an adaptive strategy is proposed for adjusting the weight in the cost function to manage the trade-off between charging time and battery thermal management energy consumption. Last, the impact of uncertainty is studied to evaluate the robustness of the proposed methods.

Chapter VII provides conclusions and presents future research directions.

CHAPTER II

Power and Thermal Models of Hybrid and Electric Vehicle

In this Chapter, the models of the thermal and power subsystems, representative of an HEV and EV used in this research, are described. The HEV powertrain system considered in this dissertation is based on a power-split Toyota Prius, and the EV is based on a commercial electric vehicle. While HEV and EV have different powertrain and thermal management systems, the vehicle traction power model, battery power and thermal model, and cabin thermal model are applicable to both HEV and EV.

2.1 Models Applicable to HEV and EV

2.1.1 Vehicle Traction Power Model

The vehicle traction power (P_{trac}) is determined by

$$P_{trac} = V_{veh}(m\dot{V}_{veh} + F_r + F_a), \tag{2.1}$$

where V_{veh}, m, F_r and F_a represent the vehicle speed, mass, the rolling and aerodynamic resistance force, respectively, which are calculated as follows:

$$F_r = C_r m g, \tag{2.2}$$

$$F_a = 0.5 \rho A_f C_d V_{veh}^2, \tag{2.3}$$

where C_r and C_d are the coefficient of rolling and aerodynamic resistance, A_f is the frontal area of the vehicle, and ρ is the air density. The vehicle is assumed to be on a flat road and the effects of road grade and wind are not considered.

2.1.2 Battery Power-Balance and Thermal Models

For HEV and EV, the battery provides the power for traction (P_{bat}^{trac}) and auxiliary systems (P_{bat}^{aux}):

$$P_{bat} = P_{bat}^{trac} + P_{bat}^{aux}, \tag{2.4}$$

where P_{bat} is the total battery power. The battery state of charge (SOC) dynamics are represented using an equivalent circuit model:

$$\dot{SOC}(t) = f_{SOC}(t) = -\frac{I_{bat}}{C_{bat}} = -\frac{U_{oc} - \sqrt{U_{oc}^2 - 4 R_{int} P_{bat}}}{2 R_{int} C_{bat}}, \tag{2.5}$$

where t denotes time while C_{bat}, R_{int}, I_{bat}, and U_{oc} are the capacity, internal resistance, battery current, and open-circuit voltage of the battery, respectively. Besides, the battery heat generation is mainly attributed to the internal resistance and is given by

$$\dot{Q}_{gen} = I_{bat}^2 R_{int}. \tag{2.6}$$

The battery is modeled as a lumped mass and the dynamic of temperature, T_{bat}, is expressed as

$$\dot{T}_{bat} = f_{bat}(t) = \frac{1}{m_{bat}C_{bat}}(\dot{Q}_{gen} + \dot{Q}_{amb} - \dot{Q}_{bat}), \tag{2.7}$$

where m_{bat}, C_{bat} are the thermal mass and specific heat capacity of battery, respectively, and $\dot{Q}_{amb}$ is the rate of the heat dissipated to the ambient by air convection, which is proportional to the temperature difference between battery and ambient.

2.1.3 Cabin Thermal Model

The cabin is modeled as a lumped mass so that the cabin temperature dynamics are expressed as

$$\begin{aligned} \dot{T}_{cab} &= f_{cab}(t) \\ &= \frac{1}{m_{cab}C_{cab}}(\dot{Q}_{sun} + \dot{Q}_{cov} + \dot{Q}_{ven} + \dot{Q}_{met} - \dot{Q}_{cab}), \end{aligned} \tag{2.8}$$

where m_{cab}, C_{cab} are the thermal mass and specific heat capacity of cabin, respectively. $\dot{Q}_{sun}$, $\dot{Q}_{cov}$, $\dot{Q}_{ven}$, and $\dot{Q}_{met}$ are the heat transfer rate of sun radiation, air convection, air ventilation, and human metabolic activities, respectively. The detailed formulation of each heat source term in (2.8) can be found in [82].

2.2 HEV Power and Thermal Models

2.2.1 Schematic of HEV Power and Thermal Systems

The HEV powertrain system considered in this paper is based on a power-split Toyota Prius. The overall schematic of the power and thermal loops of the HEV is shown in Fig. 2.1. The two states of interest, which represent two energy storages within HEV, are battery SOC and engine coolant temperature (T_{cl}). The physics-based models of SOC and T_{cl} dynamics are adopted from [43], where the power (SOC and fuel consumption rate $\dot{m}_{fuel}$) and thermal (T_{cl}) models were experimentally validated against the data collected from a Prius HEV MY 2017.

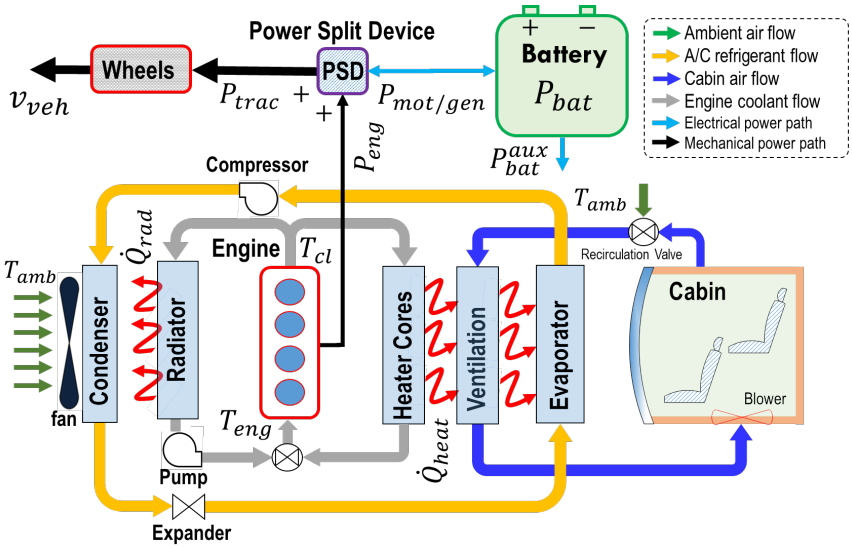

Figure 2.1: The schematic of a power-split HEV with power and thermal loops.

2.2.2 Engine Coolant Temperature Model

For a power-split HEV, the power provided by the battery (P_{bat}^{trac}) and internal combustion engine (P_{eng}) are blended to meet the traction power demand for driving:

$$P_{trac} = P_{bat}^{trac} + P_{eng}, \tag{2.9}$$

where the engine mechanical output power is determined by engine speed (ω_e) and torque (τ_e). The engine is assumed to follow the optimal operating points (OPP) line on engine brake specific fuel consumption (BSFC) is minimized [83]. The thermal dynamics of engine coolant are modeled based on the energy balance [47]:

$$\begin{aligned} \dot{T}_{cl}(t) &= f_{T_{cl}}(t) \\ &= \frac{1}{M_{eng}C_{eng}}(\dot{Q}_{fuel} - P_{eng} - \dot{Q}_{exh} - \dot{Q}_{air} - \dot{Q}_{heat}), \end{aligned} \tag{2.10}$$

where M_{eng} and C_{eng} are the equivalent thermal mass and the specific heat capacity of the engine cooling system, respectively. $\dot{Q}_{fuel}$, $\dot{Q}_{exh}$, $\dot{Q}_{air}$ and $\dot{Q}_{heat}$ represent the heat rate released from the combustion process, exchanged through exhaust gases,

dissipated by air convection, and delivered for cabin heating, respectively. In particular, $\dot{Q}_{fuel}$ is calculated using fuel consumption rate and the lower heating value (LHV) of the fuel:

$$\dot{Q}_{fuel} = LHV \cdot \dot{m}_{fuel}, \tag{2.11}$$

where $\dot{m}_{fuel}$ is the fuel consumption rate calculated as a function of engine speed, torque, and T_{cl}:

$$\dot{m}_{fuel}(\omega_e, \tau_e, T_{cl}) = \alpha(T_{cl}) \cdot f_{fuel}(\omega_e, \tau_e), \tag{2.12}$$

where $f_{fuel}(\omega_e, \tau_e)$ is the nominal fuel consumption rate and $\alpha(T_{cl})$ is a multiplier reflecting the fuel consumption sensitivity to the coolant temperature. These functions are adopted from Autonomie[1] software library for a power-split HEV, see [43] for more details. When T_{cl} is 60^oC, $\alpha = 1.03$ and decreases to $\alpha = 1$ at $T_{cl} = 100^oC$, at which point the engine is fully warmed up. When T_{cl} is less than 60^oC, α increases, reflecting the engine efficiency degradation at lower coolant and ambient temperatures. For instance, when T_{cl} decreases to 10^oC from 60^oC, α can increase by up to 50%. The experimental validation of the control-oriented models in (2.5) and (2.10) can be found in [43, 84].

2.3 Thermal Management System of an Electrical Vehicle

The power and thermal models of an EV are presented in this subsection. Fig. 2.2 depicts a schematic of the integrated thermal management system of an EV, which consists of the refrigerant loop, as well as cabin and battery cooling loops.

As presented in Fig. 2.2, the refrigerant absorbs heat from the battery and cabin

[1] Autonomie® is a MATLAB®/Simulink®-based system simulation tool for vehicle energy consumption and performance analysis developed by Argonne National Laboratory (ANL) [45].

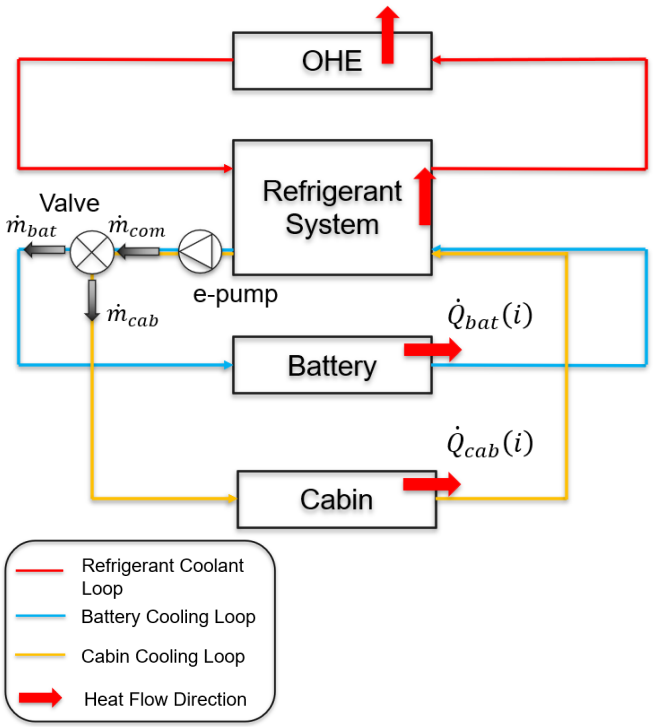

Figure 2.2: Schematic of integrated thermal management system of an EV.

coolant, while the out heat exchanger (OHE) dissipates the absorbed heat to the ambient. The battery and cabin coolant is circulated by an electric pump through the combined cabin and battery loops. Its mass flow rate is denoted by $\dot{m}_{com}$. The coolant is split into battery and cabin cooling loops by a three-way valve with mass flow rate of $\dot{m}_{bat}$ and $\dot{m}_{cab}$, respectively. The coolant flow rates follow the mass conservation law:

$$\dot{m}_{com} = \dot{m}_{bat} + \dot{m}_{cab}, \tag{2.13}$$

$$\dot{m}_{cab} = r\dot{Q}_{com}, \tag{2.14}$$

$$\dot{m}_{bat} = (1 - r)\dot{Q}_{com}, \tag{2.15}$$

where r is the split ratio of the coolant, which is controlled by the three-way valve. The cold coolant provides the cooling power to the battery ($\dot{Q}_{bat}$) and cabin ($\dot{Q}_{cab}$)

through their heat exchanges. The cooling power of each loop is determined by the following equations:

$$\dot{Q}_{bat} = \alpha(\dot{m}_{bat})(T_{bat} - T_{cl,ev}), \tag{2.16}$$

$$\dot{Q}_{cab} = \beta(\dot{m}_{cab})(T_{cab} - T_{cl,ev}), \tag{2.17}$$

where α and β are the heat exchange coefficients, which increase as the coolant flow rate increases. Besides, T_{bat}, T_{cab}, and $T_{cl,ev}$ are the temperature of battery, cabin and coolant of the EV cooling system. The cabin and battery cooling power can be controlled by the electric pump and three-way valve. The former adjusts $\dot{m}_{com}$ and the latter changes r.

The power consumption of the TMS (P_{sys}) is calculated as follows:

$$P_{sys} = \frac{\dot{Q}_{bat} + \dot{Q}_{cab}}{COP}, \tag{2.18}$$

where COP is the coefficient of performance describing the efficiency of the TMS, and P_{sys} includes the power consumed for compressor and electric pump. The representation of COP, as a function of the combined cooling power ($\dot{Q}_{bat} + \dot{Q}_{cab}$) is adopted from [85]. Based on this model COP decreases as the total cooling power increases.

CHAPTER III

Integrated Power and Thermal Management of CAV for Multi-Horizon Model Predictive Control

3.1 Problem Formulation

The integrated power and thermal management of electrified vehicles, including that of the combustion engine, battery, exhaust aftertreatment, and cabin temperature, has a significant impact on the overall fuel economy. This is especially true in cold and hot ambient conditions [45, 47, 86], where (i) the actuators used for thermal management (e.g, compressor, pumps, and fans) can consume a considerable amount of energy [84, 87], and (ii) the efficiencies of the vehicular power and thermal systems degrade outside of the optimal temperature range. For HEVs, thermal management priority varies as the ambient temperature changes. In cold ambient temperatures, cabin heating is the main thermal load. In hot ambient temperatures, on the other hand, thermal management of the engine, as well as cabin and battery cooling, contribute to the overall thermal loads within the vehicle.

In this chapter, the HEV is considered to operate at a cold ambient temperature of -10^oC, while the proposed methodology is applicable to hot ambient conditions with an appropriate adjustment in the problem formulation. The overall schematic of the power and thermal loops of the HEV is shown in Fig. 3.1. The objective of iPTM is

to minimize fuel consumption while enforcing the battery SOC and engine coolant temperature (T_{cl}) constraints in response to the traction and cabin heating demands. Moreover, there are typically terminal condition needs to be enforced to ensure a desired a final battery SOC. In this study, a charging sustainability condition is conducted, which requires the final battery SOC be close to the initial battery SOC. This condition is imposed mainly because of the following two reasons: i) the same energy is stored within the battery when comparing the fuel efficiency of different EMS, and ii) enough battery SOC is left when the vehicle starts the next trip.

In this section, we first evaluate a conventional MPC with a short receding horizon as the baseline approach. Then, motivated by the limitations of conventional MPC, the multi-horizon MPC is proposed. In all cases, the battery SOC and engine coolant temperature (T_{cl}) are considered as the system states, with battery power (P_{bat}) being the optimization variable.

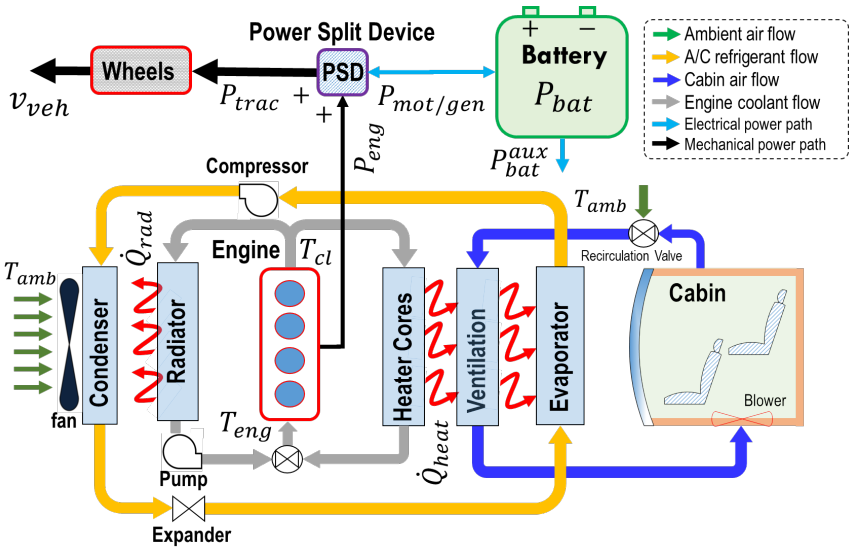

Figure 3.1: The schematic of a power-split HEV with power and thermal loops.

3.2 Conventional MPC for iPTM of HEVs

As presented in [18, 88], the conventional MPC-based strategy for energy management of HEVs is intended to minimize the fuel consumption over a finite prediction horizon, while enforcing the battery SOC charge sustaining constraint. TMS needs to consider additional constraints on the coolant temperature. Therefore, the discrete-time optimal control solved at each discrete time instant t is formulated as:

$$\begin{aligned}
\underset{P_{bat}(i)}{\arg\min} \quad & \sum_{i=t}^{t+H-1} \dot{m}_{fuel}(i)\delta t + \lambda\big(SOC(t+H) - SOC_r\big)^2, \\
\text{s.t.} \quad & SOC(i+1) = SOC(i) + \delta t \cdot f_{SOC}(i), \\
& T_{cl}(i+1) = T_{cl}(i) + \delta t \cdot f_{T_{cl}}(i), \\
& SOC_{min} \leq SOC(i) \leq SOC_{max}, \\
& T_{cl,min} \leq T_{cl}(i) \leq T_{cl,max}, \\
& T_{cl}(0) = T_{cl,init}, \quad SOC(0) = SOC_{init},
\end{aligned} \tag{3.1}$$

where H is the prediction horizon, δt is the discrete-time step, chosen as 1 s in our case studies. We used shorthand notations f_{SOC}, $f_{T_{cl}}$ for functions used in equations (2.5), (2.10) in the model described in Section 2.1. In the subsequent simulations, the initial conditions are $SOC_{init} = 0.6$ (60%), and $T_{cl,init} = 50^oC$, representative of a typical scenario where the engine is partially warmed-up. Note that we leave the treatment of cold-start to future work as it requires additional, specialized modeling and control strategies. The upper and lower bounds of SOC and T_{cl} are 0.3 and 0.8, 40^oC and 90^oC, respectively. Cabin heating system is treated as a constant thermal load, where the required heating power $P_{heat} = 1.5\ kW$ is assumed.

The weight in the quadratic penalty term is set to $\lambda = 3$ which promotes charge sustainability. This value has been chosen by trial and error. The reference value for the battery state-of-charge (SOC_r) is set to be the same as SOC_{init}. At each time step t, the optimization problem (3.2) is solved to determine the optimal battery

power ($P_{bat}(t)$), which informs the required engine power ($P_{eng}(t)$) based on (2.9). Additionally, it is assumed that the engine operates on the curve of optimal operation points on the BSFC map. Based on this assumption, for a given $P_{eng}(t)$, the engine speed and torque are calculated according to the OOP. The optimization problem (3.2) is solved using MPCTools package [89], which exploits the IPOPT solver [90] and CasADi for numerical optimization. In our simulations, the optimization is warm-started and the solution achieved in the current time step is applied as the initial guess solution for the next iteration. The simulations are performed on a desktop computer with an Intel® E-2136@3.30 GHz processor.

In order to evaluate the performance of the MPC in (3.2), a driving cycle with the speed profile shown in Fig. 3.3-(a) is considered in this section. This driving cycle is based on the New European Driving Cycle (NEDC) and includes a combination of city (with multiple stop-and-go) and highway driving. Note that in this section, it is assumed that an accurate prediction of the vehicle speed is available over the prediction horizon, and thus, uncertainties associated with vehicle speed prediction are not taken into consideration. This assumption will be relaxed in the following sections and the sensitivity of the results to the speed preview uncertainty will be investigated.

As the performance of MPC can be affected by the length of the prediction horizon [91], the fuel consumption results for different prediction horizons are summarized in Fig 3.2-(a). As the benchmark, the optimal solution computed by using dynamic programming (DP) is also shown in Fig 3.2. DP solves the following discretized optimization problem:

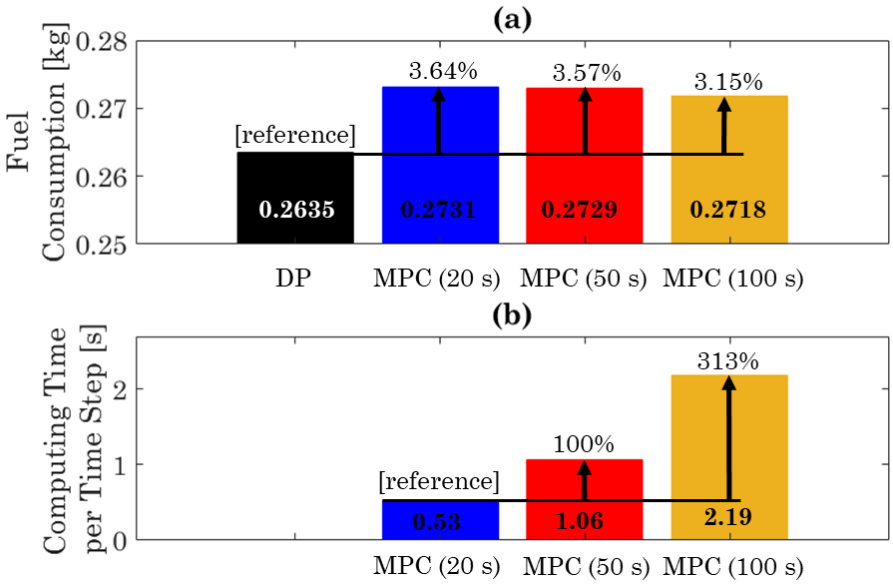

Figure 3.2: Simulation results of DP and conventional MPCs with different prediction horizons. (a) fuel consumption (b) average computational time per time step.

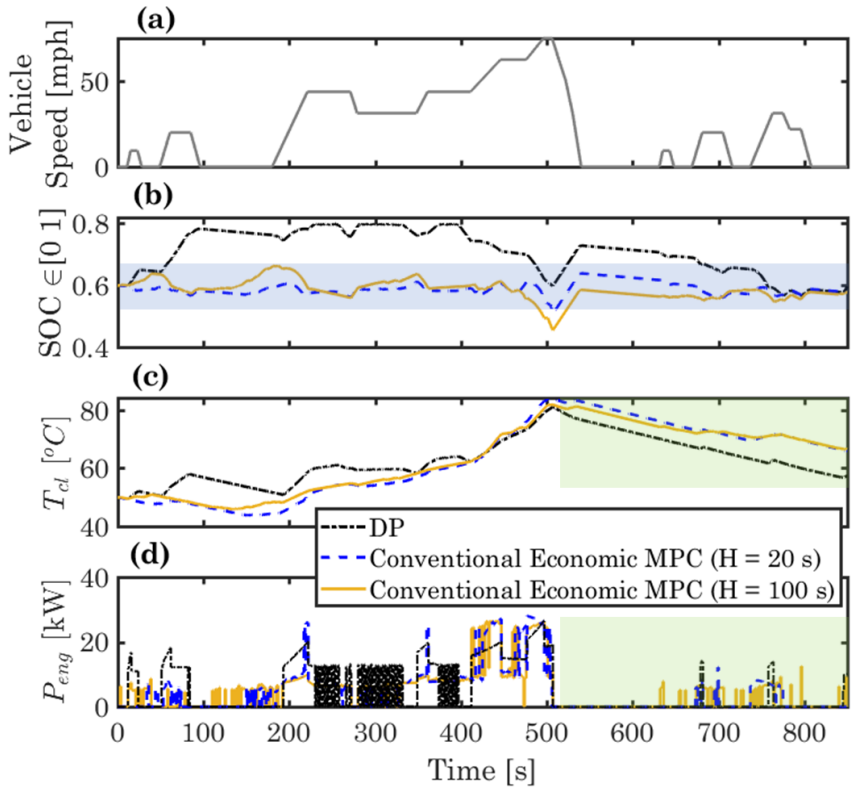

Figure 3.3: State trajectories of conventional MPC with different prediction horizons and DP: (b) SOC, (c) T_{cl}, and (d) engine power.

$$
\begin{aligned}
\underset{P_{bat}(i)}{\arg\min} \quad & \sum_{i=t}^{t+H_{tot}-1} \dot{m}_{fuel}(i)\delta t, \\
\text{s.t.} \quad & SOC(i+1) = SOC(i) + \delta t \cdot f_{SOC}(i), \\
& T_{cl}(i+1) = T_{cl}(i) + \delta t \cdot f_{T_{cl}}(i), \\
& SOC_{min} \leq SOC(i) \leq SOC_{max}, \\
& T_{cl,min} \leq T_{cl}(i) \leq T_{cl,max}, \\
& T_{cl}(0) = T_{cl,init}, \\
& SOC(0) = SOC(end) = SOC_{init},
\end{aligned}
\tag{3.2}
$$

where N_{tot} is length of the entire trip. The charging sustainability condition can be enforced as a terminal condition, and there is no artificial penalty term in the cost function. A detailed analysis of the results reveals the following insights:

First of all, while fuel consumption decreases as the prediction horizon is extended from 20 to 100 steps, the MPC still consumes 3.15% more fuel than DP. Note that as $\delta t = 1\ s$, the time period of one discrete step is 1 s. Figs. 3.3-(b,c) show the state trajectories of DP and conventional MPC. One can see that the SOC of MPC solution varies in a limited range of $\approx 10\%$. Increasing the prediction horizon has a marginal impact on this narrow variation range. This is because the conventional MPC only has the awareness of the future vehicle speed information over the receding horizon and the quadratic term in the cost function penalizes the SOC deviation from its terminal reference value. DP, on the other hand, has access to the entire driving cycle a priori, thus, the battery can be utilized more efficiently by expanding the operation range of SOC, as shown in Figs. 3.3-(b).

Secondly, the thermal responses are also quite different between MPC and DP solutions. Exploiting the information about the upcoming long stop (around t=100 to 180 s) before entering the highway, DP increases T_{cl} in advance, thereby avoiding having the coolant temperature drop below its lower limit threshold that can trigger

engine idling. The conventional MPC, on the other hand, is able to exploit preview information only over a short-horizon, leading the engine to operate within the inefficient coolant temperature range, i.e., $< 50^oC$. Towards the end of the trip, as highlighted in Fig. 3.3-(c), the vehicle exits the highway and starts a city driving phase with low traction power demand and multiple stop-and-go events. Since DP is able to exploit full trip information, it manages to store enough electrical energy in the battery (for traction) and thermal energy in the coolant (for cabin heating) before exiting the highway at around t=500 s, so that the vehicle can reach the end of the trip mainly in full electric mode. This can be seen from the engine power trajectory in Fig. 3.3-(d) showing the engine power is demanded only for few instances after $t = 500$ s. For the MPCs, on the other hand, limited electrical energy has been stored in the battery (Fig. 3.3-(b)), and so the engine is being used more often after t=500 s, resulting in unnecessarily high coolant temperatures by the end of the trip.

Thirdly, although the fuel consumption can be reduced with a longer prediction horizon, the MPC computational footprint grows with the length of the prediction horizon as shown in Fig. 3.2-(b). In particular, as the prediction horizon increases from 20 to 100 steps, the computational time increases by 313% on average per time step, making long horizon MPC prohibitive for real-time implementation.

Last, in this section, the vehicle speed (which informs traction power demand) over the prediction horizon is assumed to be known accurately . In the real-world traffic environment, long-term prediction of the vehicle speed is uncertain. This uncertainty can lead to further degradation of energy efficiency.

To address these challenges, a novel multi-horizon MPC is first-time proposed in the next subsection to address the trade-off between energy efficiency and computational footprint, in the presence of vehicle speed prediction uncertainty.

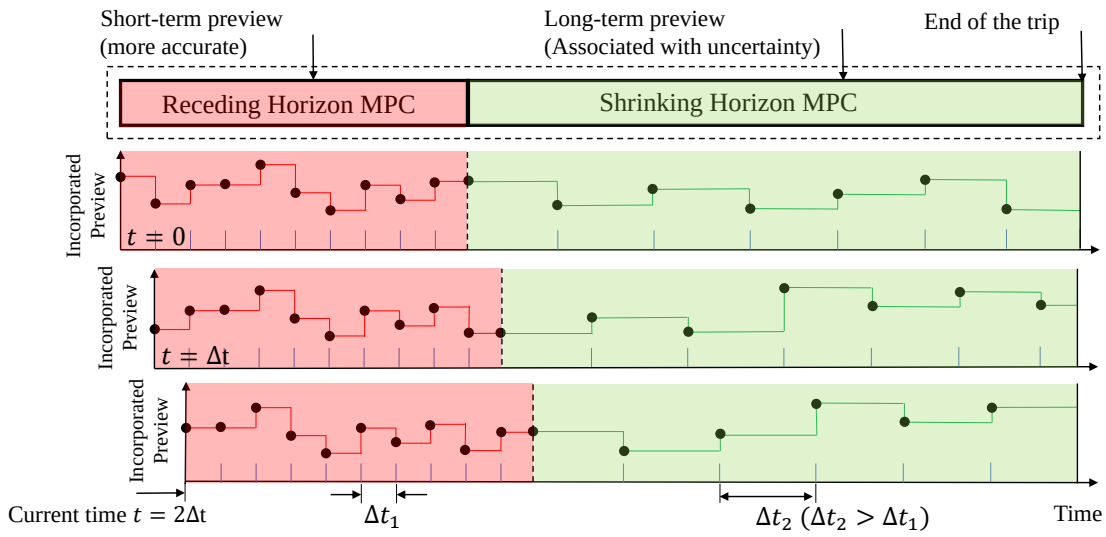

Figure 3.4: The concept of Multi-horizon MPC with short receding horizon and long shrinking horizon.

3.3 Multi-horizon MPC (MH-MPC)

The concept of the proposed MH-MPC is illustrated in Fig. 3.4. The prediction horizon spans the entire trip and is divided into two segments, (i) a short receding horizon (red window), and (ii) a long shrinking horizon (green window). Over the short receding horizon, the vehicle speed preview is assumed to be accurate. Note that for connected vehicles, a high accuracy short-term prediction of the vehicle speed may be obtained using the vehicle-to-vehicle (V2V) and vehicle-to-infrastructure (V2I) communications, see [92] for an example.

Over the long shrinking horizon, an "approximate" vehicle speed preview is assumed to be available. This approximate preview does not require a detailed second-by-second forecast of the vehicle speed. Instead, the time history of the vehicle speed consists of main traffic events, e.g., acceleration and deceleration at signalized intersections and the average cruise speed between the intersections. Note that for a specific road segment with multiple intersections, a long-term vehicle speed preview could be informed by machine learning from the historic traffic data collected from

connected vehicles driving through the same corridor, see [30] for an example.

Remark 3.1: Long-term speed prediction in mixed, uncertain, and dynamic traffic environments is challenging. Real-time route optimization and real-time traffic flow control can complicate the speed and trip time prediction even further. Consequently, it is important to understand the requirements on vehicle speed prediction accuracy, the impact of the associated uncertainties, and acceptable uncertainty bounds to make the iPTM and look-ahead information beneficial for fuel-saving. To that end, Section 3.4 provides statistical analysis to (i) identify key traffic events, and (ii) assess the impact of bounded uncertainties in speed prediction on the iPTM results.

The MH-MPC is based on the solution to the following discrete-time optimal control problem:

$$
\begin{aligned}
\underset{P_{bat}(i)}{\arg\min} \quad & \sum_{i=t}^{t+N-1} \dot{m}_{fuel}(i)\Delta t_1 + \sum_{i=t+N}^{t_{end}} \dot{m}_{fuel}(i)\Delta t_2, \\
\text{s.t.} \quad & SOC(i+1) = SOC(i) + \Delta t_j \cdot f_{SOC}(i), \quad j \in \{1,2\} \\
& T_{cl}(i+1) = T_{cl}(i) + \Delta t_j \cdot f_{T_{cl}}(i), \quad j \in \{1,2\} \\
& SOC_{min} \leq SOC(i) \leq SOC_{max}, \\
& T_{cl,min} \leq T_{cl}(i) \leq T_{cl,max}, \\
& (1-\delta) \times SOC(0) \leq SOC(t_{end}) \leq SOC(0) \times (1+\delta), \\
& T_{cl}(0) = T_{cl,init}, \quad SOC(0) = SOC_{init},
\end{aligned}
\tag{3.3}
$$

where N is the short receding horizon, δ reflects the charging sustaining requirement. In this study, $\delta = 0.01$. t_{end} is the end time of the trip, Δt_1 and Δt_2 are the update periods over the receding and shrinking horizons, respectively, and $j \in \{1,2\}$ is determined as follows

$$
j = \begin{cases} 1, & \textbf{if} \quad i \leq t+N-1, \\ 2, & \textbf{if} \quad i \geq t+N. \end{cases}
\tag{3.4}
$$

The MH-MPC cost function has two terms:

- the fuel consumption over the short receding horizon calculated based on accurate vehicle speed preview,
- an estimate of the fuel consumption over the long shrinking horizon representing the "cost-to-go" of the entire remaining trip beyond the receding horizon.

By adding these two terms, the cost function of MH-MPC reflects the actual fuel consumption over the entire trip. The conventional MPC (3.2), however, only minimizes the fuel consumption over the receding horizon. Moreover, it can be seen in (3.3) that a quadratic penalty term in the MH-MPC cost function is no longer needed. This is because the predicted cost-to-go over the shrinking horizon includes an approximation of the SOC evolution until the end of the trip, and the constraint on SOC_{end} is explicitly incorporated to satisfy the charging sustainability condition, removing the need for penalizing its deviation from a reference value as in (3.2). To improve the feasibility of the optimization problem, the final SOC (i.e., $SOC(t_{end})$) is allowed to deviate by $\pm\delta$ from SOC_{init}. Moreover, due to the inclusion of the cost-to-go term over the shrinking horizon, a pre-computed SOC_r trajectory is no longer needed.

To reduce the computational footprint of the MH-MPC over the long shrinking horizon, $\Delta t_2 > \Delta t_1$ is used. The MH-MPC problem is solved every Δt_1=1 s and the first element of the computed control input is applied to the plant. Then, the receding horizon is shifted by Δt_1 and the shrinking horizon is shortened by Δt_1. Note that when the remaining trip time is shorter than the receding horizon length, the multi-horizon is no longer needed and there is only one shrinking horizon remaining in the cost function with the sampling time of Δt_1.

Note that the models used in two horizons can be different. For example, the model used in the shrinking horizon phase can, in principle, be of lower fidelity than that in the receding horizon phase. Furthermore, as large sampling time is used in

the shrinking horizon, alternative integration procedures to Euler's discretization may need to be implemented in predicting trajectories to improve numerical stability.

To study the sensitivity of the MH-MPC to the receding horizon length (N), as well as to the resolution (i.e., sampling time) over the long shrinking horizon (Δt_2), the MH-MPC with different parameters are simulated over the same driving cycle shown in Fig. 3.3-(a). The fuel consumption and the average computational time per time step are summarized in Fig. 3.5. It can be seen from Fig. 3.5-(a) that decreasing Δt_2 from 20 s to 10 s slightly reduces the fuel consumption. Increasing N, however, has a marginal impact on fuel consumption. On the other hand, as shown in Fig. 3.5-(b), different horizon lengths and sampling times lead to different computational footprints. Considering a trade-off between fuel consumption and computing demands, $N = 5$ s and $\Delta t_2 = 10$ s are selected and used in the remainder of this chapter. Moreover, the selection of $N = 5$ s makes the availability of accurate speed preview over the receding horizon more reasonable [93, 94]. Note that, for the results presented in this section, it is still assumed that a perfect long-term preview is available. However, its accuracy is degraded due to the integration of the continuous-time model with a longer time step.

Fig. 3.6 compares the results of MH-MPC with DP and conventional MPC. Compared to the conventional MPC, MH-MPC reduces the fuel consumption by more than 3% (Fig. 3.6-(a)). It leads to similar results achieved by DP. By comparing the computational time of MH-MPC and conventional MPC in Fig. 3.6-(b), one can observe that MH-MPC is far less computationally intensive than longer horizon conventional MPC while achieving better fuel efficiency performance.

The powertrain trajectories with MH-MPC are shown in Fig. 3.7 and compared with those of DP and the conventional MPC (with $H = 20$ s). Unlike the conventional MPC, the SOC trajectory of MH-MPC varies over a wider range ($> 20\%$) and shows a similar trend with DP. This is because MH-MPC has the awareness of the entire

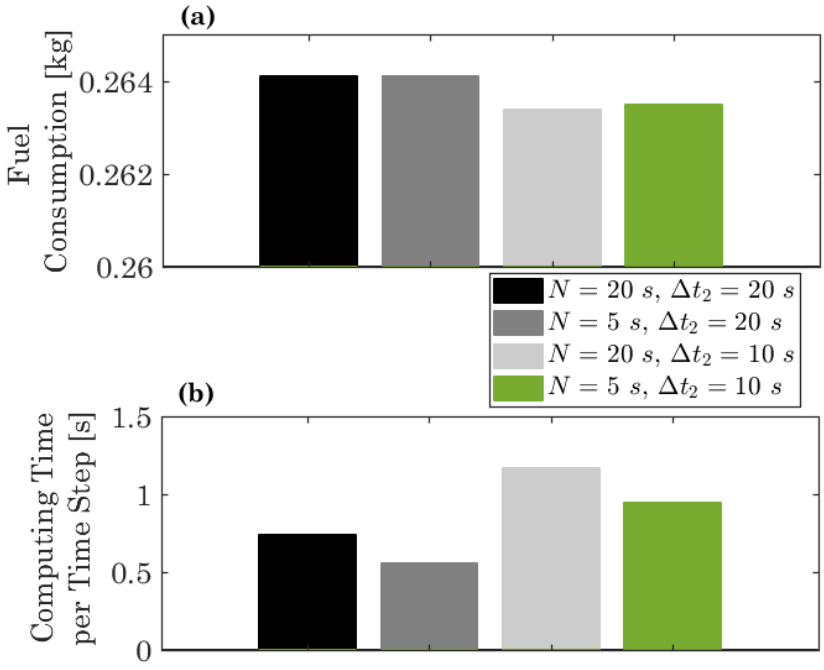

Figure 3.5: Fuel consumption and average computational time for different short receding horizons and for different sampling times over the long shrinking horizon.

driving cycle and accounts for the cost-to-go beyond the receding horizon. During the first part of the trip, as the initial engine coolant temperature is relatively low, in order to improve the engine efficiency via engine warm-up, MH-MPC decides to use the engine more frequently and at higher power (Fig. 3.7-(c)) to provide traction power while increasing the coolant temperature. Consequently, the battery is also being charged during this period using the extra engine power. Then, when the vehicle exits the highway (around t=540 s), similar to DP, the vehicle operates mainly in electric mode until the end of the trip (t=540 to 850 s), see Fig. 3.7-(c). This is possible since the MH-MPC has stored enough thermal energy in the coolant to satisfy the cabin heating towards the end of the trip. Thus MH-MPC is able to utilize the engine coolant as thermal energy storage, providing an additional degree of flexibility (in addition to the battery as electrical energy storage) for HEV energy flow optimization.

Remark 3.2: In this chapter, the considered driving cycles are relatively short

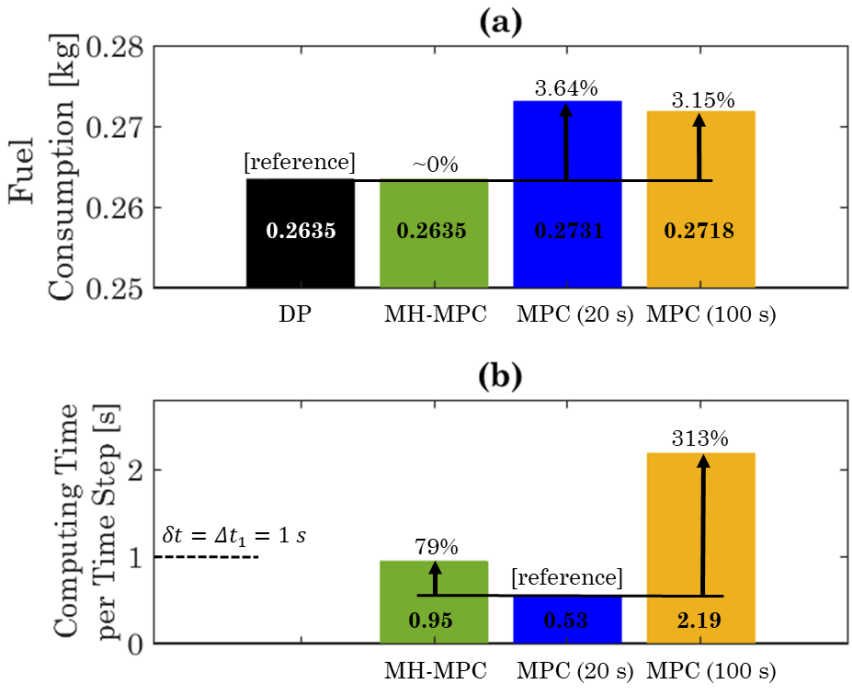

Figure 3.6: Simulation results of DP, MH-MPC, and conventional MPC with different prediction horizons. (a) fuel consumption, and (b) average computational time per time step.

($< 1000\ s$); thus, the end of the optimization horizon is set to be the end of the trip. For longer trips, such a strategy may result in increased computation load for MH-MPC. This issue can be mitigated by (i) setting the end of the optimization horizon to be the end of a long receding horizon along the trip, and later switching to the shrinking horizon as the vehicle approaches the destination to enforce the terminal constraints, or (ii) applying a more intelligent/adaptive sampling procedure over the shrinking horizon to keep the MH-MPC computational footprint at the acceptable level while ensuring that the essential look-ahead information over the long-horizon is captured and not missed due to coarse sampling.

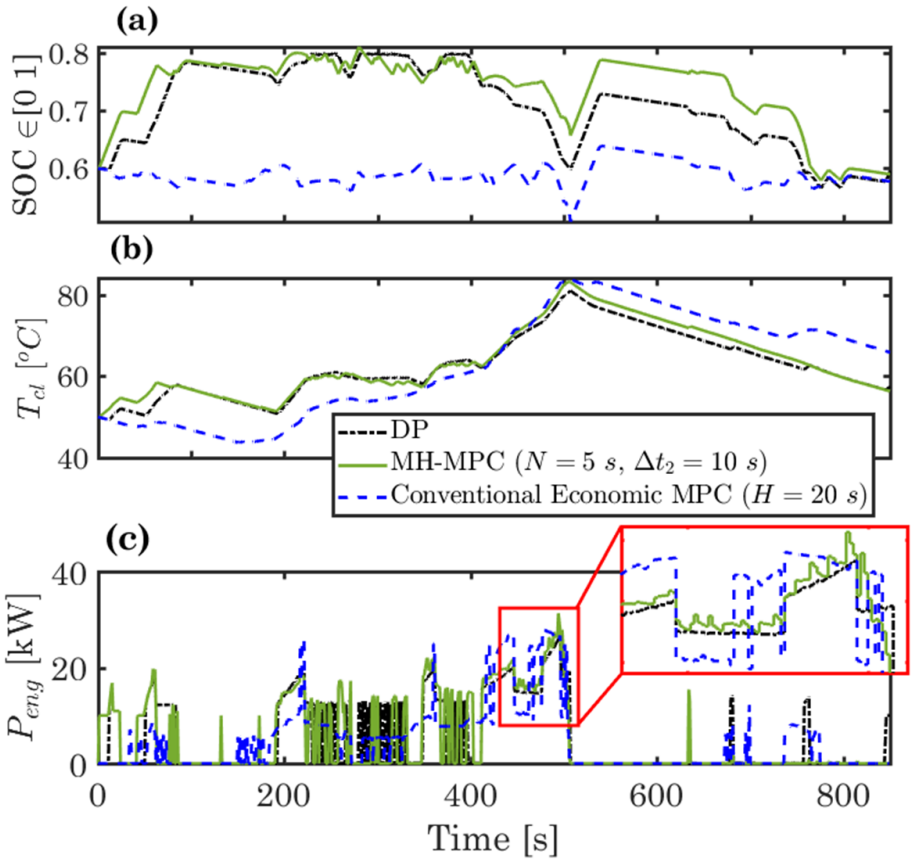

Figure 3.7: State trajectories of DP, MH-MPC, and conventional MPC: (a) SOC, (b) T_{cl}, and (c) engine power.

3.4 Robustness of MH-MPC against Uncertainties in Vehicle Speed Preview

The benefits of the proposed MH-MPC were studied in the previous section under the assumption that the speed preview is known a priori over both short- and long-range horizons. In this section, we relax this assumption to investigate the robustness of the MH-MPC to uncertainties associated with vehicle speed preview. As will be shown, this sensitivity analysis helps identify the major traffic events that significantly affect the energy efficiency improvement and hence need to be predicted.

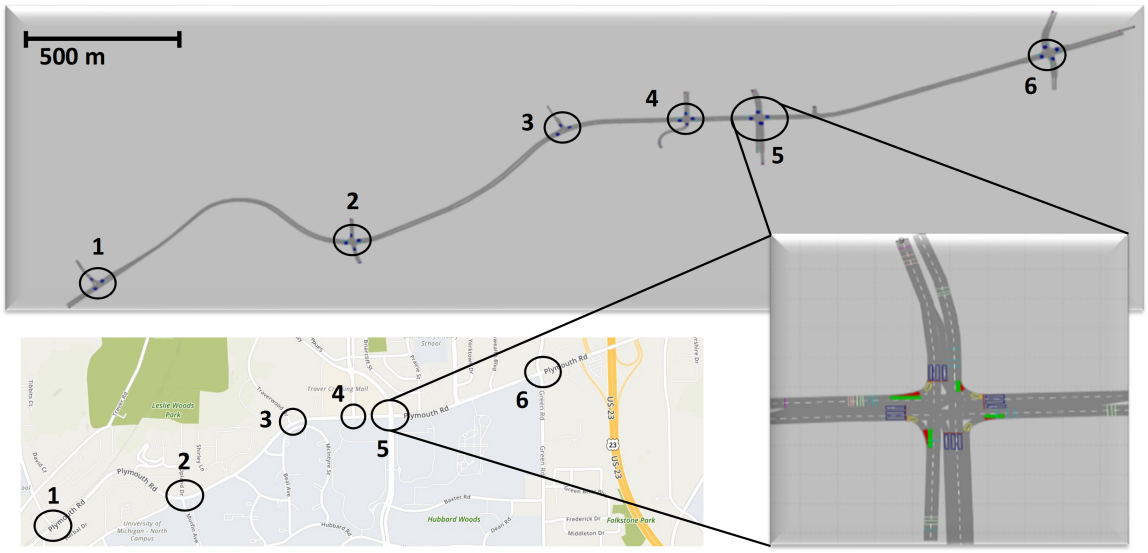

Figure 3.8: Plymouth corridor in Ann Arbor used for traffic modeling and simulation.

3.4.1 Real-world Traffic Simulation Data

To generate the real-world traffic data needed to evaluate the MH-MPC performance, a city corridor was modeled and simulated in the microscopic traffic simulation software VISSIM [95]. The simulated corridor is located on Plymouth Rd., in Ann Arbor, MI encompassing six intersections as shown in Fig. 3.8, where the location of each intersection is marked by a black circle. This corridor is about 2.2 miles long with two lanes in each direction, connecting the downtown of Ann Arbor to the US-23 highway. Real-world traffic data, including traffic flow volume and signal timing at each intersection, was collected during the rush hour (4:00 - 5:00 PM) and used to calibrate and validate the VISSIM model as described in [84, 96]. A coordinated fixed-time signal timing policy with a cycle length of 100 s has been used in all intersections. This model was run for two and a half hours while the parameters of the traffic model were kept fixed and the traffic congestion-level did not change during the simulation. The speed profiles of 1478 vehicles driving through the entire corridor in the same direction (i.e., entering from the west) were recorded. Note that the total number of vehicles in the traffic traveling through this corridor was larger than 1478

as some vehicles may have entered or exited the corridor at one of the intersections.

3.4.2 Sensitivity Analysis of MH-MPC

First, ten vehicles were randomly selected from the pool of 1478 vehicles. For these vehicles the results of applying MH-MPC are compared with the results of applying DP in Fig. 3.9. When there is no uncertainty in the speed preview, Fig. 3.9 shows that for all ten selected vehicles, the MH-MPC achieves a comparable fuel consumption to DP with the difference within 0.9%.

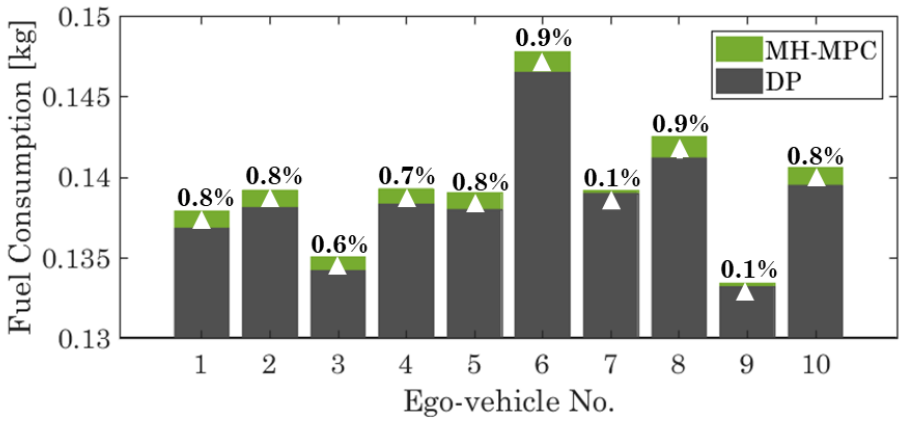

Figure 3.9: Fuel consumption results of MH-MPC and offline DP based on ten vehicle speed profiles randomly selected from the Plymouth Rd. driving cycles.

As discussed earlier, uncertainties in the vehicle speed prediction can potentially degrade the fuel consumption. To investigate the impact of speed preview uncertainties on the energy-efficiency of MH-MPC, three cases are considered over the long shrinking horizon as follows:

- **Case I**: exact vehicle speed is known a priori,
- **Case II**: the only available information is the cruise speed, i.e., the speed at which the vehicle is cruising after acceleration from stop and before deceleration to another stop,

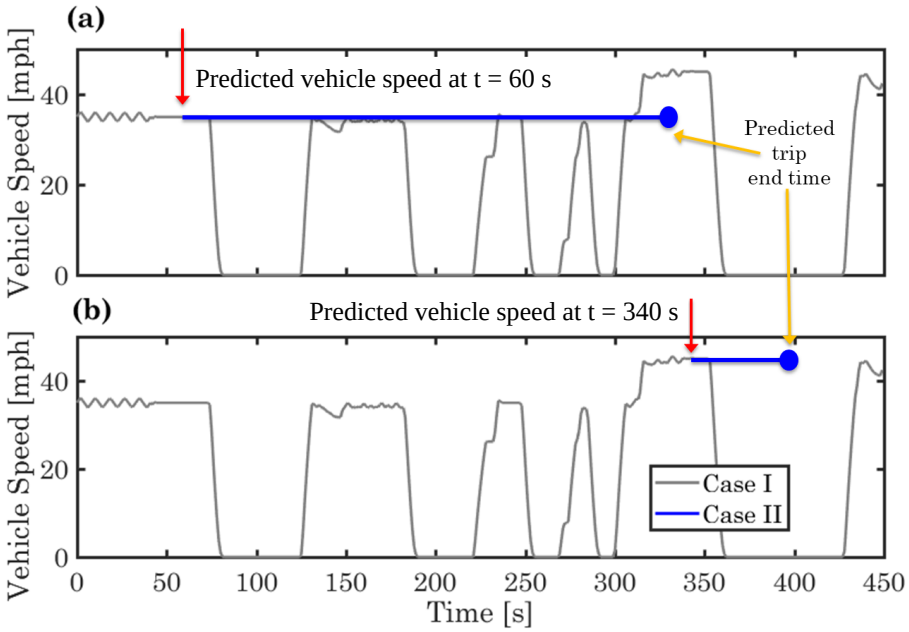

Figure 3.10: Case II as compared to Case I and the difference in the incorporated information over the long shrinking horizon of MH-MPC: (a) at around $t = 60$ s, the end time of the trip is estimated based on the known end location and the current cruise speed of 35 mph, and (b) towards the end of the trip at $t = 340$ s, the predicted trip end time is updated based on the remaining distance until the end location and the current cruise speed of 45 mph.

- **Case III**: in addition to the cruise speed (Case II), the spatio-temporal distribution of the vehicle stops at the signalized intersections is known.

Fig. 3.10 illustrates Cases I and II. It is assumed that the exact ending location of the trip is known a priori. In Case II, the vehicle speed over the long shrinking horizon is forecasted as constant equal to the last recorded cruise speed. The trip end time is calculated by dividing the remaining distance by the last recorded current cruise speed. When the vehicle comes to stop, the prediction of the trip end time is based on the last recorded cruise speed. Note that, as shown in Fig. 3.10, the cruise speed varies in different segments of the corridor, based on which the estimated trip end time is also re-calculated.

Fig. 3.11 illustrates the vehicle speed forecast in Case III and compares it with Case I, for which the entire driving cycle is known a priori over both receding and

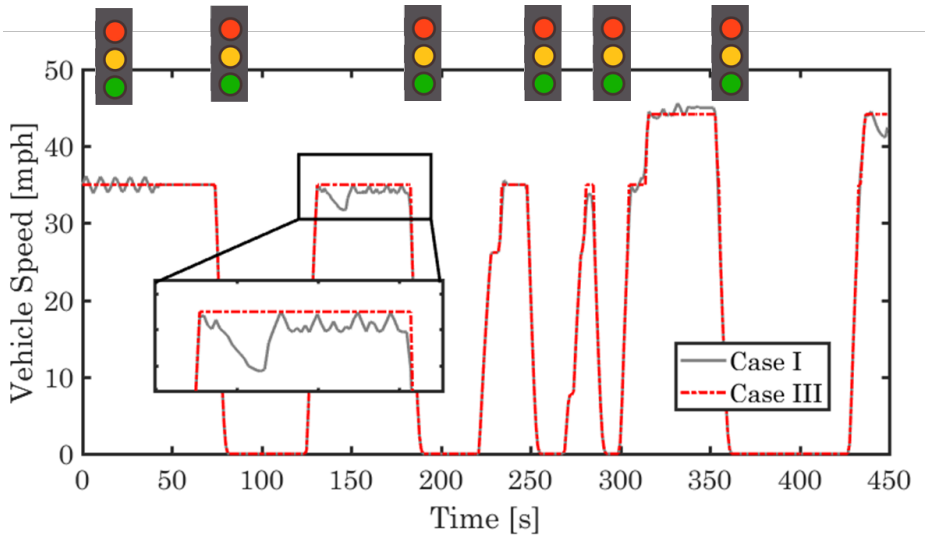

Figure 3.11: Case III as compared to Case I and the difference in the incorporated information over the long shrinking horizon of MH-MPC.

shrinking horizons. Case III assumes that the stop and departure times at each signalized intersection are known and forecasts the speed between intersections as equal to constant cruise speed in that segment. Note that the predictions of the stop events in Case III can be obtained by analyzing the historical traffic data, as we showed in our previous work [30]. In all of these three cases, the prediction of the vehicle speed over the short receding horizon is assumed to be perfect and the trip distance is also known a priori.

Among all vehicles traveling through the corridor, 140 vehicles are randomly selected to analyze the performance of the MH-MPC for three cases defined above. While these vehicles have different speed profiles, the initial conditions for T_{cl} and SOC, ambient temperature, and cabin heating demand are the same. Fig. 3.12 shows the probability density function for the fuel consumption percentage "increase" from Case II and Case III as compared to Case I. Additionally, the conventional MPC with $H = 20\ s$ is also presented as the benchmark. The average fuel consumption increase of Case II compared to Case I is 1.43%, which is 0.59% better than the conventional MPC on average. It shows that by incorporating the long-term preview

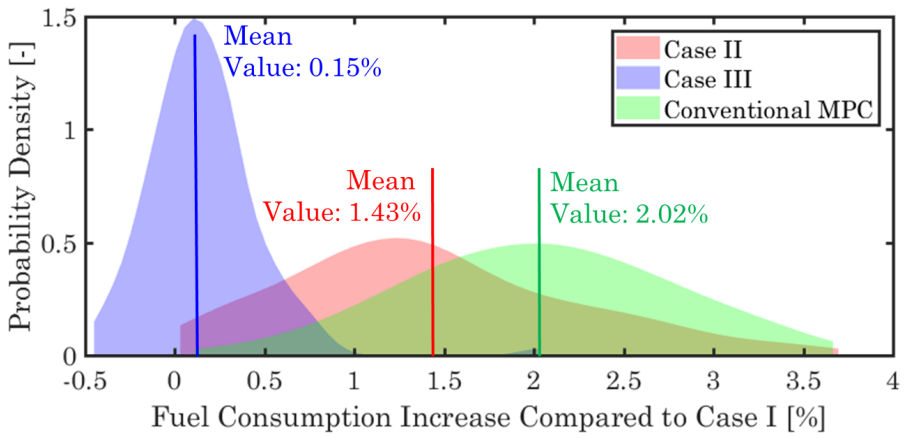

Figure 3.12: The probability density function of the fuel consumption increase with uncertain vehicle cruise speed preview.

via MH-MPC, even with a constant vehicle speed prediction over the long shrinking horizon, the MH-MPC can improve the fuel economy as compared to conventional MPC.

Comparing Case II and Case III, the fuel consumption is reduced by 1.28% on average and is only 0.15% more on average than in Case I. This suggests that spatio-temporal information about stop events and about cruise speed in intervals between stops can significantly improve fuel economy. The standard deviation of fuel consumption in Case III is 0.30%, which is also lower than in Case II (0.80%).

The state trajectories in three cases for one sample ego-vehicle are shown in Fig. 3.13. It can be seen that in all three cases, SOC is first pushed towards its upper limit (i.e., 0.8) while the engine coolant temperature is not warm enough at the beginning of the trip. Note that the SOC constraints are imposed as hard constraints in this study. To avoid the violation of SOC constraints, once the battery is fully charged (i.e., $SOC = SOC_{max}$), it is assumed that the friction brake is used instead of the regenerative braking to prevent battery overcharge, meaning the kinetic energy in the braking phase may not be recuperated fully. To fully recuperate the kinetic energy in the braking phase, knowing the upcoming stop event in advance, an

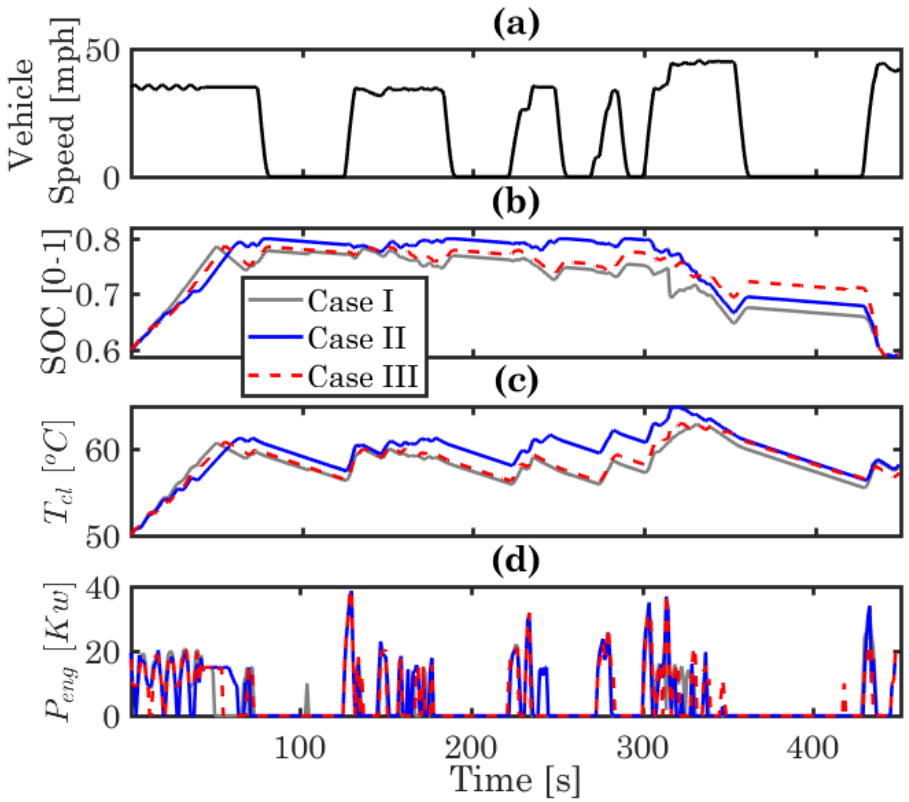

Figure 3.13: The state trajectories of the three cases evaluated for MH-MPC for one sample ego-vehicle: (a) vehicle speed, (b) SOC, (c) T_{cl}, and (d) engine power (P_{eng}).

optimal controller can command the SOC to decrease by using the battery for traction before the brake occurs. This creates spare charge capacity prior to the stop events. Such a desired response is observed for both Cases I and III in Fig. 3.13-(b). For Case II, however, the stop events are not known a priori over the long shrinking horizon. As a result, the MH-MPC cannot detect the stop events until the vehicle enters close proximity of the intersection and the stop event becomes visible to the controller within the short receding horizon. Only knowing the upcoming stop event within the short horizon does not provide the controller with enough lead time to discharge the battery proactively, thus it fails to recuperate the kinetic energy in the braking phase.

As the vehicle approaches the end of the trip, it is also desirable that the controller starts to release the stored electric energy in the battery and the thermal energy in the engine coolant, enabling the vehicle to operate in a more electric mode. Such

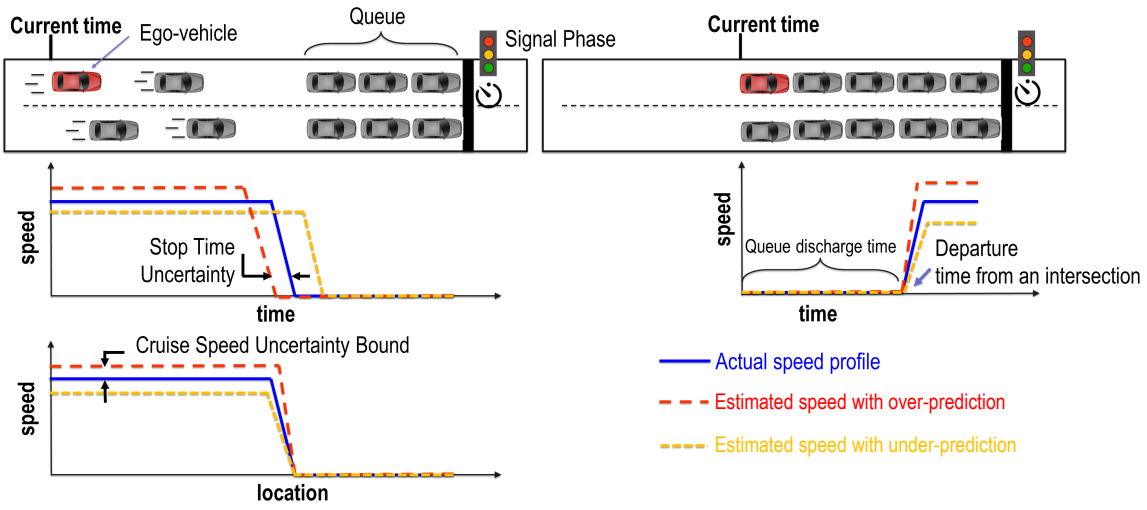

Figure 3.14: Different scenarios with uncertainties on the predicted cruise speed and the stop time. Over-prediction reflects the scenario that the predicted cruise speed is higher than the actual vehicle speed, and the stop time is predicted earlier. Under-prediction reflects the scenario that the predicted cruise speed is lower than the actual vehicle speed, and the stop time is predicted later.

a favorable response is observed in all cases, even for Case II. Note that for Case II, while the long-term speed prediction has large uncertainty from the beginning, as the vehicles approach the destination, the uncertainty in estimating the trip end time decreases. This allows the MH-MPC for Case II to adjust its actions and release the energy from the battery and the coolant as its awareness of the end of the trip increases.

3.4.3 Robustness of MH-MPC

The sensitivity analysis of the MH-MPC in the previous section suggested that the preview of stop events and cruise speed can significantly improve the performance of the proposed iPTM strategy based on MH-MPC. To further evaluate the robustness of the MH-MPC to errors in forecasting these, different levels (i.e., from -10% to +40%) of uncertainties are imposed on the "predicted" cruise speed and stop events over the long shrinking horizon as shown in Fig. 3.14. For instance, assuming the

exact location of an intersection is known a priori, if the predicted cruise speed is, e.g., 10% higher than the actual cruise speed, the predicted stop time is also shifted earlier by 10% as compared to the actual one. Thus the uncertainty imposed on the cruise speed will affect the predicted stop time at the intersections. In order to de-couple the cruise speed and vehicle stop time prediction uncertainty from other traffic parameters, here we make several assumptions:

- the queue length and the number of vehicles between the ego-vehicle and the intersection remain the same while the predicted vehicle cruise speed varies,
- while the ego-vehicle predicted cruise speed could be higher or lower than the actual one, it is assumed that the ego-vehicle does not change lane,
- the departure time from the intersections is determined by the traffic signal timing and the queue conditions at the intersection. Since these two are assumed to remain the same, as shown in the right-hand side of Fig. 3.14, the predicted departure time from the intersection will not be affected,
- while the predicted cruise speed varies, the prediction of passing or stopping at the upcoming intersection does not change.

Table 3.1 summarizes the statistical results (mean and standard deviation) of the fuel consumption increase compared to the ideal case (Case I), and Fig. 4.13 shows the probability density functions for different levels of uncertainties. The statistical results are based on the same 140 vehicles considered in the previous subsection. Note that only -10% case is presented for speed under prediction, because more under-prediction in the cruise speed will make the predicted stop time larger than the departure time, leading to a contradiction. Therefore, the scenarios of speed under-prediction of more than 10% are omitted from this study.

It can be seen that the average fuel consumption increase percentage, compared to Case I, is negligible when the uncertainties are $\pm 10\%$, and it increases from 0.39%

Table 3.1: The mean value and standard deviation of the fuel consumption increase results shown in Figure 4.13.

Uncertainty Bound [%]	**0%**	**-10%**	**+10%**	**+20%**	**+30%**	**+40%**
Mean Value [%]	0.15	0.06	0.39	0.87	1.01	1.34
Standard Deviation [%]	0.30	0.32	0.40	0.63	0.68	0.79

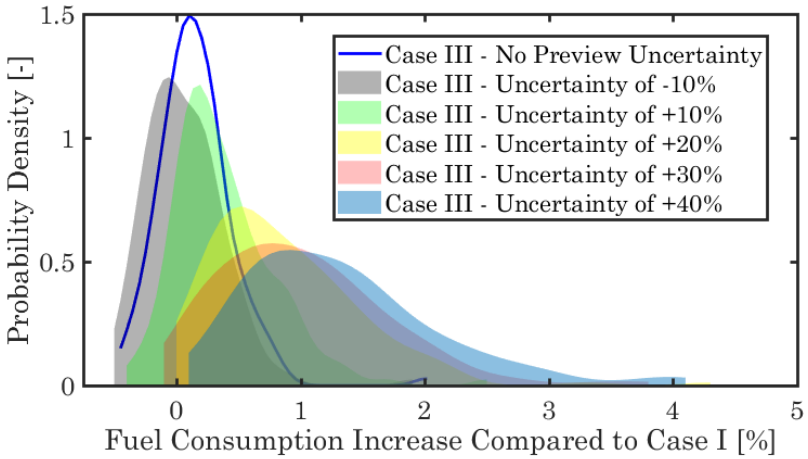

Figure 3.15: The probability density function of the fuel consumption increase with different percentages of uncertainties.

to 1.34%, as the uncertainties increase from +10% to +40%. As expected, the uncertainty in predicting the actual cruise speed and vehicle stop time degrade the MH-MPC performance. In particular, when the uncertainties are at +40%, the average fuel consumption increases by 1.34%. This observation indicates that, when the uncertainties are too large, the benefits of incorporating the stop event predictions could be diminished. Additionally, larger uncertainties lead to a larger standard deviation of fuel consumption increase, indicating higher variability in the fuel consumption results. Fig. 4.13 shows that the maximum fuel consumption increase is 4.12% when the imposed uncertainties are at +40%.

While the robustness analysis performed in this section focused on one particular type of uncertainty under an assumption that none of the other traffic parameters

have changed because of the imposed uncertainty, the results in Fig. 4.13 are encouraging suggesting the improvements in fuel consumption are possible despite levels of uncertainties of $\pm 10\%$. As we showed in our previous work [30], advanced data-analytic techniques can be applied to improve the accuracy of long-term vehicle speed forecasts, and thus, reduce the impact of the associated uncertainties on MPC-based energy management of connected vehicles.

3.5 Summary

In this chapter, a novel multi-horizon MPC (MH-MPC) strategy was proposed for integrated systems with dynamics responding over different timescales. The MH-MPC exploits multi-range prediction and optimization over a short receding horizon and a long shrinking horizon with different accuracies and resolutions. The MH-MPC estimates the "cost-to-go" over the long shrinking horizon, beyond the conventional receding horizon. This approach makes it appealing for use in mission-based problems where the objective is accomplishing a mission with a limited onboard energy resource. For such systems, the MH-MPC eliminates the artificial terminal penalty term in the receding horizon optimization cost function, allowing to incorporate an economic cost function over the entire prediction horizon. The economic cost function of MH-MPC and long shrinking horizon until the end of the mission enable the energy states to operate on or close to their admissible boundary to improve performance.

This proposed MH-MPC was demonstrated for integrated power and thermal management (iPTM) of HEVs operating in a connected traffic environment. In such an environment, short- and long-term predictions of the vehicle speed may be obtained using advanced V2V and V2I telematics, and incorporated over the receding and shrinking horizons of the MH-MPC. Simulation results of applying MH-MPC to a power-split HEV demonstrated improved performance of the MH-MPC as compared to conventional MPC with a battery charge sustaining terminal penalty. Furthermore,

in the absence of uncertainties in the vehicle speed forecast, MH-MPC performance was close to that of Dynamic Programming with a deviation of 1%. The MH-MPC performance also surpassed the long-horizon conventional MPC approach, while requiring less computational resources. The sensitivity and robustness of the iPTM strategy to uncertainties in long-term vehicle speed forecasts were also studied. The results suggested that, for city driving scenarios, the prediction of the vehicle stop events at signalized intersections and the average cruise speed between intersections are key information that can be leveraged for fuel-saving, even if the prediction is subject to moderate uncertainties.

CHAPTER IV

Multi-Range Vehicle Speed Prediction with Application to MPC-based Integrated Power and Thermal Management of Connected Hybrid Electric Vehicles

In Chapter III, a novel multi-horizon MPC (MH-MPC) strategy was proposed for integrated systems with dynamics responding over different timescales. The MH-MPC exploits multi-range prediction and optimization over a short receding horizon and a long shrinking horizon with different accuracies and resolutions. In the absence of uncertainties in the vehicle speed forecast, MH-MPC performance was close to that of Dynamic Programming. Furthermore, the sensitivity and robustness of the iPTM strategy to uncertainties in long-term vehicle speed forecasts were also studied. The results suggested that, for city driving scenarios, the prediction of the vehicle stop events at signalized intersections and the average cruise speed between intersections are key information that can be leveraged for fuel-saving, even if the prediction is subject to moderate uncertainties.

In this chapter, we develop a multi-range vehicle speed prediction framework for urban driving and incorporate it into MH-MPC for iPTM of power-split HEVs to demonstrate the associated fuel savings based on real-world driving scenarios.

4.1 Multi-range Vehicle Speed Prediction

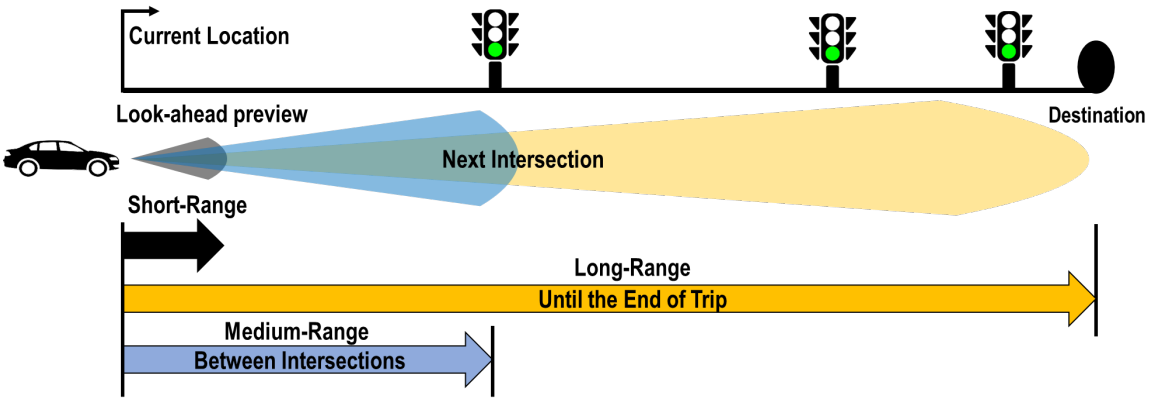

Figure 4.1: The concept of multi-range vehicle speed previews.

In this section, a multi-range vehicle speed prediction framework is introduced for urban driving cycle which enables efficient iPTM of CAVs. We assume that all the intersections in the driving route are signalized and that the destination is known from the beginning of the trip. As shown in Fig. 4.1, the vehicle speed preview is divided into three ranges as follows:

- **Short-range preview**: For the short range, e.g. $5-10$ *sec* ahead, the vehicle speed prediction could be obtained exploiting V-2V/I communications available to connected HEVs and queuing dynamic models at the intersections.

- **Long-range preview**: The long range preview covers the entire trip, for which the most probable driving scenario is predicted. Additionally, the passing/stopping at all remaining intersections, the cruise speed between intersections, and the end time of the trip are predicted according to the predicted driving scenario.

- **Medium-range preview**: In order to mitigate the uncertainty of long-range speed prediction, this study also explores a medium-range preview. This medium-range preview addresses the portion of the trip from the current vehicle location to the next intersection and involves prediction for passing/stopping event,

arrival/stop time, and departure time at the next intersection.

Our approach to implement the proposed multi-range vehicle speed prediction is data-driven. Note that the same traffic data set introduced in section 3.4.1 is used in this study, and the the prediction algorithms are detailed in what follows.

4.1.1 Short-range Preview

In this study, an accurate vehicle speed prediction over a relatively short-range horizon, e.g., 5-10 *sec*, is assumed to be available and known. A sufficiently accurate short-range speed prediction can be informed by V2V/I communications through model-based [96], stochastic [16, 92], data-driven [97, 98], and learning-based [99] methods. Noted that, in actual traffic, short-range speed predictions are subject to uncertainties, e.g., unexpected events such as vehicle cut-in that could lead to speed prediction errors. This study, however, is focused on enhancing the speed prediction accuracy over long and medium horizons.

4.1.2 Long-range Preview

We first present the long-range speed prediction strategy and motivate the need for a medium-range speed prediction, which will be presented in section 4.1.3. The long range vehicle speed prediction becomes necessary given relatively slow thermal dynamics. As shown in Fig. 4.1, the long-range vehicle speed preview defined in this work covers the segment from the end of the short-range preview until the end of the trip. Accurately predicting vehicle speed over such a long range is fundamentally challenging. Fig. 4.2 shows the mean value and standard deviation of all 1478 vehicle speed trajectories collected over the Plymouth Rd as described in section 3.4.1. It can be seen that this aggregated average speed, with large standard deviation, does not provide insightful information about the traffic flow. For example, the stop-and-go behavior at the signalized intersections cannot be predicted, making the aggregated

average speed not meaningful for long-range vehicle speed prediction. The aforementioned observations of the aggregated vehicle speed suggest that additional data processing is needed to get a clearer patterns of the long-range preview and reduce the error of forecast.

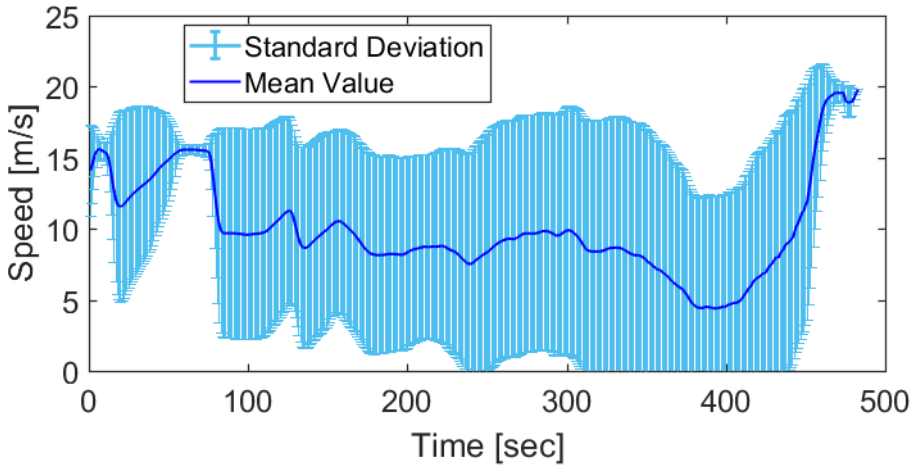

Figure 4.2: The mean value and standard deviation of all simulated vehicle speed data collected over the Plymouth Rd corridor.

To enable long-term vehicle speed prediction, a Bayesian Network (BN) is adopted to classify the traffic data and generate a long-term driving scenario tree. Specifically, we treat passing/stopping events at intersections as stochastic variables dependent on the observed events at upstream intersections. These events influence the probability distributions of the variables at downstream intersections. A BN can take into account the causal relationship between the variables of interest and represent conditional dependencies between a set of random variables [100]. The BN can be exploited to generate a dynamic scenario tree to obtain the joint probability distribution of passing/stopping events at different intersections, from which the "most probable" driving scenario is determined. The concept of this BN for urban driving is presented in Fig. 4.3, in which the most probable driving scenario is updated in real-time after the vehicle passes each intersection according to (i) observations obtained from the actual driving, and (ii) changes in the probability distribution of passing/stopping

events as the traffic evolves. As an example and according to Fig. 4.3, while from the beginning the vehicle is predicted to pass the first intersection (Fig. 4.3-(a)) as the computed probability of passing is larger than that of stopping, the actual observation indicates that the vehicle stops at the first intersection. Consequently, the most probable driving scenario is updated once the vehicle departs the first intersection (Fig. 4.3-(b)).

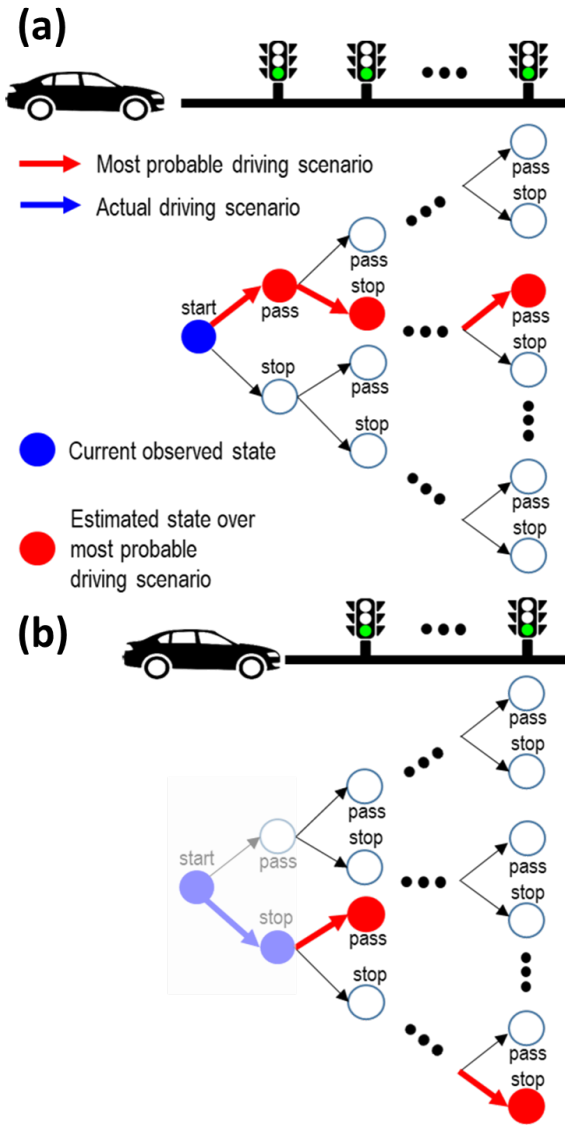

Figure 4.3: Driving scenario generation for estimation of most probable driving scenario over an arterial corridor using BN: (a) before the vehicle approaches the first intersection, (b) when the vehicle is between the first and second intersections.

For the BN that is developed for an arterial corridor, we interpret an arc from intersection k to $k+1$ as stop/pass at intersection k followed by stop/pass at intersection $k+1$. For a corridor with H intersections, each intersection is considered as a node represented by x_k ($k = 1, \cdots, p, \cdots, H$), where x_k takes the values of "true" for passing and "false" for stopping. At intersection p, the joint probability distribution for the remaining trip is updated as

$$Pr(x_p, \cdots, x_H) = \prod_{k=p}^{H} Pr(x_k | x_{\mathbf{P}_k}). \tag{4.1}$$

Here $Pr(x_k|x_{\mathbf{P}_k})$ is the conditional probability distribution associated with intersection k and $\mathbf{P}_k$ is the set of indices labeling the upstream intersections of the k^{th} intersection [100, 101]. For instance, $Pr(x_4|x_1 = \text{True}, x_2 = \text{False}, x_3 = \text{False})$ indicates the probability of the ego-vehicle passing the fourth intersection after it has passed the first, but stopped at the second and at the third intersections. Note that the directed arc of the BN should flow forward both in the time direction and in the traffic flow direction [100].

The conditional probability distribution of the passing/stopping events at intersections is inferred from the traffic data according to (4.1). Note that, while in this study the data set is built based upon the Vissim traffic simulation model, in practice, the connected vehicles speed data can be collected, analyzed, and updated by a central/cloud server in real-time, constructing the historical traffic data set for a specific memory length. The speed of a vehicle traveling through the corridor is estimated using the branch with the highest product of probabilities, which represents the most probable driving scenario until the end of the trip. The branch selection is updated during the trip based on the observed states (i.e., observation of actual passing/stopping events at given intersections).

The vehicle data collected over the Plymouth Rd driving corridor are used to

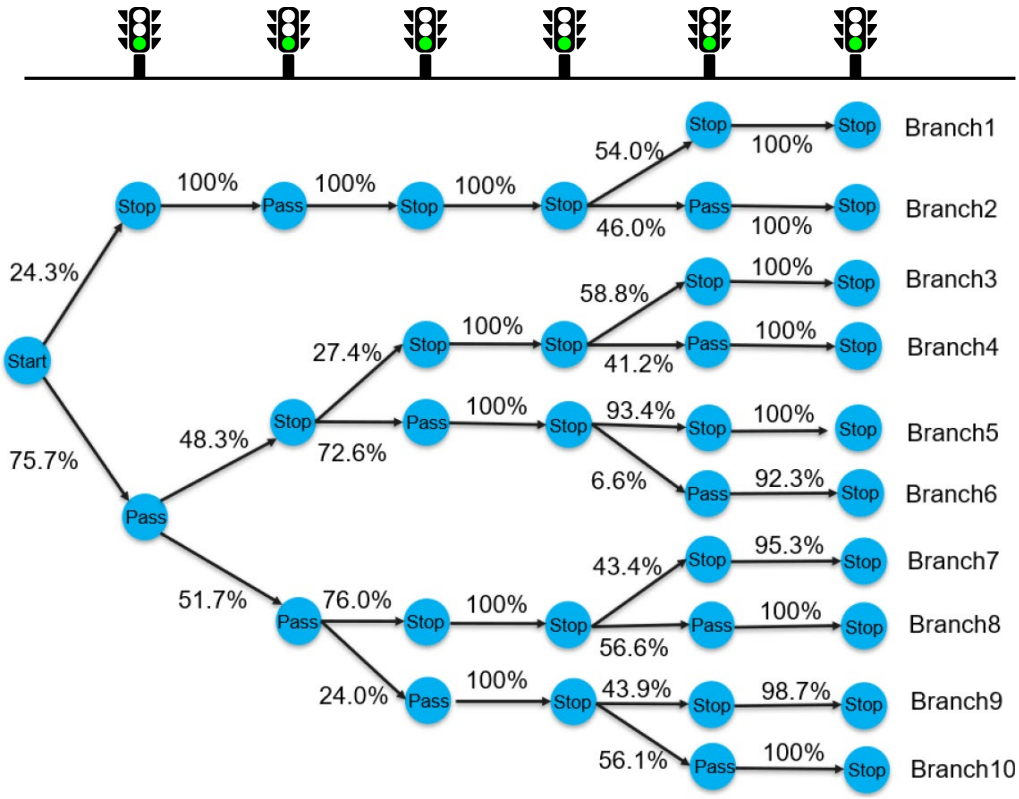

Figure 4.4: The BN developed based on the historical data over an arterial corridor. The numbers over the arrows indicate probability.

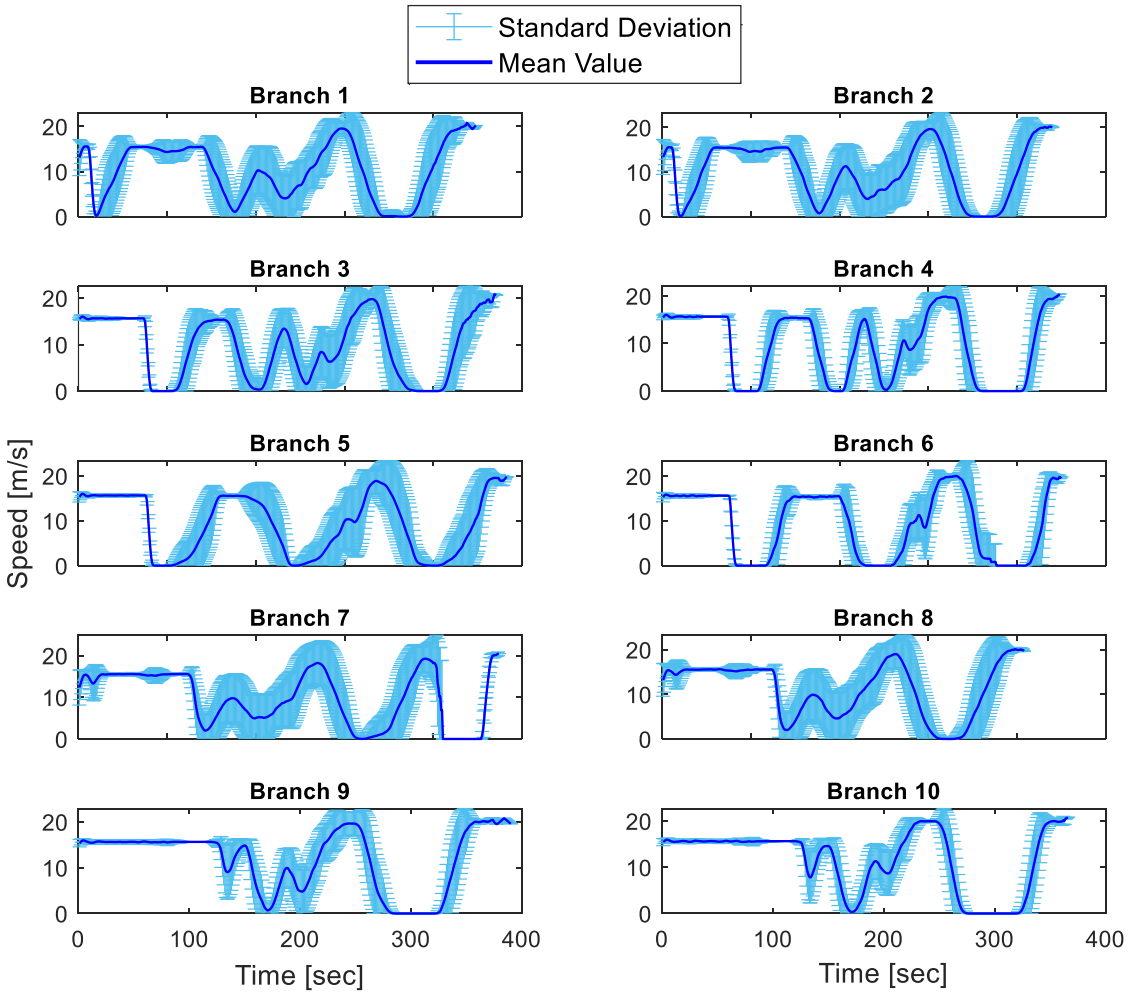

Figure 4.5: The mean value and standard deviation of vehicles in 10 branches classified by BN.

inform the proposed BN. The results are presented in Fig. 4.4. It can be seen that the BN for the section of Plymouth Rd consists of 10 main branches. Note that there are 3 minor branches with probability of less than 0.01 that are excluded from the BN. The time-varying mean and standard deviation of the vehicle speed for each of the 10 branches of the BN are reported in Fig. 4.5. It can be observed that the prediction of vehicle speed over a given branch provides a marked improvement over using the average speed of all trajectories. Therefore, this BN will be leveraged for long-range vehicle speed prediction. Additionally, the BN can be used to predict passing/stopping events at signalized intersections and the end time of the trip that

are useful in energy management optimization.

To summarize, a BN is developed to provide the conditional probabilities of passing/stopping events at signalized intersections. When used in real-time for vehicle speed prediction, the vehicle speed profile prediction corresponds to the branch with the highest probability. The probability for each branch is updated each time a stop/pass event is observed. The developed BN is designed to capture an "average" behaviour of drivers based on the data described in section 3.4.1. In actual traffic, drivers have different levels of aggressiveness, requiring the adaptation of the long-term speed prediction for each "ego" vehicle. For automated vehicles the sensitivity of the long-term speed predictions to these types of individual vehicles' behaviors is expected to be smaller. The developed BN treats vehicles with noticeably different behaviors, as compared to the average traffic, as outliers that have less impact on the average traffic flow dynamics.

Remark 4.1: Expanding the proposed BN-based approach to corridors with more intersections requires a more systematic way to generate a scalable driving scenario tree. To that end, insights from scenario tree generation in stochastic MPC [16, 102] may be considered.

4.1.3 Medium-range Preview

In the previous subsection, a BN is developed to provide long-range vehicle speed forecast by predicting the most probable driving scenario. However, sometimes, the prediction error of forecast passing/stopping events at intersections can be large. For example, as shown in Fig. 4.4, for the vehicles passing through the first intersection, the probability of passing and stopping at the second intersection are 51.7% and 48.3%, respectively. Thus almost half of the vehicles (passing the first intersection) are expected to be mis-predicted using the BN and this introduces substantial uncertainty into the long-range vehicle speed prediction due to significant differences

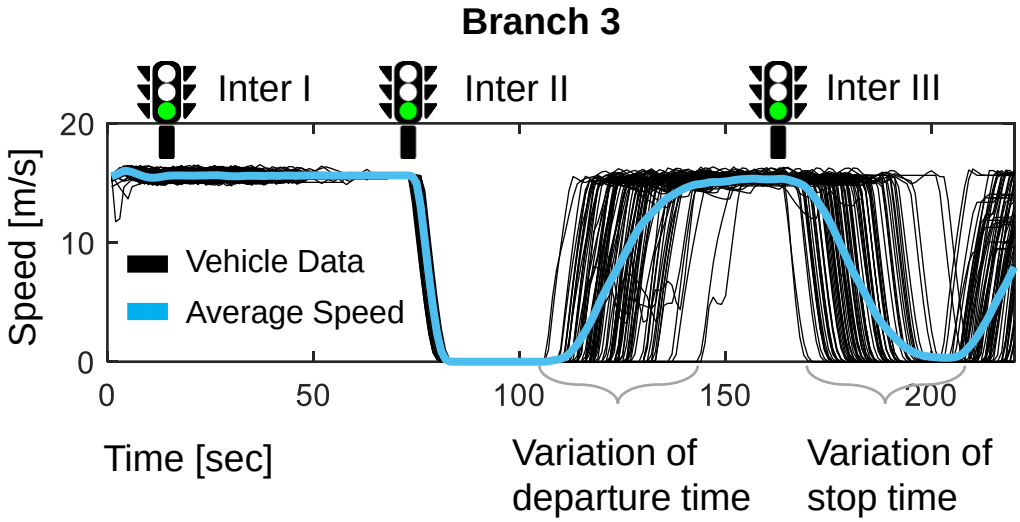

Figure 4.6: The variation of the stop time and departure time at intersections for the vehicle data in Branch 3.

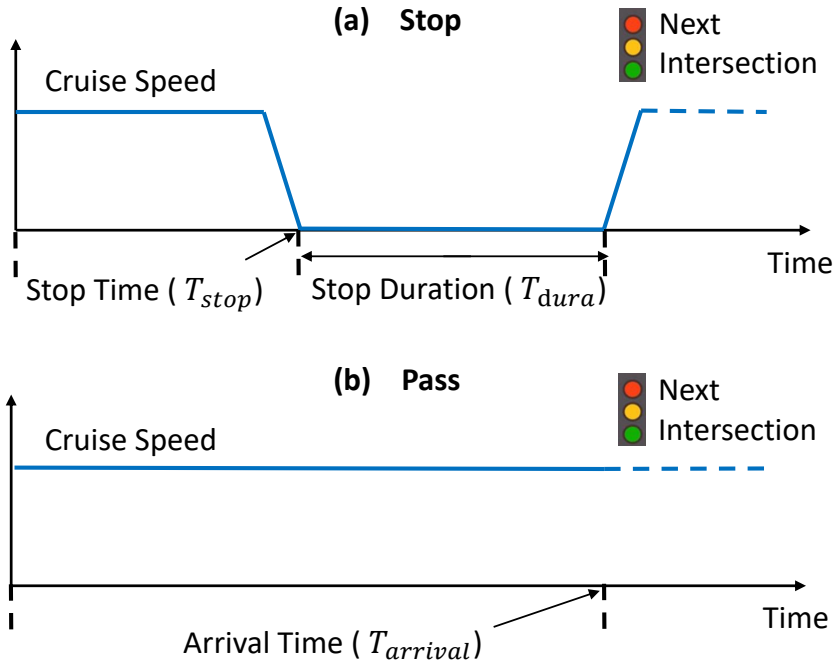

Figure 4.7: Predicted vehicle speed in the medium-range for ego-vehicles (a) stopped at next intersection and (b) passing through the next intersection.

between the average speed of the branches. Another limitation of this long-range vehicle speed prediction is the uncertainty around the stop time and departure time

Figure 4.8: The concept of vehicle speed in the medium-range preview.

at intersections. As shown in Fig. 4.6, Branch 3 displays large variations in the stop times and departure times at intersections. This variation may be attributed to the queuing dynamics and traffic signal phase switch. Additionally, most of the vehicles have similar acceleration/deceleration profiles but shifted in time which confounds the average speed. To address these issues, a medium-range preview is introduced.

Assuming an urban driving scenario with signalized intersections, the medium range preview involves the prediction of vehicle speed from the end of the short-range preview to the next intersection. Fig. 4.7 illustrates the models of vehicle speed trajectories assumed in the medium-range that are dependent on the forecasted passing/stopping events at the next intersection. The vehicle speed between intersections is assumed to be equal to the average cruise speed (V_{cruise}). Note that the cruising here means that the vehicles travel at the speed limit of the segments (in Vissim the cruising speed between intersections is set to the speed limit of the corresponding segment) and varies within a range of 2 m/s. For vehicles stopping at the next intersection, we define the stop time (T_{stop}) and stop duration (T_{dura}) as shown in Fig. 4.7. For vehicles passing through the next intersection, the arrival time ($T_{arrival}$) is defined as the time to reach the stop bar at the next intersection, see Fig. 4.7, and is estimated as

$$T_{arrival} = \frac{s_{bar}}{V_{cruise}}, \tag{4.2}$$

where s_{bar} is the distance between the vehicle and the stop bar at the next intersection. Note that it is assumed that the location of vehicle and the stop bar of intersections are available during the trip, and thus s_{bar} can be calculated in real-time. As shown in Fig. 4.8, for vehicles stopping at the next intersection, both T_{stop} and T_{dura} are

significantly influenced by the queue length (s_{queue}), and thus are predicted as follows:

$$T_{stop} = \frac{s_{bar} - s_{queue}}{V_{cruise}}, \tag{4.3}$$

$$T_{dura} = T_{signal} + T_{queue}, \tag{4.4}$$

where T_{signal} and T_{queue} are the time duration that an ego-vehicle needs to wait for (i) the traffic signal phase switch, and (ii) the discharge of the queue, respectively. It can been seen that, in order to predict the vehicle speed using aforementioned models, pass/stop and queue length information for the next intersection are needed .

To this end, a real-time vehicle speed prediction is proposed, based on V2V/I communication and passing/stopping prediction over the medium-range. Fig. 4.9 presents flow chart of the proposed strategy. Once an ego-vehicle enters a segment between two intersections, the model of the vehicle speed trajectory in Fig. 4.7 is selected based on the predicted passing/stopping event at the next intersection. If this vehicle is predicted to pass through the intersection, the arrival time is calculated by equation (4.2) and the vehicle speed trajectory in the medium-range is predicted using the model in Fig.4.7-(b). If this vehicle is predicted to stop, T_{stop}, T_{dura} as well as s_{queue} need to be predicted. To accomplish this, first, we assume the number of vehicles (N) ahead of this ego-vehicle in the respective road segment is known. Note that, in a road segment between two intersections, if coordinates of the vehicles in front are known either through the vehicle to vehicle communications [103], through the individual vehicle to infrastructure (cloud) communications, or through infrastructure-based sensing, the number of vehicles in front of an ego-vehicle (N) can be inferred. Approaches that are based on vision-based systems onboard of the ego-vehicle can also be used.

In the next step, the passing/stopping events for all these N vehicles are predicted

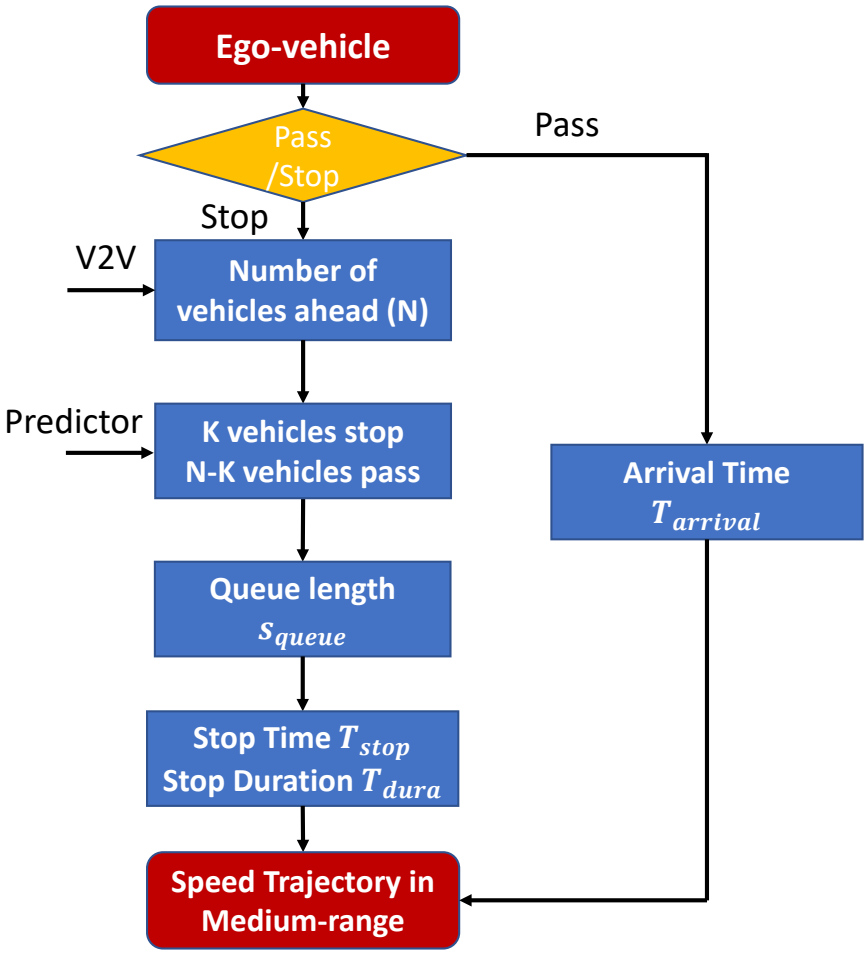

Figure 4.9: The flow chart to generate the vehicle speed trajectory in medium-range.

and as a result, K vehicles are predicted to stop and the remaining $N-K$ vehicles pass. With K being the number of vehicles in the queue, s_{queue} can be estimated assuming that every vehicle adds a fixed length to the queue. Additionally, the dependence of s_{queue} on T_{queue} based on Plymouth Rd vehicle data is shown in Fig. 4.10. It can be observed that the relationship can be reasonably represented by a second order polynomial, $T_{queue} = as_{queue}^2 + bs_{queue} + c$. Then, T_{stop} and T_{dura} are calculated using equations (4.3) and (4.4), and the vehicle speed trajectory is predicted using the model in Fig. 4.7-(a).

To implement the above approach, the prediction of the passing/stopping event

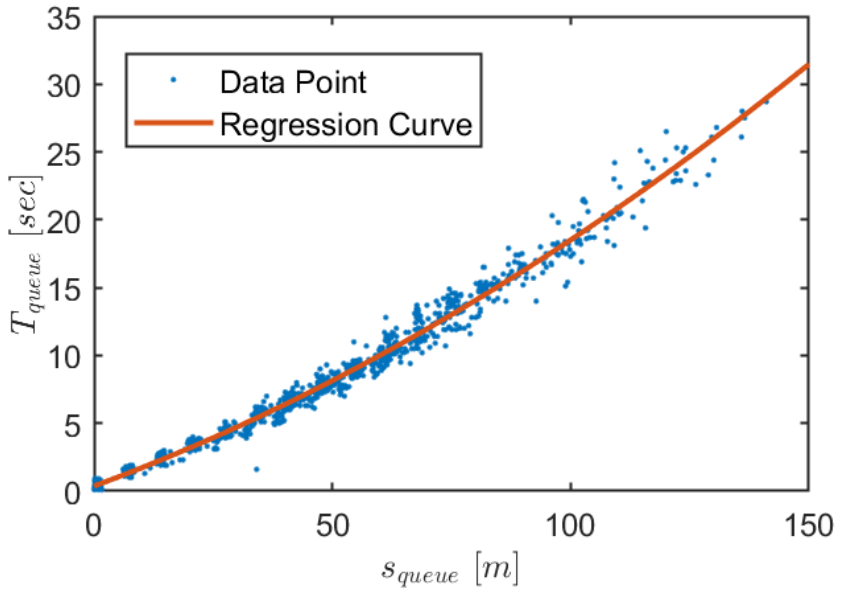

Figure 4.10: The relationship between queue length (s_{queue}) and the discharge time of queue (T_{queue}).

is required. The algorithm shown in Fig. 4.9 is generic and is not restricted to a particular model to predict the passing/stopping event. In this study, a Neural Network (NN)-based solution is used for this purpose. We propose a decentralized NN design process, in which one NN is trained for each road segment between two adjacent intersections. An alternative approach to this strategy is to develop one single centralized NN covering all the road segments. The main reason for adopting a distributed NN in this study is because it greatly helps to keep the NN structure and its training process simple and computationally fast. Moreover, since the ratio of the vehicles that may enter/exit at an intersection and the traffic flow and the length of one segment could be different than other segments, different NNs for different segments may be needed to represent traffic patterns more accurately to inform the medium range speed forecast.

The proposed NN, shown in Fig. 4.11, has 4 inputs, i.e., the current vehicle speed, trip distance (to the start point of route), trip time in the route, and current signal

timing and phase of the next intersection, and 1 output, i.e., passing/stopping at the next intersection. Note that it is assumed that the current signal phase of intersections is available by V2I communications. The NN is a feedforward network and consists of 3 hidden layers with 10 neurons each (a in Fig. 4.11). The logistic sigmoid function is used as the activation function. The NN is developed using MATLAB Deep Learning Toolbox for pattern recognition. The weight and bias values of the NN are trained with the scaled conjugate gradient method. Twenty percent of the Plymouth Rd simulation data is used to train the NN, as using a higher percentage of training data did not improve the predictions. The remaining 80% of the data is used to assess prediction accuracy, which is summarized in Table 4.1. For each intersection, one NN with the aforementioned structure is trained independently of others. Note that because all the vehicles in the data set stop at intersection IV, the accuracy of NN prediction is 100%. As compared with the BN, NN provides a better accuracy (higher than 90% for all intersections) in predicting passing/stopping events at the next intersection which inform a more accurate vehicle speed forecast over a medium range.

Table 4.1: The accuracy of NN in predicting passing/stopping events at 6 intersections.

Intersection Number	**I**	**II**	**III**	**IV**	**V**	**VI**
Accuracy [%]	97.3	99.4	94.9	100.0	94.8	99.1

Remark 4.2: The proposed long-range speed prediction approach based on the BN's branch with the highest probability is computationally very fast and can be updated in real-time. However, there might be branches with slightly smaller probabilities that will not be picked up as the long-term preview by the BN. The integration of the medium-range preview could compensate for such scenarios. For example, if based on the most probable driving scenario, a vehicle is predicted to "pass" an upcoming intersection, but the medium-range predictor estimates it to "stop", then in the final speed preview, the "stop" event is accepted as the more reliable prediction.

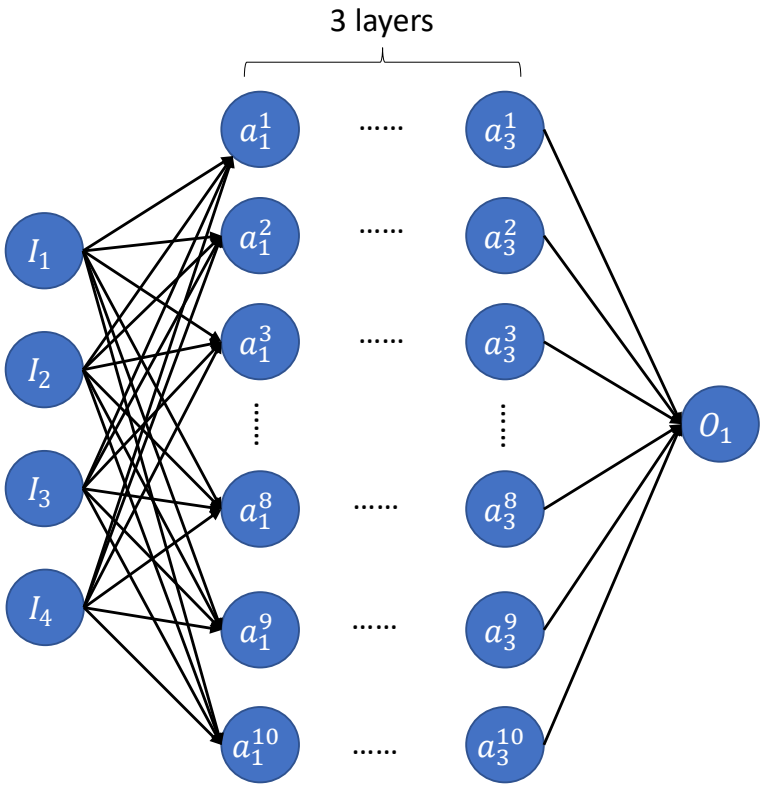

Figure 4.11: The structure of NN designed in medium-range preview.

4.2 Combine Multi-range Vehicle Speed Prediction with MH-MPC for iPTM of HEVs

In order to assess the benefits of the proposed framework, the multi-range vehicle speed prediction strategy is applied to enable the iPTM of MH-MPC. Three cases shown in Fig. 4.12, are considered over the long shrinking horizon as following:

- **Case A**: The vehicle speed over the long shrinking horizon is assumed to be constant and equal to the current cruise speed.
- **Case B**: The BN is used to provide the vehicle speed trajectory until the end of the trip.

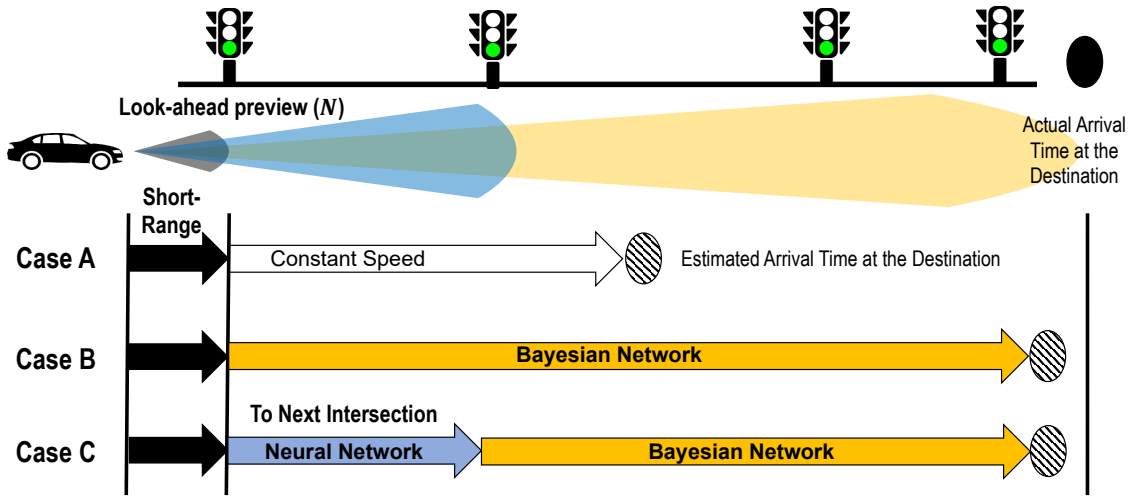

Figure 4.12: The three cases (A, B, and C) defined to evaluate the performance of MH-MPC with different types of information incorporated in the look-ahead.

- **Case C**: On the basis of Case B, the vehicle speed preview in the medium-range is enhanced by the NN while BN provides the vehicle speed prediction beyond the next intersection to the end of the trip.

Fig. 4.12 illustrates the concepts of Cases A, B and C. Note that in all three cases, the vehicle speed prediction over the short-range horizon (i.e., the receding horizon $N = 5$ *sec*) is assumed to be accurate. For Case A, the cruise speed in the long-range horizon varies at different segments of the corridor, specifically, it is around 15.6 m/s from intersection I to V, and 20.8 m/s after intersection V. The trip end time is estimated based on the remaining distance and estimated vehicle speed profile, which will be updated each time when the estimated vehicle speed is updated.

Fig. 4.12 shows how the predicted speeds over different ranges from Fig. 4.1 are combined for implementation in MH-MPC for iPTM. In Case C, while the predicted speed over the medium range is already available from the BN, the more accurate prediction obtained from the NN is used.

In order to analyze the performance of MH-MPC for three cases defined above, 140 vehicles are randomly selected among all the vehicles traveling through the entire

corridor. The initial conditions of states (SOC and T_{cl}), ambient temperature, and cabin heating demands are set to be the same for all the vehicles. The results of applying an offline DP are used as the benchmark [104] to show how the uncertainty and lack of information about the speed preview degrade the fuel consumption from its optimal value, thereby demonstrating how the proposed speed prediction framework helps to stay close to the global optimal solution. Fig 4.13 shows the probability density functions for fuel consumption increase of Cases A, B, and C as compared to DP solution. Note that for DP implementation, it is assumed that the entire vehicle speed is known a priori with a sampling period of 1 *sec*. To compute the probability densities in Fig 4.13, we have used `ksdensity` function in MATLAB, which returns a kernel distribution through a nonparametric representation of the probability density function of a random variable [105]. In our case, the random variable is the fuel consumption increase percentage from the simulated vehicles as compared to the DP solution. The detailed analysis reveals the following insights:

First, the mean value of fuel consumption increase in Case B is 2.04%, which is 0.37% lower than Case A. It shows that by enhancing the vehicle speed prediction over the long shrinking horizon using the BN, the MH-MPC can improve fuel consumption.

Moreover, the addition of medium-range speed prediction (Case C) enhances the fuel consumption by 0.9% on average as compared to Case B. In this case, 0.9% is nearly half the distance between case B and DP, meaning that Case C provides significant incremental benefits of 50%, as compared to Case B. Given the higher probability density of Case C, as compared to Case B. Fig 4.13 suggests that an improved prediction of vehicle speed and passing/stopping events in the medium-range provides extra fuel savings. Overall, while a long prediction horizon is needed given the slow responding thermal dynamics of the system, further refining the speed prediction in the medium range provides significant incremental benefits without the complexity of refining the entire long horizon.

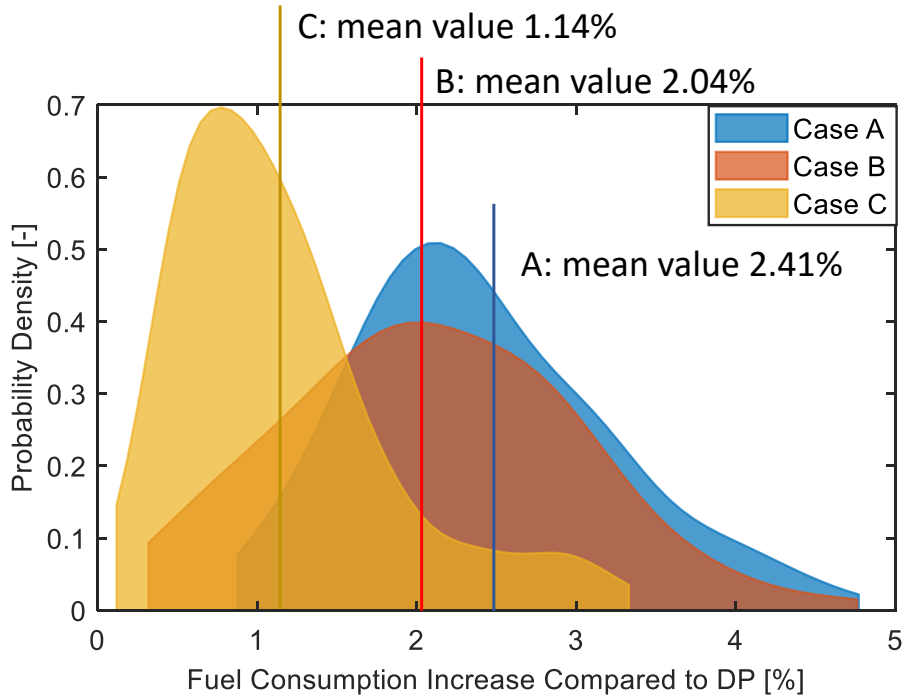

Figure 4.13: The probability density function of the fuel consumption increase from Cases A, B, and C.

In order to investigate the sensitivity of fuel consumption to the errors in the speed forecast, we consider two vehicles following two different branches of the BN (i.e., Vehicle #1 from Branch 5 and #2 from Branch 3). Fig. 4.14 shows the predicted vehicle speed profiles of these two vehicles, before they approach intersection III. According to the BN, before intersection III, Branch 5 has the highest probability for both vehicles. One can see that while the BN predicts all the passing/stopping events for Vehicle #1 correctly, it mis-predicts the event for Vehicle #2 at intersection III ($t = 170$ *sec*), see Fig. 4.14-(b).

Fig. 4.15 shows the fuel consumption of these two vehicles. It can be seen that, as compared to DP, the fuel consumption is larger in Case A by 2.25% and 2.93% for vehicles #1 and #2, respectively. Additionally, as compared to Case C, in Case B the fuel consumption is increased by 0.51% and 0.90% for vehicles #1 and #2, respectively.

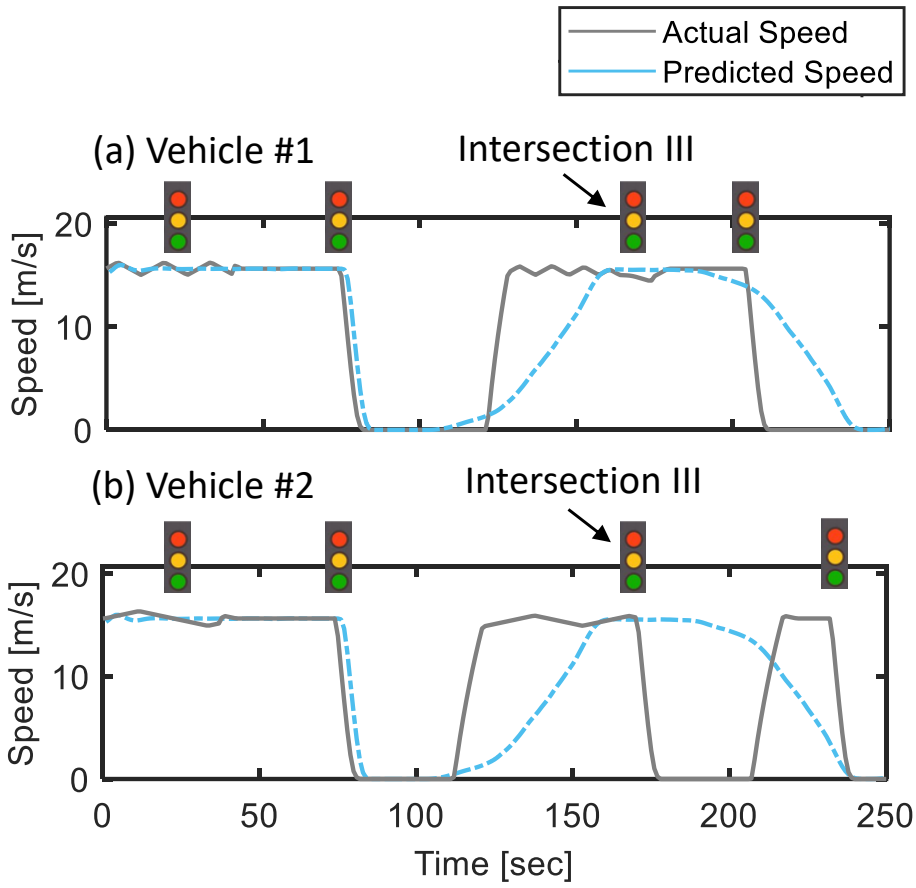

Figure 4.14: The comparison of actual and predicted vehicle speed profiles before the vehicle approaches intersection III (a) Vehicle #1 and (b) Vehicle #2.

The state trajectories of two vehicles are shown in Figs. 4.16 and 4.17. It can be seen that the SOC and T_{cl} trajectories show a similar trend for all cases. At the beginning of the trip, when T_{cl} is not warm enough, i.e., around 50 ^oC, the engine is used to meet the traction power demand and at the same time, charge the battery. While SOC is pushed towards its upper limit, i.e. 80 %, T_{cl} rises to around 60 ^oC. Note that when the T_{cl} is lower than 60 ^oC, the engine efficiency degrades significantly [45]. Therefore, by running the engine at a higher load, the controller is able to warm up the engine faster to enable fuel savings later during the drive. Note that, in order to fully recuperate the kinetic energy during braking, as shown in Figs 4.16-(b) and 4.17-(b), the controller uses the battery to satisfy traction power

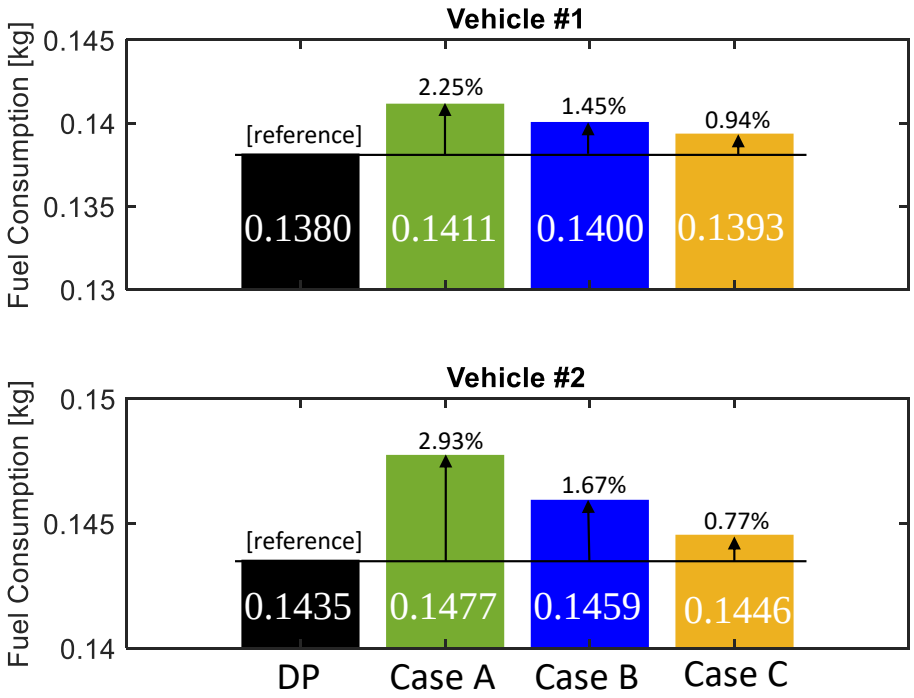

Figure 4.15: Fuel consumption of DP, Case A, B and C.

demand prior to a stop/braking event. The subsequent reduction in SOC increases the amount of regenerative braking energy that can be recovered before reaching the maximum SOC constraint. Enabling this energy recovery requires the controller to accurately predict the upcoming stop/braking event. For Case A, the controller cannot detect the stop event until the intersection is within the short receding horizon, leaving insufficient time for battery discharge. Therefore, the kinetic energy during braking phases is not fully recuperated in Case A. Moreover, for Vehicle #2, the BN makes a mis-prediction at intersection III (around 170 sec) and in Case B, the stop is not detected in advance, and thus, the energy is not fully recuperated during braking.

4.3 Summary

In this chapter, a novel data-driven multi-range vehicle speed prediction strategy was proposed for urban corridors with signalized intersections. The proposed strategy

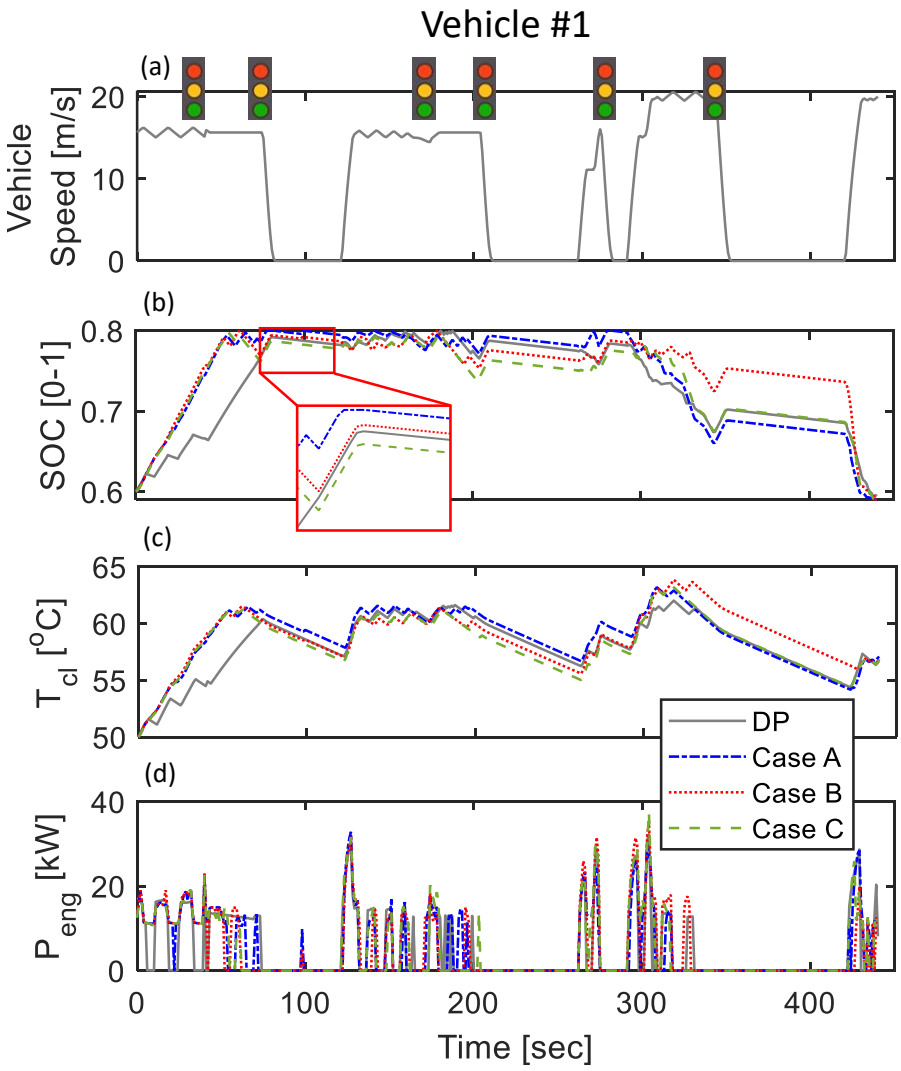

Figure 4.16: State trajectories for Vehicle #1: (a) vehicle speed, (b) battery SOC, (c) coolant temperature, and (d) engine power.

exploits historical traffic data collected from connected vehicles to provide prediction of vehicle speed over short range, medium range and long range. Over the short-range horizon, the vehicle speed prediction is obtained based on V2V/I communication, which is assumed of high accuracy. Over the long-range horizon, a Bayesian Network (BN) provides the vehicle speed prediction and estimates the most probable driving scenario until the end of the trip. The medium range prediction (from the end of the short-range to the next intersection) exploits a Neural Network (NN) that is able to

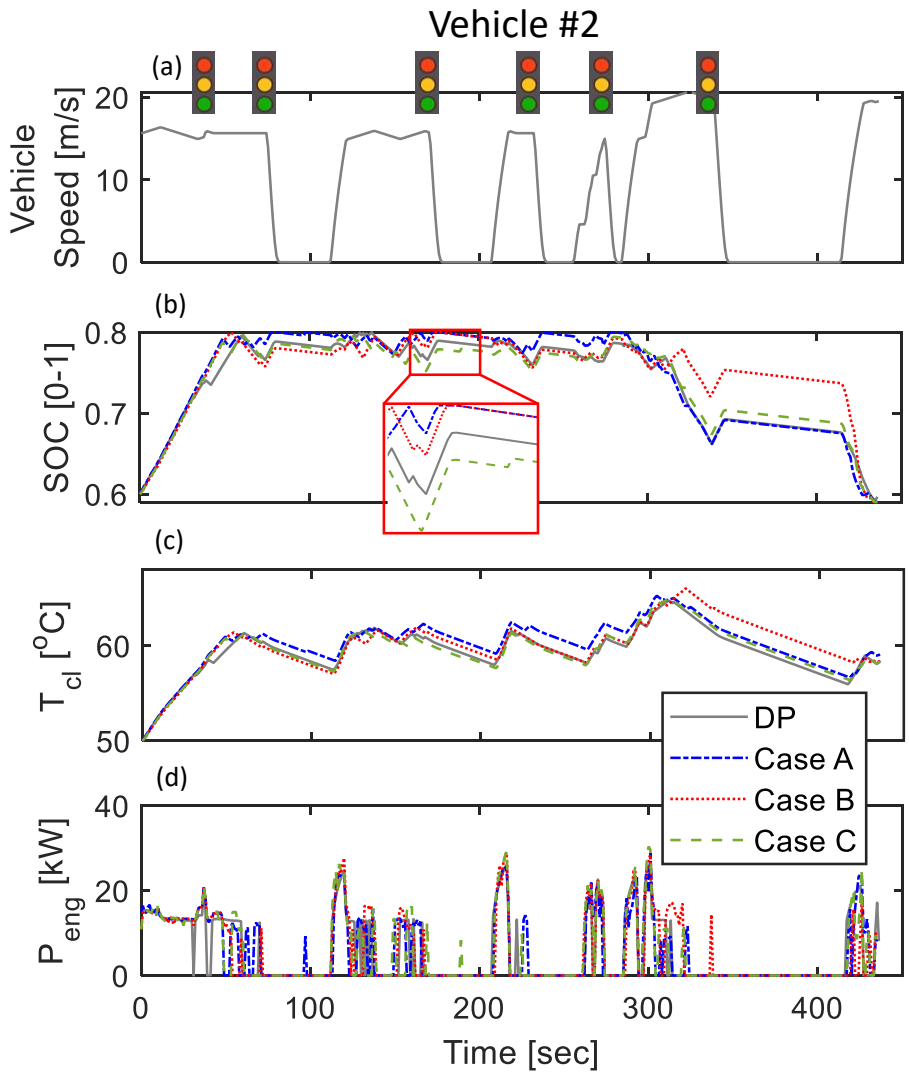

Figure 4.17: State trajectories for Vehicle #2: (a) vehicle speed, (b) battery SOC, (c) coolant temperature, and (d) engine power.

forecast the passing/stopping event at the next intersection with 90 % accuracy based on the validation data. Then the medium range vehicle speed trajectory forecast is informed by exploiting the prediction of passing/stopping event and estimates of the queue length and stop/arrival time.

The effectiveness of the proposed vehicle speed prediction framework was demonstrated by exploiting it for vehicle speed preview in a multi-horizon model predictive control (MH-MPC) scheme used for HEV integrated power and thermal manage-

ment (iPTM). The MH-MPC exploits a short receding horizon and longer shrinking horizon that extends to the end of the trip. The vehicle speed preview over the receding horizon is informed by V2V/V2I- based short range vehicle speed prediction, while NN and BN-based approaches are used to inform the vehicle speed preview over the shrinking horizon. The simulation results show that, by incorporating the medium- and long-range speed preview, the MH-MPC achieves a fuel consumption within 1.0 % deviation from the offline Dynamic Programming solution. Furthermore, the sensitivity analysis revealed that by enhancing the accuracy of predicting the passing/stopping events, the performance of MH-MPC can be improved. Compared with constant vehicle speed preview, the proposed multi-range vehicle speed prediction reduces the fuel consumption by around 1.28 %.

CHAPTER V

Robust Power and Thermal Management of Electric Vehicles using Model Predictive Control

In chapter III, we developed MH-MPC for iPTM of HEVs and identified the major traffic events that needed to be predicted using sensitivity analysis. In chapter IV, in order to predict the important traffic events, the multi-range vehicle speed prediction approach was proposed over different prediction horizons. The benefits of the proposed approach was assessed by combining it with the MH-MPC for iPTM of HEVs.

In this chapter, the MPC-based iPTM framework is expanded for EVs to improve energy efficiency by optimizing the thermal responses, e.g., battery and cabin temperatures. Similar to the iPTM of HEVs, the relatively slow dynamics of thermal systems in EVs also call for a long-range prediction horizon to achieve the desired performance, and the errors in vehicle speed prediction can be detrimental to achieving the optimal performance of the battery TMS. However, there are two main differences between the iPTM of HEVs and EVs. First, as all the power consumed for traction and auxiliary systems of EVs are eventually provided by the battery, there is no need to optimize the power split between the battery and engine. Second, the charging sustaining condition is no longer required for EVs. Therefore, the MPC formulation developed for the iPTM of HEVs needs to be properly adjusted, and the focus of this

study is to improve the robustness of the MPC-based iPTM approach for EVs with the uncertainties of preview information.

To this end, we first determine the key traffic preview information required over the prediction horizon. Then, the impact of preview uncertainties on the optimal performance is evaluated. Finally, the algorithm is modified to further improve the robustness of the MPC-based thermal management algorithm in the presence of inevitable uncertainties associated with traffic/vehicle speed predictions.

5.1 Problem Formulation

We consider an EV operating with hot ambient temperatures. Fig. 5.1 depicts a schematic of the integrated thermal management system of an EV, which consists of the refrigerant loop, as well as cabin and battery cooling loops. The refrigerant absorbs heat from the battery and cabin coolant, while the out heat exchanger (OHE) dissipates the absorbed heat to the ambient. The battery and cabin coolant is circulated by an electric pump through the combined cabin and battery loops. The cool-down phase is not considered in this study. The objective of MPC-based thermal management strategy (TMS) is to minimize the energy consumption while enforcing the thermal constraints, i.e., battery and cabin temperature constraints.

5.2 MPC-based Power and Thermal Management of an EV

5.2.1 MPC Formulation

To reduce the energy consumption by TMS and enforce the constraints on thermal states and control inputs, our MPC approach is based on the following discrete-time finite horizon optimal control problem:

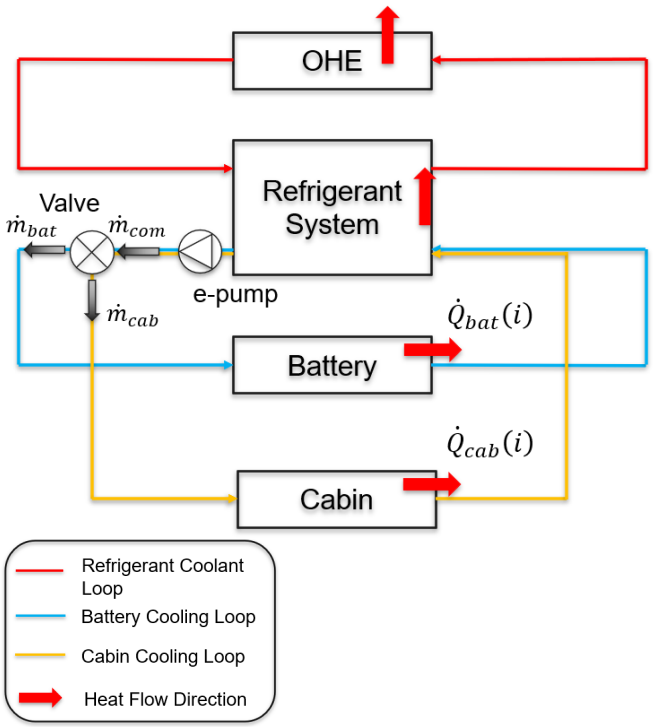

Figure 5.1: Schematic of the integrated thermal management system of an EV.

$$
\begin{aligned}
\underset{\dot{m}_{com}(i),r(i)}{\arg\min} \quad & \sum_{i=t}^{t+N-1} \{(\dot{Q}_{cab}(i) + \dot{Q}_{bat}(i))/COP + a_1\epsilon_1^2 + a_2\epsilon_2^2 \\
& + b_1\Delta\dot{m}_{com}(i) + b_2\Delta r(i)\}, \\
\text{s.t.} \quad & T_{bat}(i+1) = T_{bat}(i) + f_{bat}(i)\Delta t, \\
& T_{cab}(i+1) = T_{cab}(i) + f_{cab}(i)\Delta t, \\
& \dot{Q}_{bat}(i) = \alpha(\dot{m}_{bat}(i))(T_{bat}(i) - T_{cl,out}), \\
& \dot{Q}_{cab}(i) = \beta(\dot{m}_{cab}(i))(T_{cab}(i) - T_{cl,out}), \\
& T_{bat,min} \leq T_{bat}(i) \leq T_{bat,max} + \epsilon_2, \\
& T_{cab,min} \leq T_{cab}(i) \leq T_{cab,max} + \epsilon_1, \\
& 0 \leq \dot{m}_{com}(i) \leq \dot{m}_{max}, \\
& 0 \leq r(i) \leq 1,
\end{aligned}
\tag{5.1}
$$

where f_{bat} and f_{cab} are defined in (2.7) and (2.8), respectively. The details and the variables defined for the integrated thermal management system have been presented in Section **??**. Δt is the sampling time, and $H = N\Delta t$ is the prediction horizon length. The cost function in (6.1) consists of three terms: (i) the power consumption for cabin and battery cooling, (ii) penalty on slack variables, ϵ_1 and ϵ_2, which relax T_{cab} and T_{bat} upper bounds, and (iii) penalty terms for the rate of change of control variables, $\dot{m}_{com}$ and r.

Remark 5.1: The rate of change is penalized for physical considerations. Firstly, the inertia of the compressor and valve in the TMS does not allow a rapid change in the coolant flow rate and split ratio. Secondly, the rapid change of cabin cooling power could be perceived unfavorably to passengers' comfort.

5.2.2 Impact of Prediction Horizon Length on MPC-based TMS Performance

In this study, the MPC formulated in Section 5.2.1 is applied to a commercial electrical vehicle. For the case study, the initial cabin and battery temperatures are 25^oC and 34^oC, respectively, which are already within their desired operation ranges. The lower and upper bounds on T_{cab} are set as 24^oC and 25^oC, respectively, assuming that the cabin temperature setpoint is set to 24.5^oC with an allowable deviation of 0.5^oC. The desired operating temperature range for the battery is from 15^oC to 35^oC, consistently with [106]. Note that the upper limits of cabin and battery temperature are soft and slack variables have been added to avoid the infeasibility of optimization problem. The sampling time, Δt, in (6.1) is chosen to be 5 *sec* and the MPC is updated every 1 *sec*. The MPC feedback law is informed by the first element of the optimal control sequence.

The relatively slow dynamics of thermal systems call for a long prediction horizon for MPC to achieve the best performance [67]. In this study, to investigate the impact

of the prediction horizon length on energy consumption and constraint enforcement, we consider two cases with different prediction horizon lengths are defined as follows:

- **Case I**: Prediction horizon length is 50 *sec*, and $T_{bat,max} = 35^oC$,
- **Case II**: Prediction horizon length is 200 *sec*, and $T_{bat,max} = 35^oC$.

Note that, in this section, it is assumed that accurate vehicle speed information over the prediction horizon is known a priori, regardless of the length of the prediction horizon. This assumption will be relaxed in the later sections when investigating the impact of uncertainties.

The simulated driving cycle, shown in Fig. 5.2-(a), combines the Environmental Protection Agency (EPA) Urban Dynamometer Driving Schedule (UDDS) with Highway Fuel Economy Test Cycle (HWFET), which includes both city and highway driving scenarios. Fig. 5.2 summarizes the simulation results. As one can see, over the entire trip, T_{cab} can be maintained in the comfort range for both Cases I and II, while multiple violations of T_{bat} can be observed for Case I when the prediction horizon is 50 *sec*. As highlighted in Fig. 5.2, such violations happen when large current is generated as the vehicle is undergoing aggressive acceleration or deceleration maneuvers. This constraint violation, if occurs often enough, may negatively impact the battery state-of-health and longevity [106]. It can be also seen from Fig. 5.2-(e) that $\dot{m}_{com}$ approaches its limit over the highlighted time periods for Case I. For Case II with a long prediction horizon (200 *sec*), MPC has more awareness of the large traction power in the near future, thus, the controller cools down T_{bat} in advance to prevent the constraint violation. Moreover, longer prediction horizon leads to more favorable enegry efficiency, as shown in Table. 5.1.

Intuitively, one simple approach to enforce the T_{bat} constraint in Case I is to tighten the upper bound of the soft constraint, $T_{bat,max}$, based on which a modified version of Case I, Case I* is defined as follows:

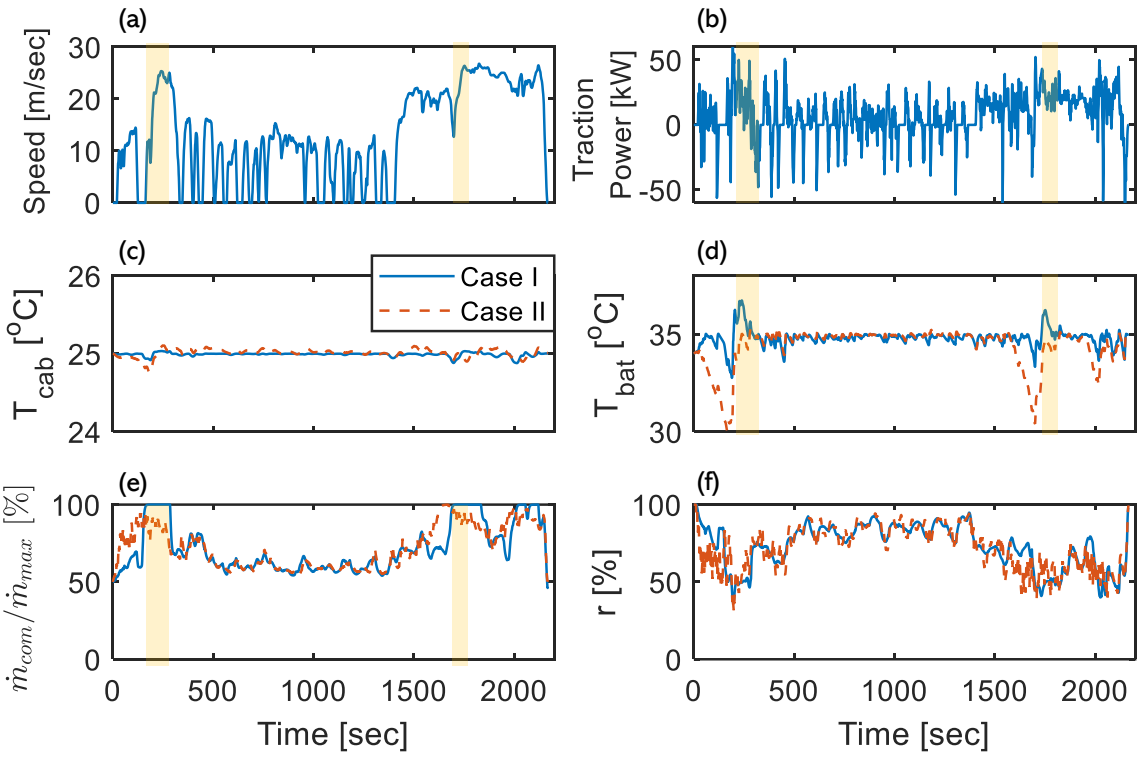

Figure 5.2: MPC results with different prediction horizons based on Cases I and II: (a) vehicle speed profile, (b) traction power profile, (c) cabin temperature, (d) battery temperature, (e) normalized coolant flow rate, and (f) coolant split ratio.

- **Case I***: Prediction horizon length is 50 *sec*, and $T_{bat,max} = 33^oC$,

Note that $T_{bat,max}$ is reduced by 2 ^oC in Case I* according to the maximum constraint violation observed in Fig. 5.2-(d), while no constraint tightening is applied to Case II. Fig. 5.3 presents the simulation results of Case I*. It can be observed that by tightening the upper bound of the soft constraint, T_{bat} constraint can be successfully enforced over the entire trip for Case I*. However, the conservative approach leads to extra energy consumption for the TMS, as shown in Table 5.1. It can be seen that compared to Case I, Case I* consumes 9.4% and 1.1% more energy for battery (J_{bat}) and cabin (J_{cab}) cooling, respectively. Moreover, Case II achieves the best energy efficiency among all three cases with good enforcement of thermal constraints over the entire trip, thanks to the long-range prediction horizon. The above analyses demonstrate that for the MPC-based thermal management for an EV, a longer prediction

Table 5.1: The energy consumption for the thermal management system computed for Cases I, I*, II, and III.

Case	**I**	**I***	**II**	**III**
J_{bat} $[kJ]$	1339.1	1465.1	1314.7	1316.5
J_{cab} $[kJ]$	4477.4	4526.7	4458.8	4460.4
J_{total} $[kJ]$	5816.5	5991.8	5773.5	5776.9
Computational Time $(Avarage)$ $[sec]$	0.20	0.21	0.53	0.26
Computational Time $(Worst)$ $[sec]$	0.36	0.40	0.72	0.72

horizon allows a less conservative strategy to enforce the thermal constraints while providing better energy efficiency for this use case.

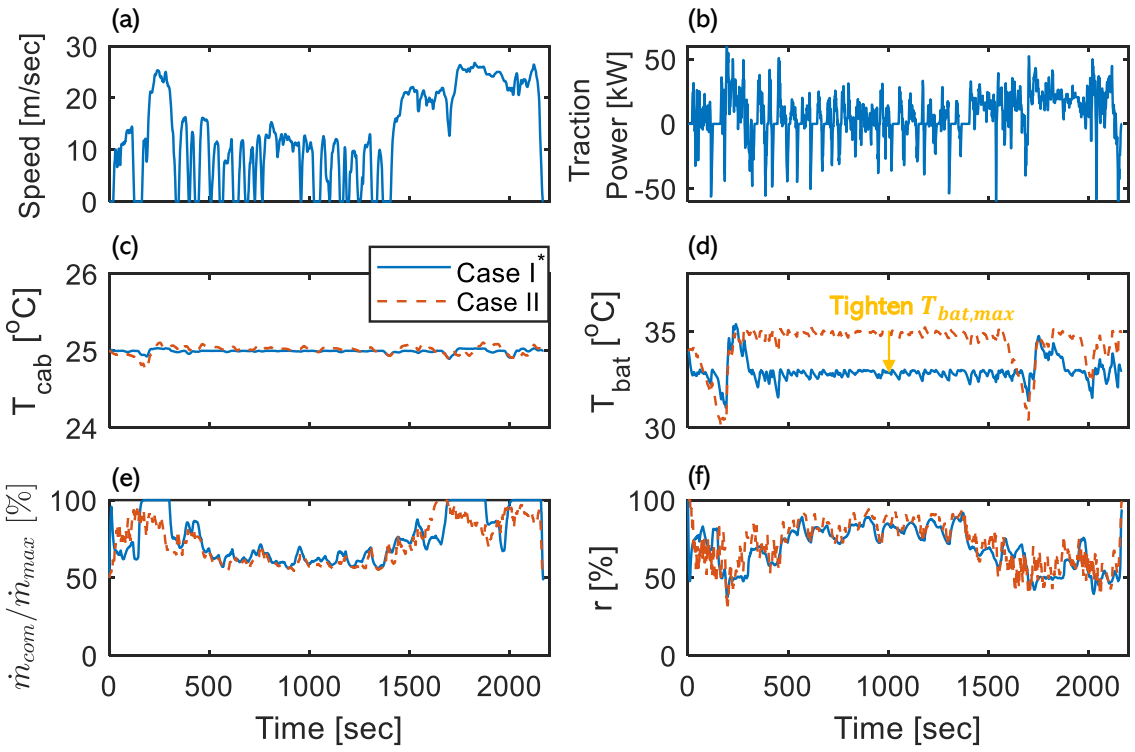

Figure 5.3: MPC results with different prediction horizons based on Cases I* and II: (a) vehicle speed profile, (b) traction power profile, (c) cabin temperature, (d) battery temperature, (e) normalized coolant flow rate, and (f) coolant split ratio.

5.2.3 Key Features in the Speed Preview

It can be seen from Fig. 5.2-(d) that the optimal T_{bat} trajectories are considerable different for different prediction horizons only when there is a large change in traction power. If there is no such event, e.g., from t=500 *sec* to 1500 *sec*, Case I and II exhibit similar results for T_{bat}, and extending the prediction horizon doesn't improve energy efficiency and constraint enforcement. This case study identifies the large traction power associated with aggressive acceleration and deceleration maneuvers as one of the key events that significantly impact performance and therefore should be captured in the speed preview.

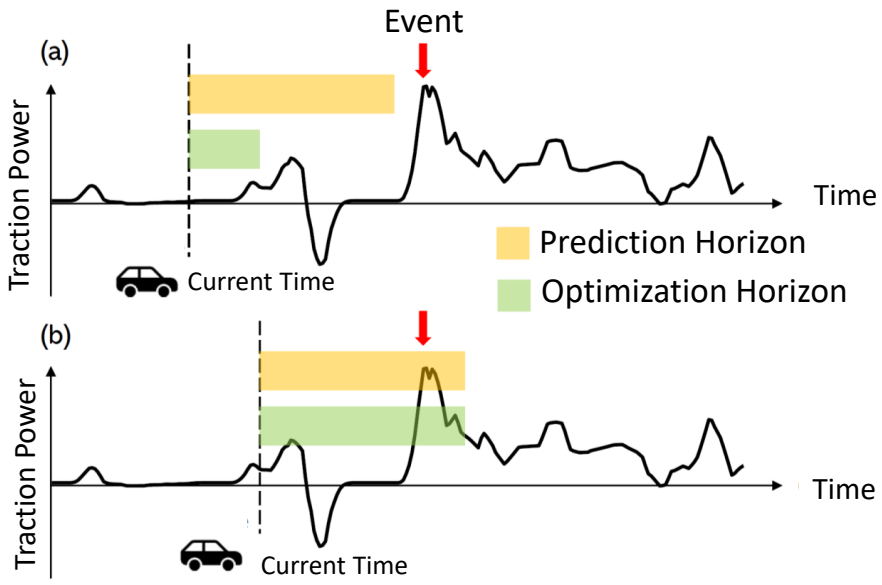

Figure 5.4: Concept of Case III: (a) when the key "event" of large traction power is not detected over the prediction horizon, a short horizon is adopted for MPC, and (b) when the key "event" is detected within the prediction horizon, a long optimization horizon is adopted.

To capture the significant events over the long prediction horizon without being over-burdened with computation, we propose the concept of adaptive optimization horizon, as presented in Fig. 5.4. A long prediction horizon is applied to cover the key speed events, and if such event is not detected over the prediction horizon, as shown in

Fig. 5.4-(a), a short-range optimization horizon is applied to the MPC problem (6.1). Whereas, if the key "event" is predicted to occur within the prediction horizon, as shown in Fig. 5.4-(b), a long optimization horizon is applied to (6.1). To demonstrate the impact of the adaptive prediction horizon, a new case study (Case III) with adaptive prediction horizon length is considered as follows:

- **Case III**: Adaptive optimization horizon length, and $T_{bat,max} = 35^oC$,

In this study, the long and short prediction horizon lengths are set as 200 *sec* and 50 *sec*, respectively. The simulation results of Case III are presented in Fig. 5.5, and the energy consumption results are summarized in Table-5.1. It can be seen that Cases II and III provide a similar trajectory of T_{bat} and energy consumption, which confirms that the long-range optimization horizon is only needed when the key events occur over the prediction horizon. Moreover, Table. 5.1 summarizes the computational footprint of different cases. It can be seen that by leveraging adaptive optimization horizon strategy the average computational time of solve the optimization problem (6.1) can be reduced. Therefore, the proposed adaptive optimization horizon length strategy reduces the average computational cost without compromising performance. Note that although the average computational time is reduced, for practice implementation, the computational requirement is usually determined by the worst case, which has not been reduced by the proposed strategy.

5.3 Robustness of MPC-based Thermal Management against Uncertainties in Vehicle Speed Preview

For the analysis in Section 5.2, an accurate speed preview over the prediction horizon is assumed, which is not realistic, particularly when the prediction horizon is relatively long. In this section, we evaluate the robustness of the MPC-based TMS performance against the errors in forecasting the speed-related key events. Focusing

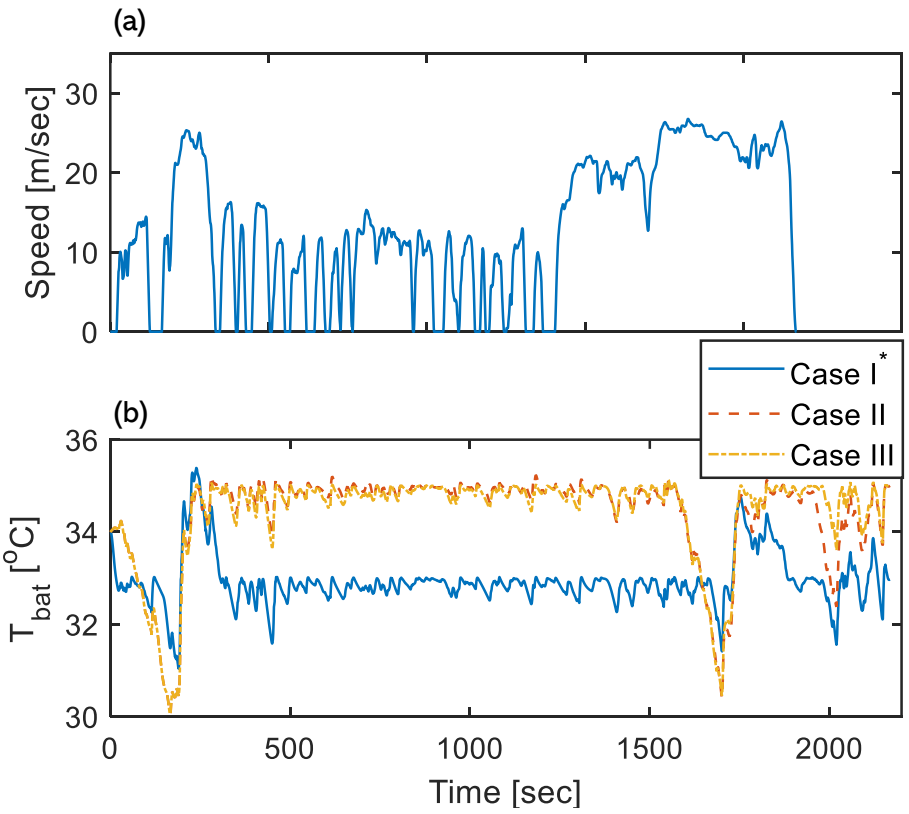

Figure 5.5: MPC results of Cases I*, II, and III: (a) vehicle speed profile, and (b) battery temperature.

on the impactful period of high traction power, we consider two different types of uncertainties, as shown in Fig. 5.6. Namely the over- and under-estimation of the magnitude (Fig. 5.6-(a)) and the wrong prediction of the timing (Fig. 5.6-(b)). As vehicle acceleration occurs after a stop, difficulties in estimating the stop time will lead to errors in predicting the time of acceleration. While both types of uncertainties are unavoidable in real application, we consider them separately in this study.

To study the impact of the first type of uncertainty, three cases are defined as follows:

- **Case A**: The preview information is accurate,
- **Case B**: The traction power during the concerned event period is 30% over-estimated,

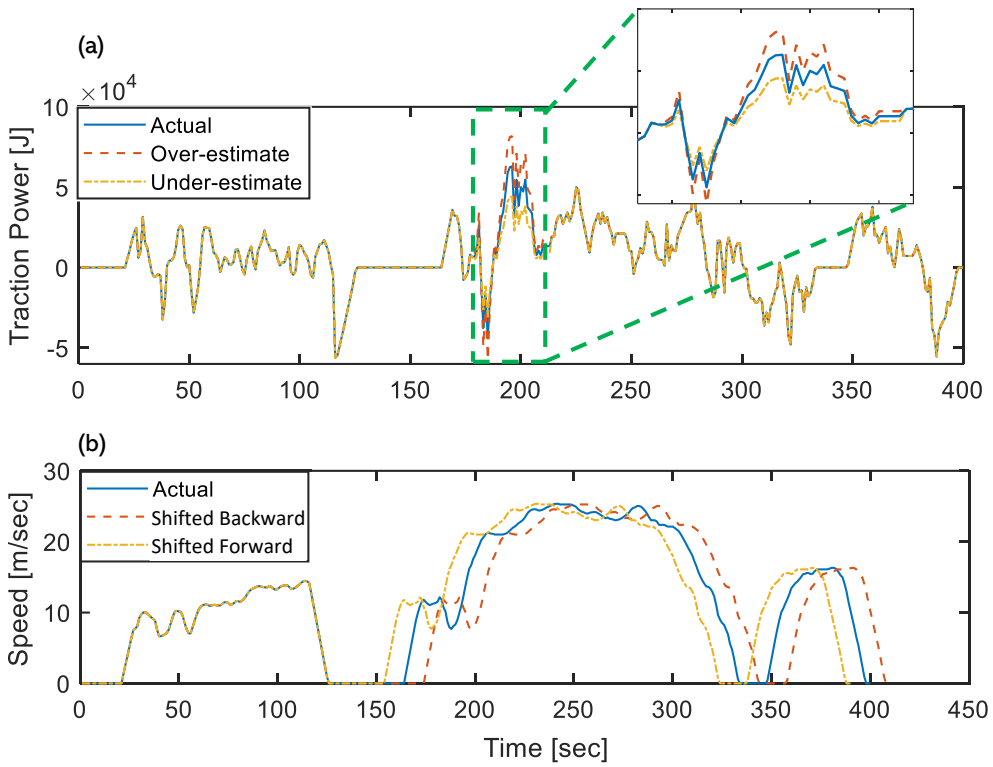

Figure 5.6: Concept of two types of uncertainties: (a) the event magnitude (traction power) is over- or under-estimated, and (b) the event timing is shifted backward and forward.

- **Case C**: The traction power during the concerned event period is 30% under-estimated.

For all three cases, the prediction horizon is set to 200 *sec*. The simulation results are presented in Fig. 5.7. With accurate preview information, T_{bat} constraint of Case A is enforced by pre-cooling the battery before the upcoming aggressive acceleration event. Compared to Case A, in Case B, T_{bat} magnitude decreases to a lower value, because the traction power is over-estimated, and accordingly, more internal heat is predicted to be generated during the event period. Conversely, due to the underestimation of the traction power, in Case C, TMS does not provide enough pre-cooling for T_{cab}, which results in the constraint violation after the event. The energy consumption and accumulated constraint violation values for with different levels of uncertainties are summarized in Fig. 5.8. Note that the negative values

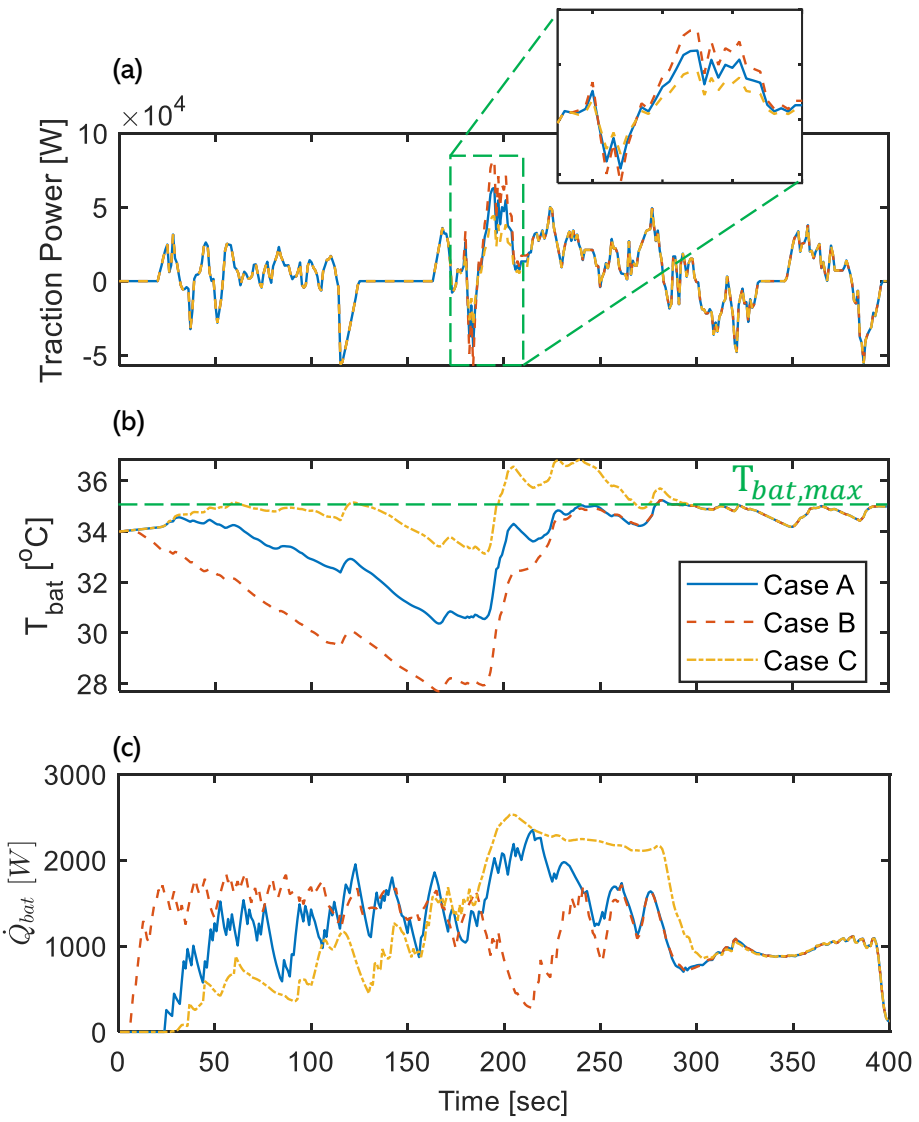

Figure 5.7: MPC-based thermal management results for Cases A, B, and C. (a) actual and predicted traction power, (b) battery temperature, and (c) battery cooling power.

reflect the levels of under-estimation on the traction power while positive values reflect over-estimation. It can be seen that Case A achieves the best energy efficiency while enforcing the constraints with accurate preview information. When the traction power is over-estimated, although no constraint violation occurs, the energy consumption for battery cooling increases as the uncertainty increases. This is because of the extra thermal load perceived by the TMS. The TMS tries to decrease T_{cab} to a lower

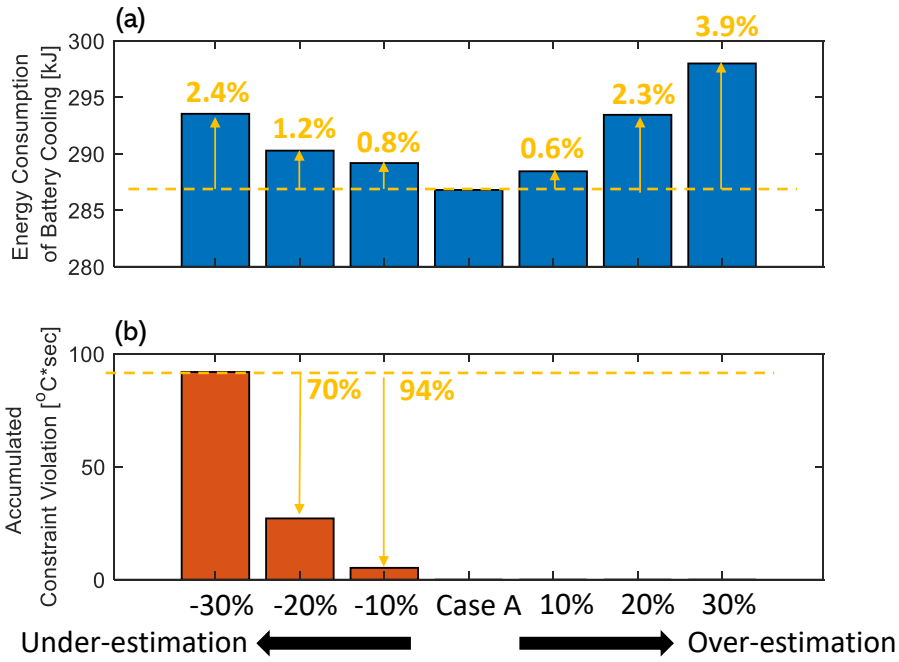

Figure 5.8: The summary of the results with different levels of uncertainties in traction power magnitude estimation (negative value for under-estimation, and positive value for over-estimation): (a) energy consumed for battery cooling, and (b) accumulated battery temperature constraint violation.

value in the pre-cooling phase, as shown in Fig. 5.7-(c). On the other hand, when the traction power is underestimated, both energy consumption and the accumulated constraint violation increase as the uncertainty increases. As shown in Fig. 5.7-(c), because Case C does not provide enough pre-cooling, when T_{bat} exceeds $T_{bat,max}$, a larger $\dot{Q}_{bat}$ is required to prevent a prolonged period of time with constraint violation, which as discussed earlier, reduces the efficiency (COP) of the TMS and leads to extra energy consumption.

To study the impact of the second type of uncertainty, the following three cases are considered:

- **Case a**: The preview information is accurate,
- **Case b**: Event timing is predicted to be 30 *sec* later than the actual time,

- **Case c**: Event timing is predicted to be 30 *sec* earlier than the actual time.

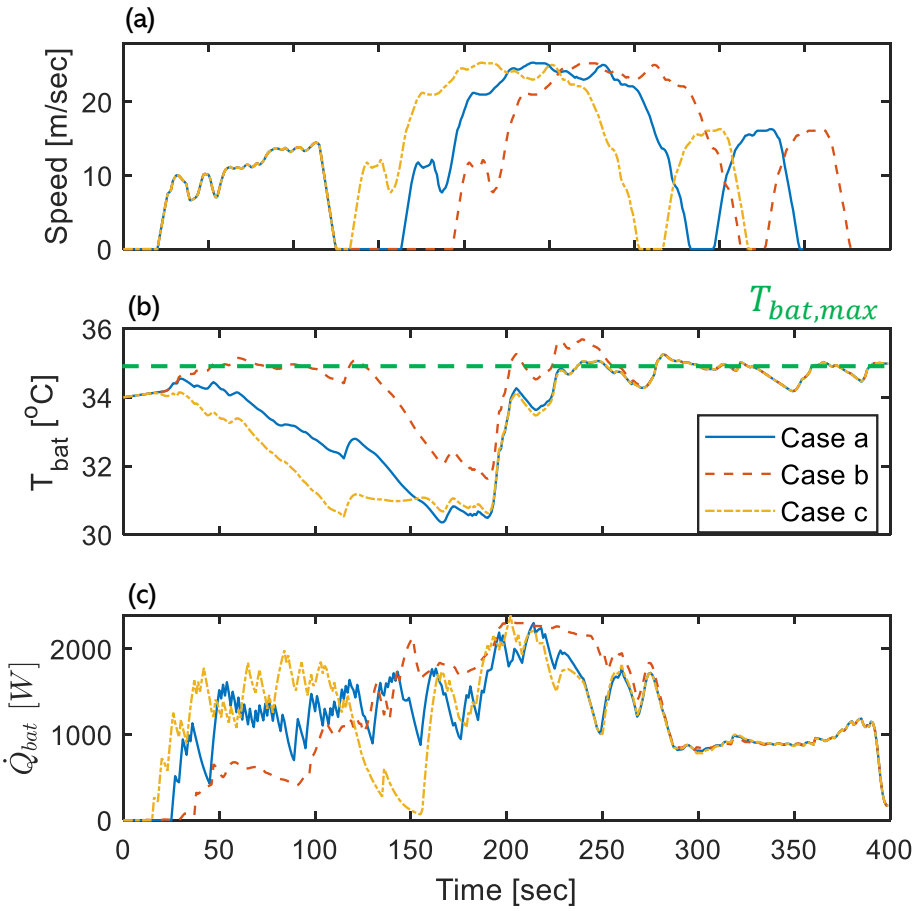

Figure 5.9: MPC-based thermal management results, for Cases a, b, and c. (a) actual and predicted traction power, (b) battery temperature, and (c) battery cooling power.

The simulation results are shown in Fig. 5.9. It can be seen that for Case b, the controller decreases T_{bat} with a delay and does not provide enough pre-cooling, which results in battery temperature constraint violation. On the other hand, for Case c, T_{bat} is first decreased and then maintained at a lower value until the high traction power event occurs. Moreover, no constraint violation is observed for Case c as Case c involves the same level of pre-cooling as Case a with accurate preview information. The energy consumption and the accumulated temperature constraint violation with different levels of uncertainties in event timing are summarized in Fig. 5.10. The negative cases represent the scenarios when the event is predicted to be earlier than

the actual high traction power event, and the positive ones are those predicted to be later than the actual event. Similar to the trend shown in Fig. 5.8, the energy consumption increases as the uncertainty increases in either direction, and constraint violation occurs only when the event is predicted to be later than the actual high traction power event.

Thus the accuracy of predicting the high traction power event can significantly affect the optimal performance of MPC-based TMS. The errors in estimating the event timing and magnitude can reduce the energy efficiency of the TMS by performing over-cooling or under-cooling prior to the event. Moreover, the failure of providing enough pre-cooling could increase constraint violation.

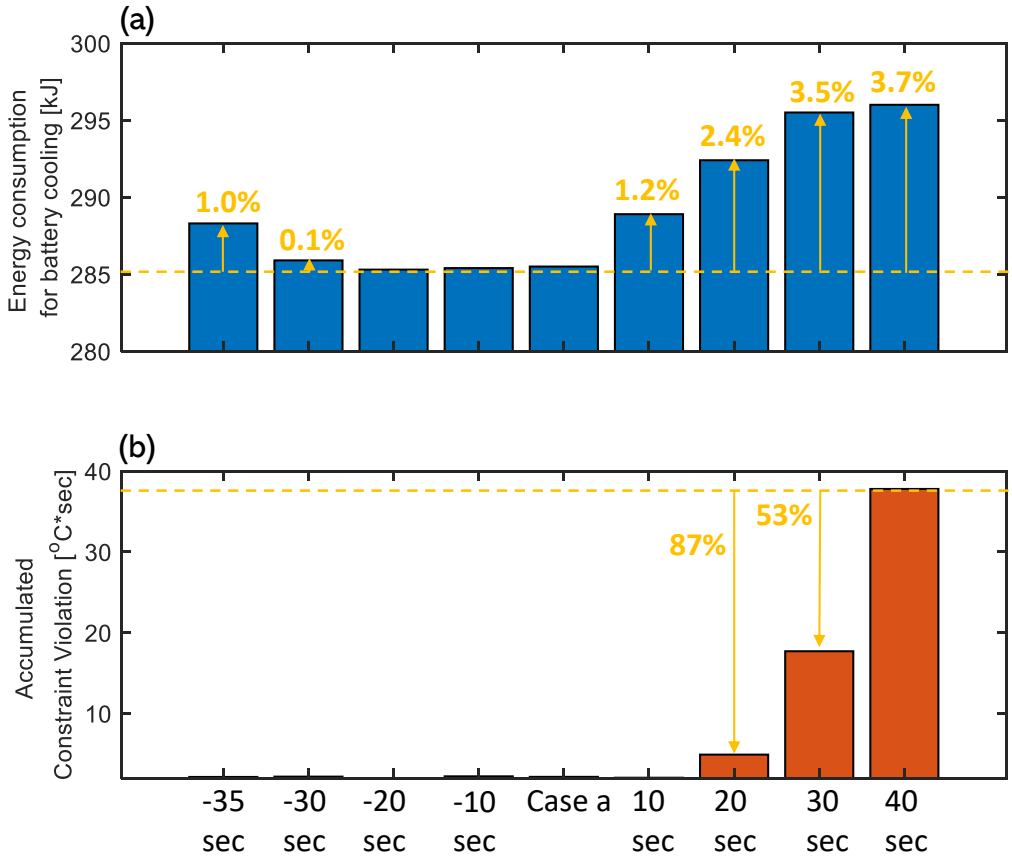

Figure 5.10: The summary of the results with different levels of uncertainties in predicting the high traction power event timing: (a) energy consumption of battery cooling and (b) accumulated constraint violation.

5.4 Evaluation of MPC-based TMS Performance Using Real-world Traffic Data

The benefits of the MPC-based thermal management for EVs were studied in Section 5.2 under the assumption that the speed preview is available. The impact of uncertainties on the TMS performance was investigated in Section 5.3, demonstrating that the errors in predicting high traction power events will diminish the benefits of predictive approach for TMS. In this section, the MPC performance is further evaluated using real-world traffic data. Based on insights gained in Section 5.3 and in this section, a strategy to enhance the robustness of the MPC-based thermal management algorithm is presented.

5.4.1 MPC Results Based on Real-world Traffic Data

In this subsection, we apply the MPC-based thermal management strategy to the commuting driving cycle data collected from a test vehicle, which was following the same route between campus and home during the commuting hours. The trips follow the exact same route with the same start and end points. Fig. 5.11 presents the simulation results of three different sample trips randomly selected from the database of over 20 trips for the same vehicle. Note that even though we assume accurate preview information over the prediction horizon, Case I, with a shorter prediction horizon, fails to enforce the T_{bat} constraint for all sample trips. The T_{bat} constraint violations happen at different times during the trip for different sample trips, and the severity of constraint violations also differs. The above observations demonstrate that even for the repeated commuting cycle data, the aggressive acceleration events have large variations in their temporal distribution, as well as in their magnitudes from one trip to another. On the other hand, although Case II enforces the constraint over the entire trip for these three trips, it requires an accurate preview information

over a long prediction horizon, which may not be available in reality. Therefore, it is important to understand the impact of uncertainties associated with such real-world traffic data and improve the robustness of the MPC-based thermal management algorithm accordingly.

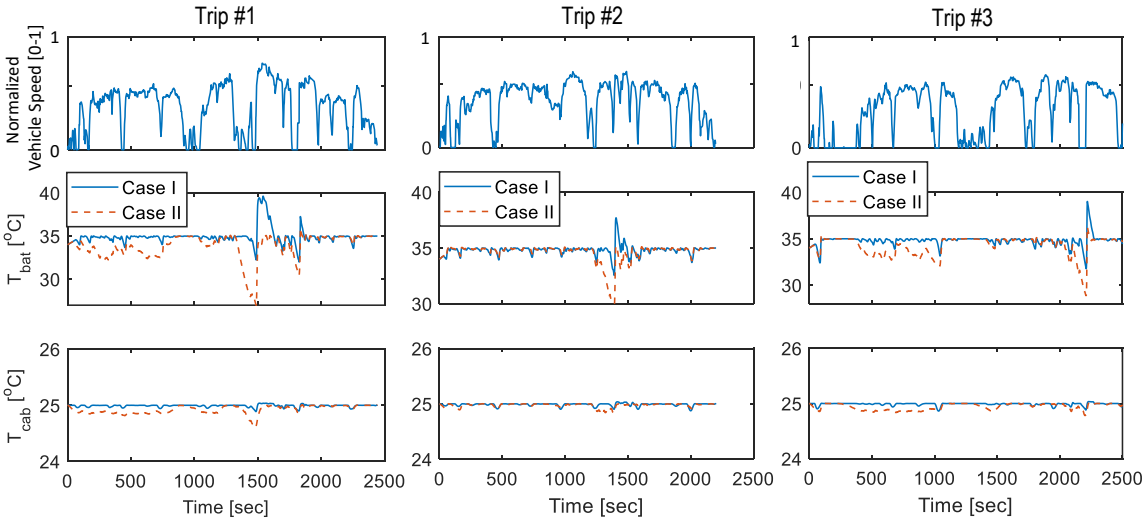

Figure 5.11: MPC-based thermal management results over three sample trips from the same test vehicle driving the same route.

5.4.2 Long-range Vehicle Speed Prediction for Implementation in MPC-based TMS

To relax the initial assumption that the vehicle speed preview is accurate, we adopt a data-driven speed prediction framework, which is built based on spatial-domain commute data. Fig. 5.12 shows the data collected from the commuting vehicle. Test category 1 represents the trip from campus to house and Test category 2 is from house to campus. The trips in one certain category share the same starting and ending points, while following the exactly same route. In order to understand the variation of these set of trips, the vehicle speed is plotted in both time domain and spatial domain.

Fig. 5.12 demonstrates that the aggregated vehicle speed in time domain exhibit

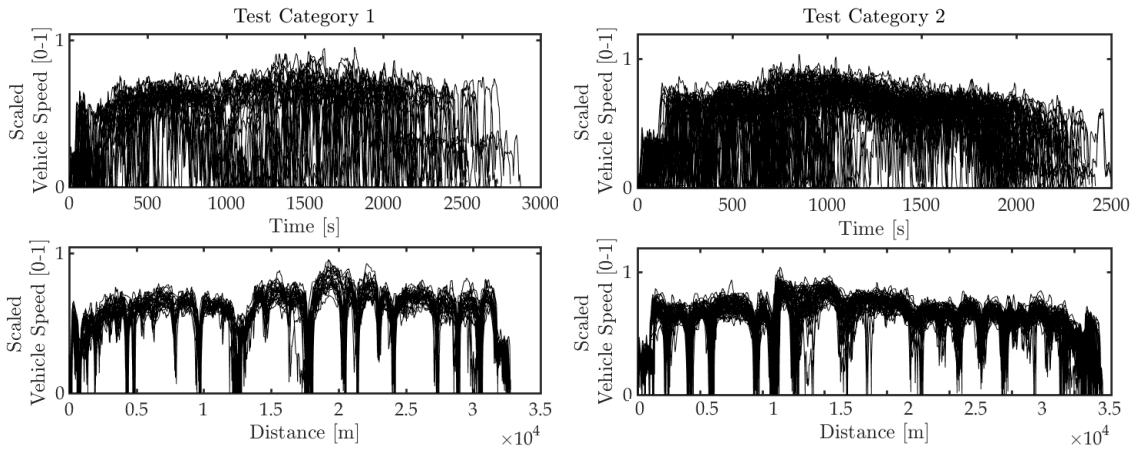

Figure 5.12: The aggregated vehicle speed trajectory of commuting data. Test category 1 represents the commuting data from campus to house while Test category 2 is from house to campus.

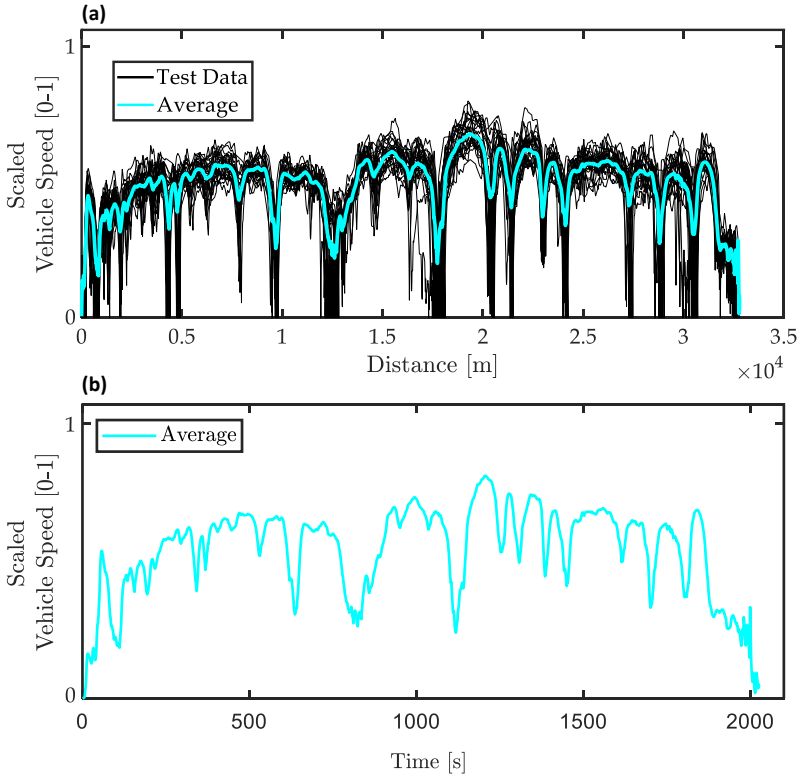

Figure 5.13: The average vehicle speed of test category 1. (a) the test data and average speed in spatial domain. (b) conversion of the average speed from spatial domain to time domain.

much larger variation, compared to that in spatial domain. The primary reason for such observation is the large variation of the stop time and stop duration. It can be seen that, in spatial domain, the vehicle speed of different trips drop at several certain locations, where the vehicle reaches the signalized intersection or stop sign. However, how long the vehicle will stop at those places varies a lot, which depends on a variety of factors, e.g., signal timing, traffic congestion level and driver's behavior. Such difference at stops accumulates along the trip, resulting in the large variation of the aggregated vehicle speed in time domain. Therefore, the vehicle speed is more predictable in the spatial domain than in the time domain. To this end, the average vehicle speed of category 1 in spatial domain plotted in Fig. 5.13-(a) provides a good estimation of the speed preview over the whole trip. Because the MPC used in this chapter is discredited and solved in time domain. Therefore, to apply such average speed to the MPC as the long-range speed prediction, there is one more step to convert it from spatial domain to time domain, as shown in Fig. 5.13-(b). To this end, the spatial-domain approach for the long-range vehicle speed prediction can be summarized as following steps:

- **Step 1**: based on the current location of the vehicle, the long-range vehicle speed is forecasted as equal to the average speed in spatial domain.
- **Step 2**: convert the vehicle speed forecast from spatial domain to time domain for the use of MPC.

As shown in Fig. 5.13, while the average speed preview captures the main trends and the location of high traction power events, it is subject to uncertainties. To investigate the impact of these uncertainties associated with real-world traffic data, three cases are considered as follows:

- **Case 1**: The preview information is accurate and the prediction horizon length is 50 sec; $T_{bat,max} = 30^oC$ over the entire trip

- **Case 2**: The preview information is accurate and the prediction horizon length is 200 sec; $T_{bat,max} = 35^oC$ over the entire trip,
- **Case 3**: The preview information is based on the average speed shown in Fig. 5.13 and is subject to uncertainties. The prediction horizon length is 200 sec; $T_{bat,max} = 35^oC$ over the entire trip.

Similar to Case I* discussed in Section 5.2-B, with a short prediction horizon, Case 1 has a tightened $T_{bat,max}$ as compared to Cases 2 and 3 to prevent constraint violation. In this case, $T_{bat,max}$ is tightened by 5^oC based on the maximum T_{bat} constraint violation observed. Since a long prediction horizon is used in Case 2 and the preview information is assumed to be accurate, there is no need to adjust upper bounds. For Case 3, we set $T_{bat,max} = 35^oC$. The state trajectories in three cases based on one sample trip from the commute data are presented in Fig. 5.14, and the energy consumption and accumulated constraint violation results are summarized in Fig. 5.15.

It can be seen from Fig. 5.15 that in both Case 1 and Case 2, T_{bat} constraint is successfully enforced over the entire trip. However, to achieve this goal, compared to Case 2, Case 1 consumes 30.1% more energy for battery cooling due to a tightened constraint. Case 1 confirms that a short prediction horizon leads to a less energy-efficient and more conservative TMS performance. On the other hand, while the long-range prediction horizon is applied to Case 3, T_{bat} constraint violation still happens. This is because of the uncertainty associated with the long-range speed preview. As presented in Fig. 5.13, although the average speed inferred in the spatial domain provides an identifiable pattern for vehicle speed profiles, it is still subject to errors due to the variance in acceleration/deceleration and the offset of stop/departure time on different work days from one trip data to another. Such errors, as discussed in Section 5.3, could degrade the MPC-based TMS performance.

The above analyses demonstrate the limitations of the existing MPC-based thermal management strategies in response to uncertainties in speed preview, specifically

over a long range which is needed for TMS. Such limitations in the baseline MPC design call for improved robustness of the optimization algorithm without making the TMS controller design conservative. To address this limitation, a location-dependent constraint handling strategy is proposed in the next sub-section.

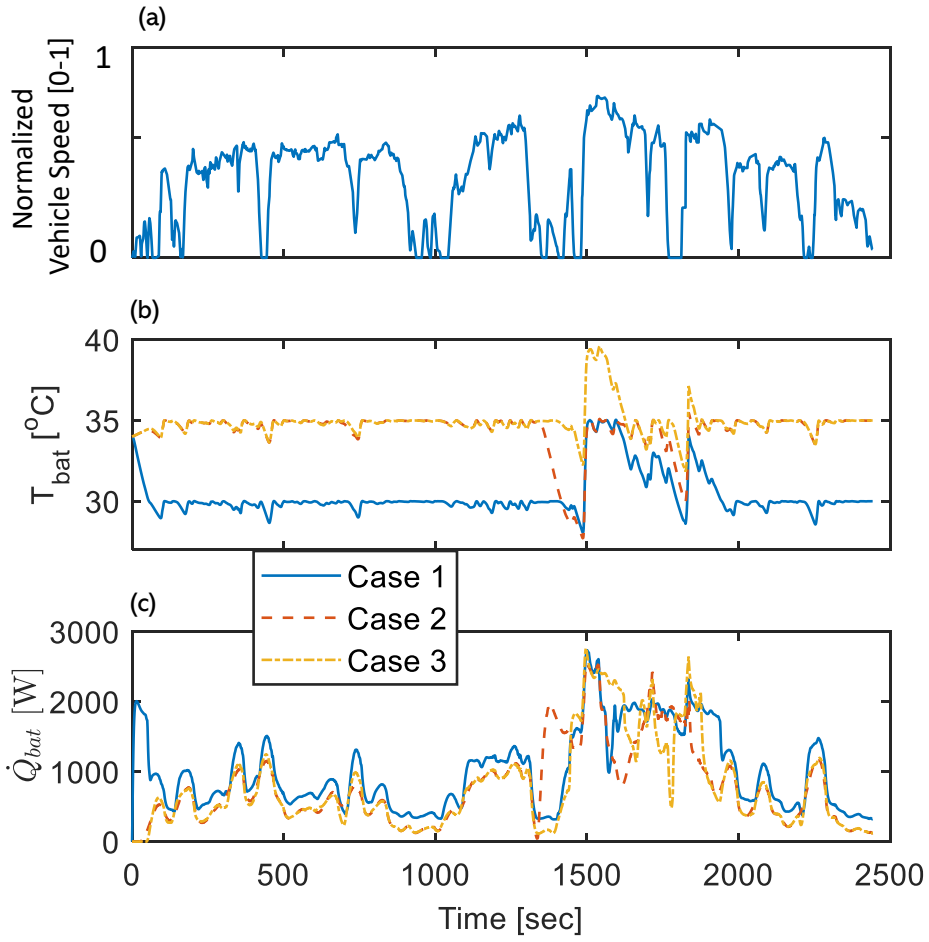

Figure 5.14: State trajectories of Cases 1, 2, and 3. (a) vehicle speed and (b) battery temperature. (c) battery cooling power.

5.4.3 Location-dependent Thermal Constraint for Improved MPC Robustness

As previously discussed in Section 5.4.2, for the repeated commuting trip data, although the test vehicle follows the same route on different work days, the large traction power events happen at different times and locations along the route. The

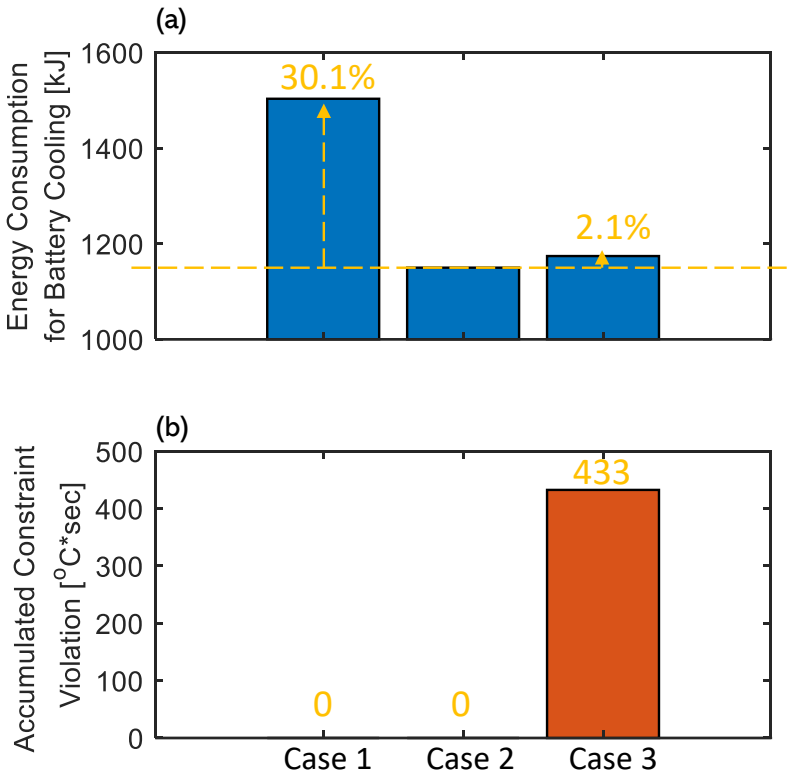

Figure 5.15: The energy consumption and battery temperature constraint violation results of Cases 1, 2, and 3: (a) energy consumption for battery cooling, and (b) accumulated T_{bat} constraint violation.

locations where the constraint violation occurs are marked in Fig. 5.16-(a). Note that we can compute the event probability and the maximum constraint violation at each location. The event probability means the probability of the battery temperature constraint violation when the vehicle passes through certain locations and only short prediction horizon is used in Case I. It can be observed that there is only a finite number of locations that have a non-zero probability of constraint violation based on historical trip data. This observation suggests a relationship between the high traction power event probability and the specific locations across the route. To leverage this relationship, a location-dependent constraint handling in MPC-based thermal management strategy is proposed and presented in Fig. 5.16-(b).

The location-dependent constraint handling strategy tightens the upper limit of

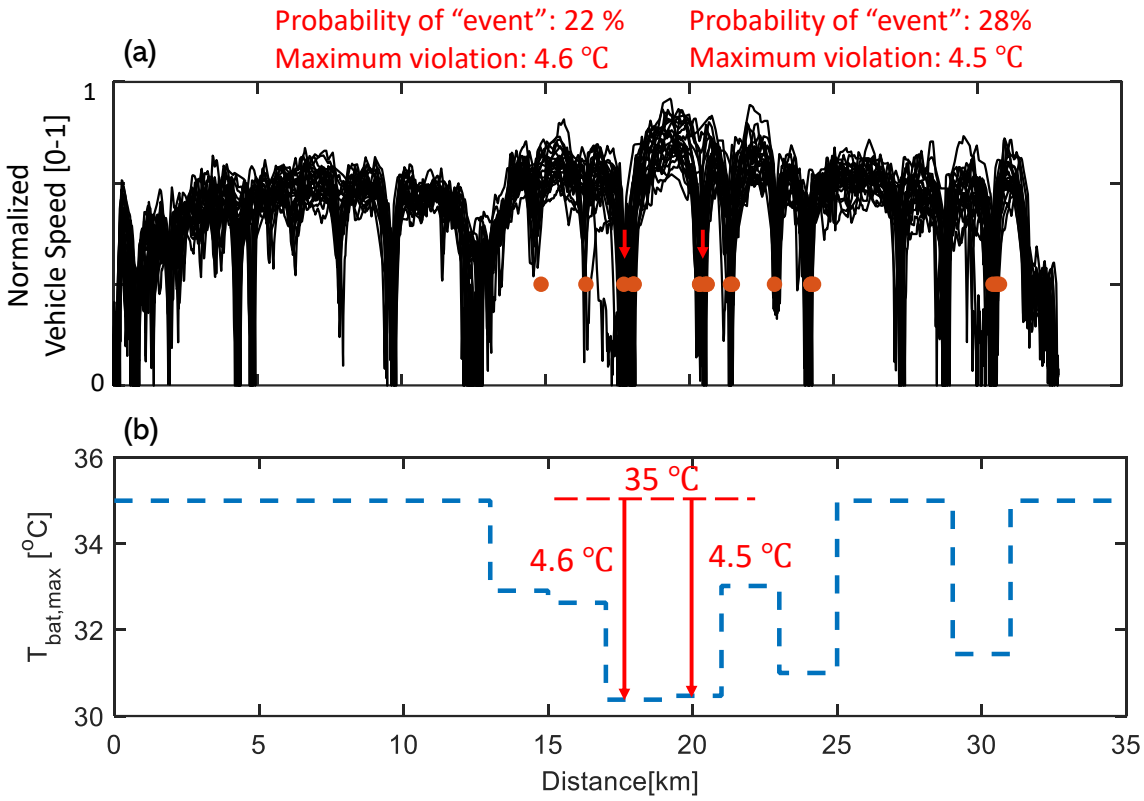

Figure 5.16: (a) the aggregated vehicle speed profiles in spatial domain (the red dots represent the locations of the events detected in the historical data) and (b) the concept of the location-dependent constraint handling strategy.

the battery temperature constraint based on the high traction power event probability and the maximum expected temperature constraint violation. If over a certain range, there is a probability of constraint violation based on the historical data, the upper limit, $T_{bat,max}$, is tightened based on the maximum violation of Case I. For example, two locations highlighted in Fig. 5.16 have a high traction power event probability of 22% and 28%, respectively, and their maximum T_{bat} violation are 4.6^oC and 4.5^oC, respectively. Therefore, the upper battery temperature limits of these two locations are tightened by 4.6^oC and 4.5^oC in the MPC formulation, once these two locations are detected within the controller prediction horizon. Whereas, for those locations where no constraint violation was observed based on historical data, no constraint

tightening will be performed, i.e., $T_{bat,max} = 35^oC$. Note that in this study, we consider the worst case with largest violation and the probability of violation has not been used for constraint tightening.

To demonstrate the benefits of the proposed location-dependent constraint handling strategy, a new Case 4 is defined as follows and compared against Cases 1-3:

- **Case 4**: the preview information is based on the average speed shown in Fig. 5.13 and is subject to uncertainties. The prediction horizon length is 200 *sec*; the location-dependent constraint is imposed on the upper limit of the battery temperature over the trip.

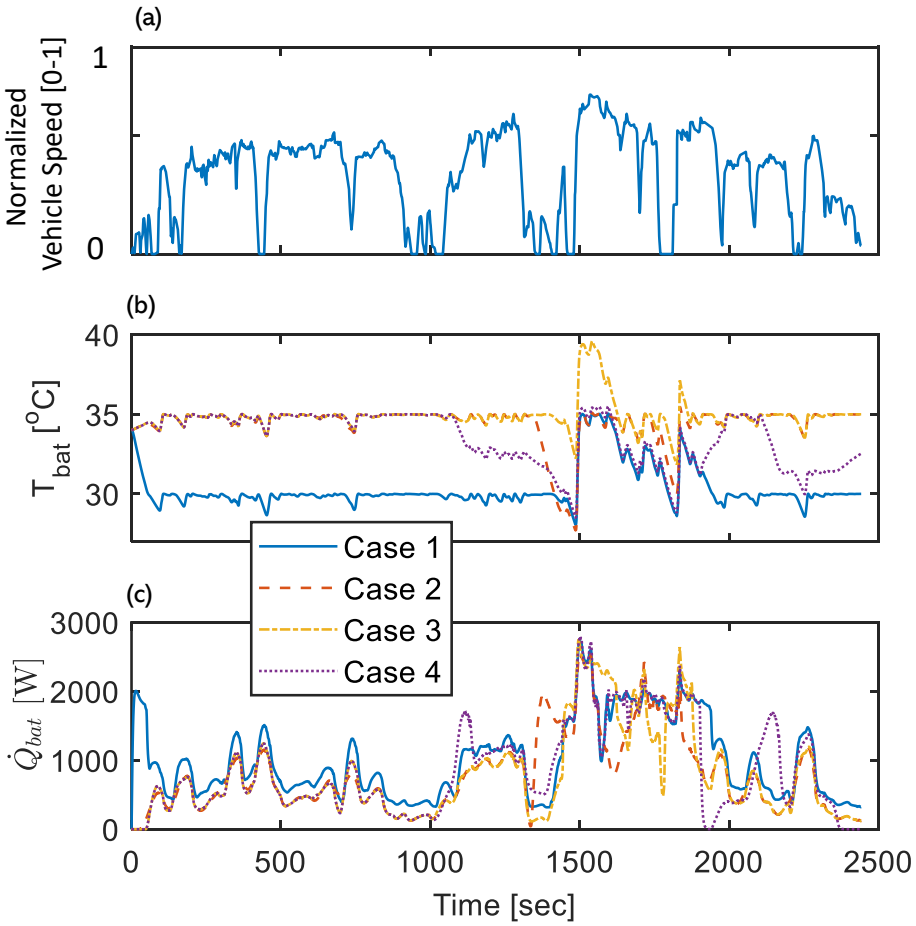

Figure 5.17: State trajectories of Cases 1-4: (a) vehicle speed and (b) battery temperature. (c) battery cooling power.

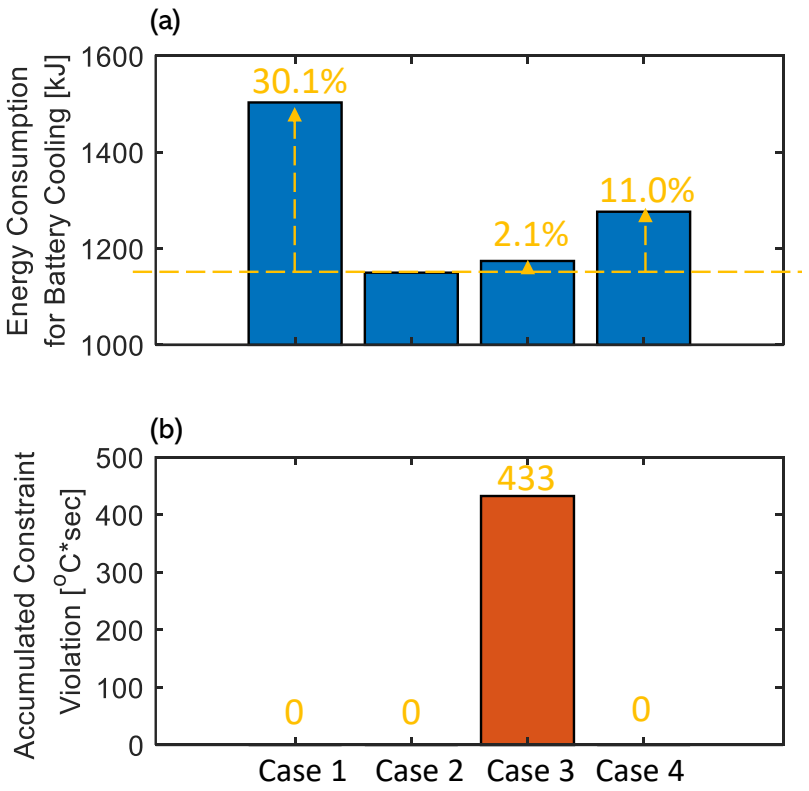

Figure 5.18: The results of Cases 1-4: (a) energy consumption for battery cooling, and (b) accumulated constraint violation.

The state trajectories with MPC are presented in Fig. 5.17, and the energy consumption and accumulated constraint violation are summarized in Fig. 5.18. It can be seen from Fig. 5.17 that with the uncertain vehicle speed over the long horizon, the battery temperature constraints can be enforced over the entire trip thanks to the proposed location-dependent battery temperature constraint handling strategy. Moreover, compared to Case 1, the proposed strategy in Case 4 achieves energy saving of 19.1%. Thus the proposed MPC-based thermal management strategy with the location-dependent constraint handling improves the energy efficiency while reducing the battery temperature constraint violation.

5.5 Summary

The thermal management system (TMS) in electric vehicles (EVs) consumes considerable energy for maintaining the battery and cabin temperature within a desired range. To increase the driving range of EVs and enhance the efficiency of the TMS, a model predictive control (MPC) based strategy was developed and comprehensively evaluated in this paper. The relatively slow dynamics of thermal systems call for a long prediction horizon over which the vehicle speed and vehicle traction power forecast may not be accurate. In this paper, we showed that accurately predicting certain key features in vehicle speed and vehicle traction power such as the timing and magnitude of large changes can have a significant impact on the MPC-based TMS performance. The MPC-based thermal management strategy was evaluated using real-world drive cycles and a location-dependent thermal constraint handling strategy was proposed to improve the robustness of the controller in presence of uncertainties.

CHAPTER VI

Enhanced Fast Charging Enabled by Battery Thermal Management and Model Predictive Control for Electric Vehicle

In Chapter V, the MPC-based power and thermal management strategy has been applied to EVs for improving energy efficiency and enforcing the constraints. This chapter explores the synergy between battery thermal management and battery charging for an EV. An MPC-based approach is proposed to minimize the energy used for battery thermal management during the drive and fast charging stages and the estimated charging time while enforcing constraints imposed on state-of-charge (SOC), power, and thermal conditions of the battery.

6.1 Problem Formulation

We consider a commercial EV operating under a hot ambient temperature and with a low initial SOC, requiring the battery to be charged at a nearby fast charging station. The objectives of the iPTM for the EV in this study are threefold. The first objective is to ensure the final SOC after charging is above a certain threshold. The second objective is to keep the total charging time within the desired range. Lastly, we aim to minimize the energy consumption for the battery thermal management

system while enforcing power and thermal constraints. In a real-world application, the requirements on the final SOC and charging time are typically determined by the type of trip and mission of the commercial vehicle after the charging event.

6.2 MPC Formulation of EV iPTM

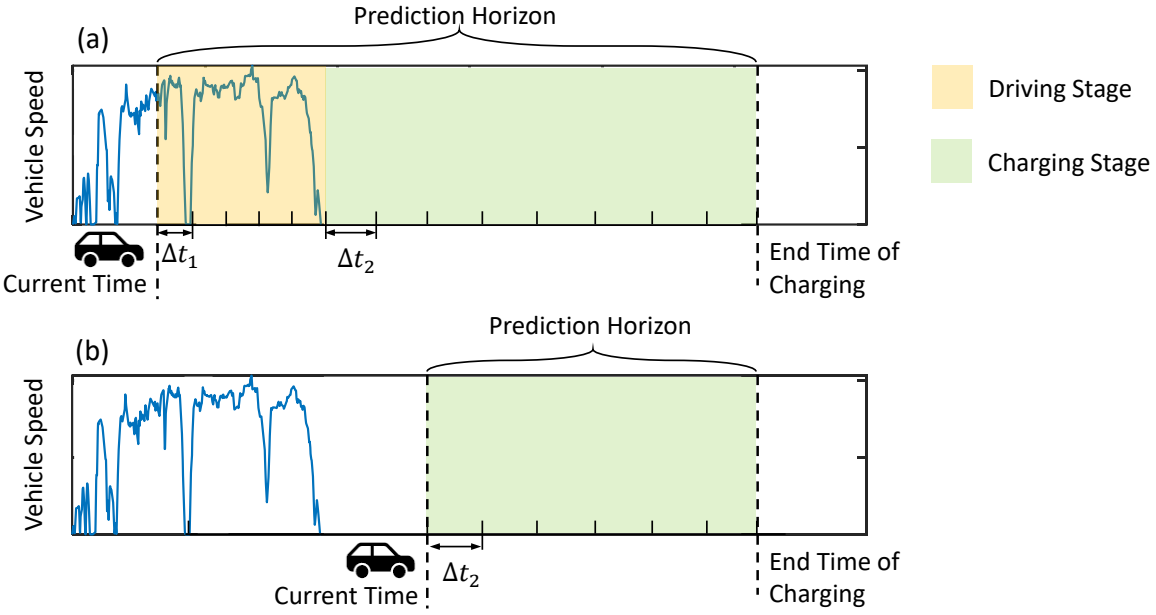

Figure 6.1: The notional illustration of the proposed MPC-based iPTM strategy implemented (a) before the charging starts, when the vehicle moves towards the charging station, and (b) after the charging starts, when the vehicle stays in the charging station.

To address the aforementioned objectives, an MPC-based iPTM is proposed in this chapter. As shown in Fig. 6.1, two different scenarios, before and after the start of the charging event, are considered. Before the start of the charging event, the vehicle moves towards the charging station, and the prediction horizon of the MPC extends from the current time until the projected end time of the charging event. This time horizon is divided into two stages of driving and charging. After the charging starts, the vehicle stays at the charging station, and the prediction horizon only has one stage from the current time to the end of the charging event. In both cases, the

discrete-time finite horizon optimization problem in MPC can be expressed as:

$$
\begin{aligned}
\min_{\substack{\dot{Q}_{cl}(i),\\ P_{chg}(i),\ \Delta t_2(i)}} \quad & \sum_{i=t}^{t+N_1-1} \left(\frac{\dot{Q}_{cl}(i)}{COP(i)}\Delta t_1\right)^2 \ + \\
& \sum_{i=t+N_1}^{t+N_1+N_2-1} \{\left(\frac{\dot{Q}_{cl}(i)}{COP(i)}\Delta t_2\right)^2 + \alpha(\Delta t_2(i))^2 + \beta\epsilon^2\}, \\
\text{s.t.} \quad & SOC(i+1) = SOC(i) + f_{soc}(i)\Delta t_j, \quad j \in \{1,2\} \\
& T_{bat}(i+1) = T_{bat}(i) + f_{bat}(i)\Delta t_j, \quad j \in \{1,2\} \\
& SOC_{min} \le SOC(i) \le SOC_{max}, \\
& T_{bat,min} \le T_{bat}(i) \le T_{bat,max} + \epsilon, \\
& -\dot{Q}_{cl,max} \le \dot{Q}_{cl}(i) \le 0, \\
& 0 \le P_{chg}(i) \le P_{chg,max}, \\
& 0 \le \Delta t_2(i) \le \Delta t_{2,max},
\end{aligned}
\tag{6.1}
$$

where f_{SOC} and f_{bat} designate the right hand sides of (2.5) and (2.7). Δt_1 and Δt_2 are the sampling time over the driving and charging stages, respectively, and N_1 and N_2 correspond to the numbers of sampling points over these two stages. Therefore, the prediction horizon length is $\Delta t_1 N_1 + \Delta t_2 N_2$ where $\Delta t_1 N_1$ is the remaining time for the vehicle to arrive at the charging station while $\Delta t_2 N_2$ is the total predicted time spent at the charging station. Note that $N_1 = 0$ once the driving is completed and charging started. The index $j \in \{1,2\}$ is determined as follows:

$$
j = \begin{cases} 1, & \textbf{if} \quad i \le t + N_1 - 1, \\ 2, & \textbf{if} \quad i \ge t + N_1. \end{cases}
\tag{6.2}
$$

It can be seen from (6.1) that the control/decision variables are $\dot{Q}_{cl}$, P_{chg}, and Δt_2, and the cost function consists of four terms. The first and second terms are the accumulated energy consumption of the battery cooling system over the driving and charging stages. The third term is the square of Δt_2, which penalizes the total charg-

ing time. The last term is used to relax the constraint on the battery temperature by introducing a slack variable (ϵ) treating the battery temperature limit as a soft constraint. It avoids infeasibility in solving the discrete-time optimization problem.

Different from the conventional receding or shrinking horizon MPC, the length of the charging time not pre-determined and depends on the computed solution of problem (6.1) with Δt_2 being an optimization variable. Therefore, a novel sampling strategy with varying sampling time and sampling points over different optimization horizons is proposed to accommodate the iPTM problem in this study, as summarized here. During the driving stage, the sampling time Δt_1 is fixed, and N_1 is calculated based on the remaining time before the vehicle arrives at the charging station. However, at the charging stage, the sampling time Δt_2 is one of the adjustable variables determined by the solution of the optimization problem (6.1), and it is no longer fixed. Instead, the number of samples, N_2, is fixed. Such a sampling strategy allows us to fix the dimension of the optimization problem (6.1) and solve it numerically. Then, by applying the first element of the computed control sequence to the plant and repeating the optimization with updated initial conditions, a feedback law is formed as in the conventional receding horizon MPC scheme.

6.3 Simulation Results and Discussion

In this section, we present the simulation results of the multi-objective MPC on a commercial EV. A sensitivity analysis is conducted to evaluate the performance of the controller. The ambient temperature is set to 35^oC and the initial battery SOC to 0.3 (30%). The vehicle goes through an urban route to arrive at the fast charging station, and the battery is required to be charged to $SOC = 0.6$. Moreover, the maximum battery cooling power and charging power of the station are 5 kW and 80 kW, respectively.

For this study, during both driving and charging stages, we design the MPC to

maintain the battery temperature within an operating range of $15 - 35\ ^oC$ [106, 107]. To prevent soft temperature constraint violation, we set the slack variable $\beta = 10^8$, which is large enough to avoid constraint violation over our example use cases.

6.3.1 Trade-off Between BTM Energy Use and Charging Time

We first assume that the vehicle speed profile over the urban route is known a priori, based on which the arrival time at the charging station can also be accurately predicted. This assumption will be relaxed in Section 6.3.3. To investigate the impact of the weight (α) on the charging time in (6.1), a sensitivity analysis is conducted, and the results are summarized in Fig. 6.2.

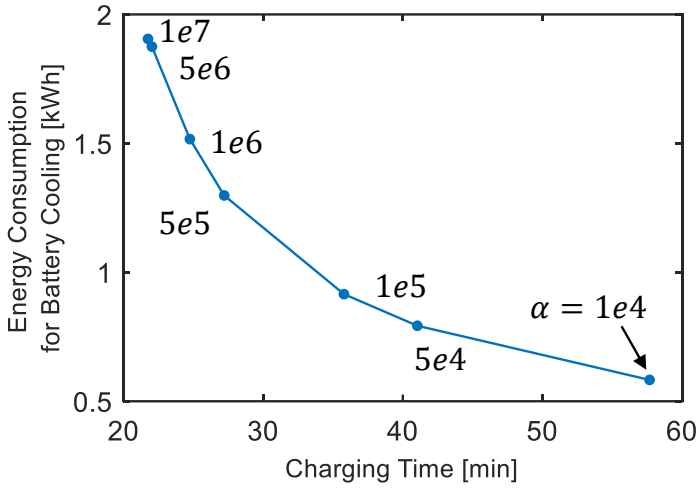

Figure 6.2: The energy consumption for battery cooling versus battery charging time as α varies.

A trade-off can be observed from Fig. 6.2 between the energy consumed for battery cooling and battery charging time. As α increases, the battery charging time decreases while the energy consumed for battery cooling increases. To illustrate the impact of different weight values, the state and input trajectories of two cases with different α are presented in Fig. 6.3. It can be seen that for both cases, thanks to the soft constraint settings and battery cooling system, the battery temperature is maintained

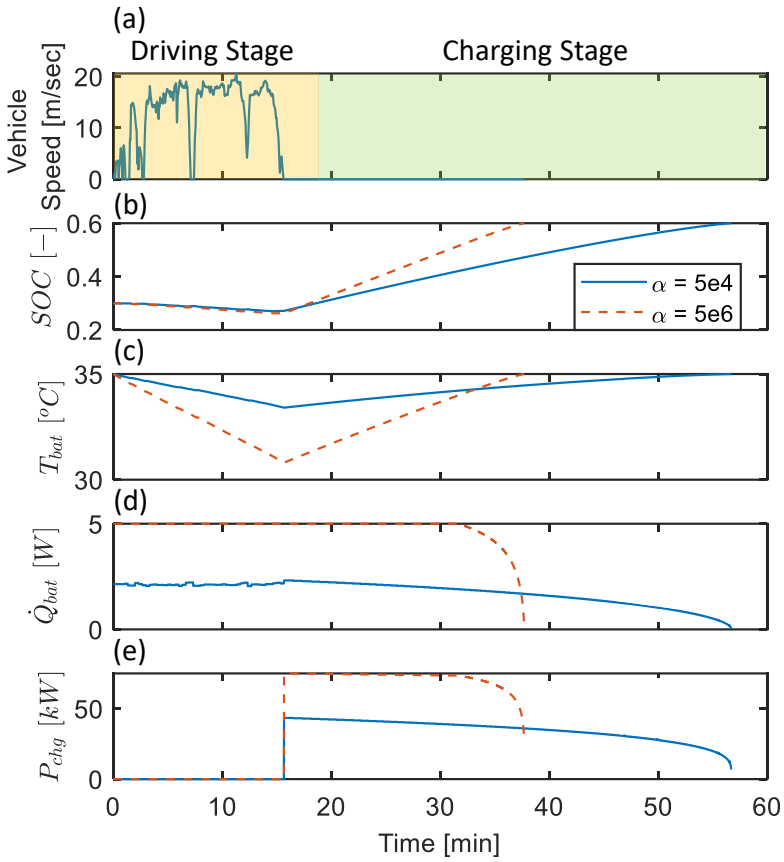

Figure 6.3: State and input trajectories with different α values: (a) vehicle speed, (b) SOC, (c) battery temperature, (d) battery cooling power, and (d) battery charging power.

within the desired range during the whole process. By comparing the two cases, it can be seen that, with a larger α, the controller tends to draw a larger battery charging power during the charging stage to reduce the charging time, as more focus is put on the penalty term for the charging time in the cost function. However, a larger battery charging power, on the other hand, requires a larger battery cooling power to avoid raising temperature over desired thresholds. Moreover, with accurate knowledge of the arrival time and charging event timing, battery pre-cooling of battery is effected to create some room for the rise of battery temperature, thereby enabling faster charging with larger charging power. The above observations explain the trade-off between energy consumed for battery cooling and total charging time, as well as the

pre-cooling feature associated with larger α.

6.3.2 Weight Adaptation Strategy

The results in Section 6.3.1 demonstrate that in order to balance the charging time and BTM energy consumption, α needs to be properly tuned to enforce the constraint on charging time while minimizing the energy consumption. There are several challenges of scheduling α in real-time. Note that α is determined by the arrival time at the charging station and by the required charging time. It needs to be adjusted during the trip to deal with uncertainties in vehicle speed preview, availability of charging, etc. In this section, an adaptive strategy to schedule α in real-time is proposed, which can be summarized as follows:

Algorithm VI.1: Weight Adaptation based on the Estimated Charging Time

An initial value of α is selected from the range shown in Fig. 6.2, at $t = 0$ *sec.*
for *each time step* **do**
    Solve optimization problem (6.1 using the current α_t;
    Estimated charging time ($t_{chg,est}$) is calculated as $\Delta t_2 N_2$;
    Update α so that $log(\alpha_{t+\Delta t_j}) = log(\alpha_t) + \lambda(t_{chg,est} - t_{chg,req})$.
end

Here, λ is the adaptation rate, and Δt_j is the sampling time defined in (6.1). It can be seen that the update law for α leverages the relationship presented in Fig. 6.2, and α is updated by comparing the estimated charging time ($t_{chg,est}$) with the required charging time ($t_{chg,req}$). Given the broad range of the α values shown in Fig. 6.2, to more effectively update α and adjust the optimal performance, a logarithmic update law is selected.

To show the effectiveness of the proposed adaptive strategy for updating α, the required charging time is set to be within 30 *min*, and different λ values are applied in Algorithm VI.1. The simulation results are presented in Fig. 6.4, and the actual charging times of three cases are summarized in Table. 6.1. It can be seen that

for these three cases, the initial guess for α is too small, which leads to an estimated battery charging time of almost 50 min. With the α updated by the adaptive law, the estimated charging time converges to the value near $t_{chg,req}$. Moreover, as λ increases, the convergence rate increases, and the steady-state error in the final charging time decreases. Based on these results, $\lambda = 0.1$ is adopted for this study, to better adhere to the charging time constraint.

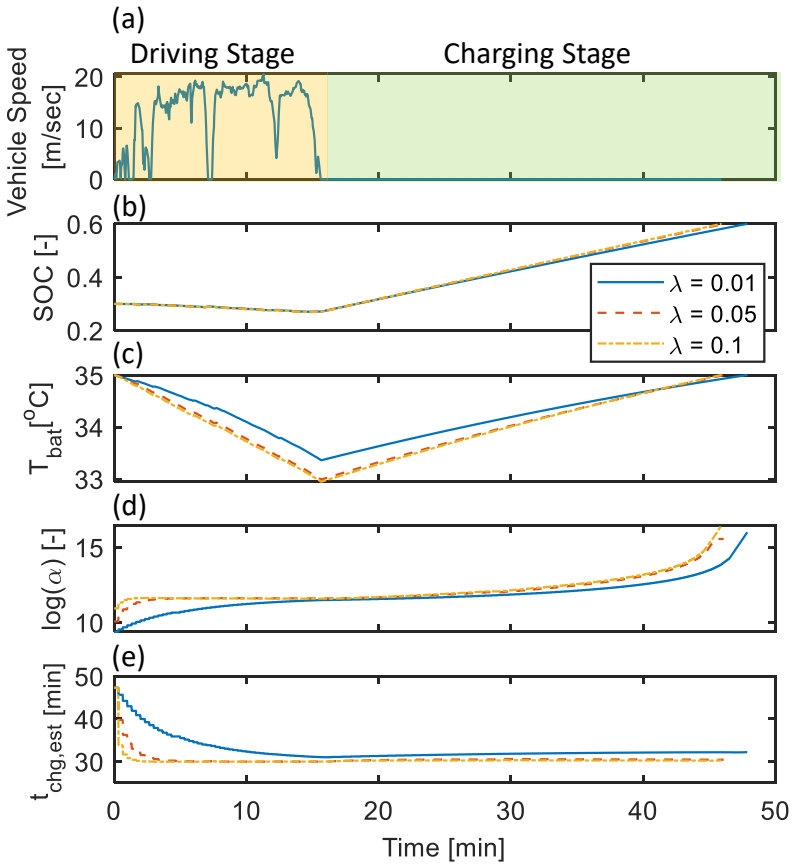

Figure 6.4: State and input trajectories with different adaptive rate λ: (a) vehicle speed, (b) SOC, (c) battery temperature, (d) weight on charging time, and (e) estimated charging time.

Table 6.1: The actual charging time with different adaptive rates.

λ	**0.01**	**0.05**	**0.1**
t_{chg} $[min]$	32.2	30.4	30.2

It can be seen in Figs. 6.3 and 6.4 that, MPC incorporates the knowledge of the

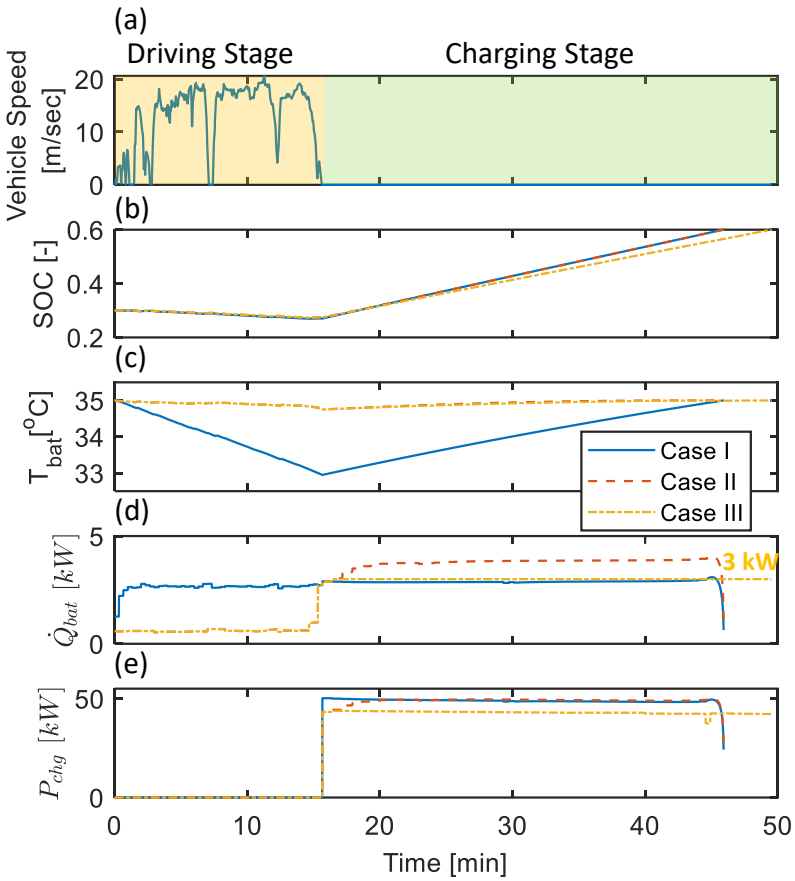

Figure 6.5: State and input trajectories with different α for Cases I, II, and III: (a) vehicle speed, (b) SOC, (c) battery temperature, (d) battery cooling power, and (d) battery charging power.

upcoming charging event to pre-cool the battery, allowing larger battery charging power to reduce the charging time. To quantify the benefits of leveraging the preview information and identify the conditions under which the pre-cooling is beneficial, the following three cases are considered for comparison:

- **Case I**: The charging event is predicted accurately over the prediction horizon,
- **Case II**: The charging event is not predicted until the vehicle arrives at the charging station, and the maximum cooling power is 5 kW,
- **Case III**: The charging event is not predicted until the vehicle arrives at the charging station, and the maximum cooling power is 3 kW.

For Case I, it is assumed that the preview information is known a priori, and the proposed MPC-based iPTM is applied at driving and charging stages. For Case II and Case III, before vehicle arrives at the station, as the charging event is not predicted over the prediction horizon, the cost function only has the first term in (6.1) to minimize the BTM energy consumption during the driving stage. After vehicle arrives at the station and starts charging, the same optimization problem in (6.1) is solved by MPC. The only difference between Case II and Case III is the maximum battery cooling power. Fig. 6.5 presents the state and input trajectories of these three cases, and the charging time and BTM energy consumption results are compared in Fig. 6.6.

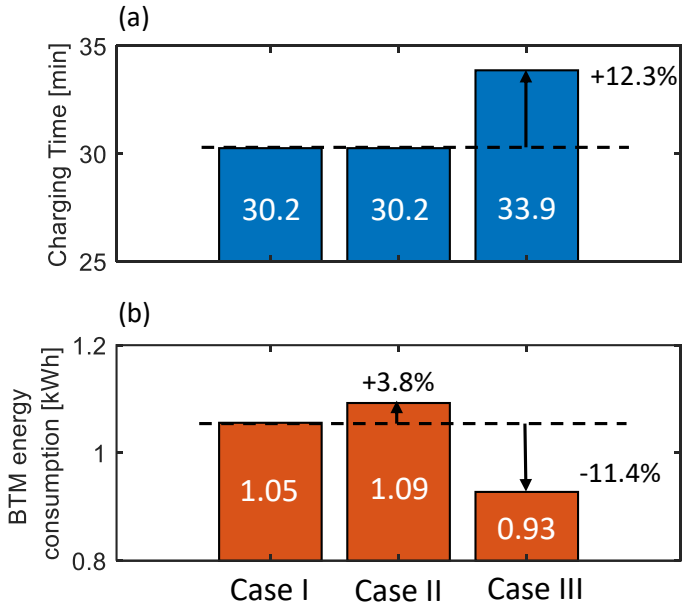

Figure 6.6: Simulations results of Cases I, II, and III: (a) charging time, (b) BTM energy consumption.

It can be seen in Fig. 6.5 that pre-cooling is only performed in Case I, while the battery temperature in Cases II and Case III follows the upper bound constraint prior to vehicle arriving at the charging station to minimize the cooling loads. While the initial battery temperatures at the beginning of the charging stage are different, Cases I and II have similar charging times. This is because the battery charging power in

these two cases is almost the same, as shown in Fig. 6.5-(e). Compared to Case I which has a lower initial battery temperature at the start of the charging stage, Case II needs to increase the battery cooling power to avoid constraint violation, when applying the same charging power. It can be seen from Fig. 6.5-(d) that the battery cooling power for Case I is always below 3 kW, while the cooling power for Case II is above 4 kW during the charging stage, leading to a slight increase in the BTM energy consumption, as shown in Fig. 6.6-(b).

As a result, when the maximum cooling power is reduced to 3 kW in Case III, the same charging power is unattainable without pre-cooling, and the charging time is increased by 12.3%. Note that because the upper bound constraint on cooling power in Case I is inactive, the optimal performance would remain the same when the maximum cooling power is reduced from 5 kW to 3 kW. This case study illustrates that pre-cooling can distribute the cooling load over time such that the cooling demand remains within the available capacity. This restriction is particularly notable when the same refrigerant system on an EV is applied for battery cooling and cabin climate control, simultaneously.

6.3.3 Robustness of the MPC-based iPTM Algorithm Against Selected Uncertainties

In Sections 6.3.1 and 6.3.2, the effectiveness of the proposed MPC-based iPTM framework was demonstrated. While the controller successfully enforces the power and thermal constraints during the battery charging process and keeps the charging time to the desired range, such favorable performance requires preview information, e.g., vehicle speed prediction, availability of charging, etc. The previous simulations assume that accurate preview information is available. This assumption is relaxed in this subsection and the robustness of the algorithm is studied.

We consider a scenario in which the vehicle needs to wait in a queue after arriving

at the station and before starting to charge. The total time that vehicle is allowed to spend in the charging station includes the queuing time and charging time, which is determined by the requirement of the mission after charging. While it is assumed that the queuing time can be estimated using connectivity information, this estimate is still subject to uncertainty. The proposed scenario is illustrated in Fig. 6.7-(a). As a case study, we assume that the total time is 40 min. It is also assumed that the estimated waiting time before the vehicle arrives at the station is 5 min, but the actual waiting time is 10 min. We also assume that the actual waiting time becomes available when the vehicle arrives at the charging station. Moreover, the target battery SOC is still 0.6.

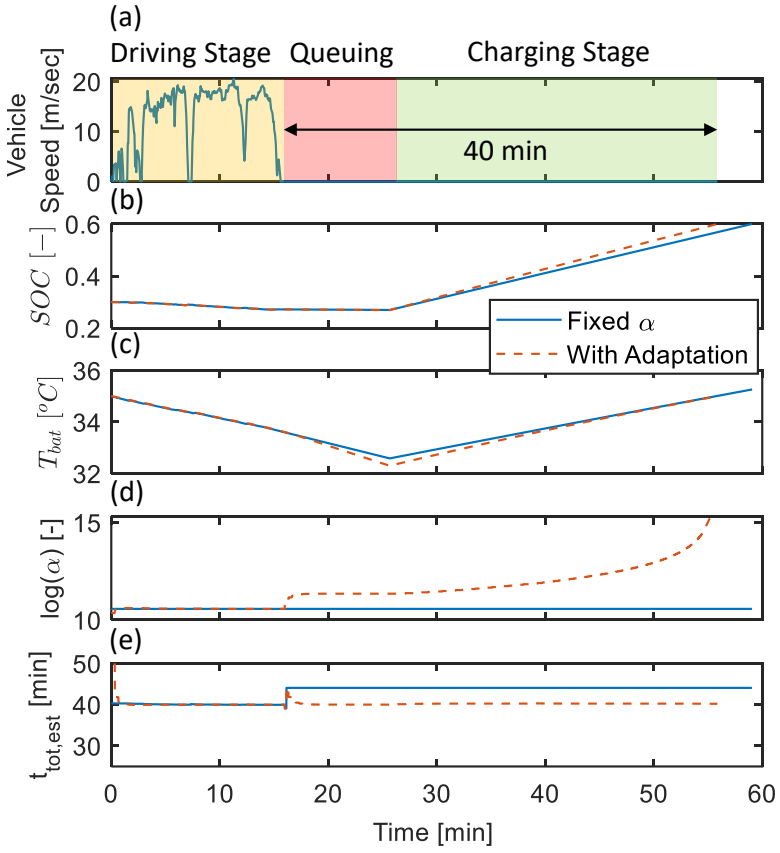

Figure 6.7: State and input trajectories with different adaptive rate: (a) vehicle speed, (b) SOC, (c) battery temperature, (d) weight on charging time, and (e) estimated total time staying at charging station.

The proposed MPC-based iPTM combined with the adaptive strategy for α weight adjustment is now applied for this scenario. Simulation results are presented in Fig. 6.7. Note that for comparison, a reference case with fixed α is also presented in Fig. 6.7. In this case, α is determined assuming that the waiting time is 5 min, and will not be updated during the whole process.

Before the vehicle arrives at the station, with the estimated waiting time of 5 min, the scheduled charging time for both cases is 35 min to ensure the total time vehicle remains at the station is 40 min. However, when the vehicle arrives at the station, knowing the actual waiting time, the responses of two cases diverge. With the adaptation strategy, the controller is capable of re-scheduling the charging time to 30 min, while with a fixed α, the total time that vehicle remains at the charging station exceeds 40 min due to the uncertainty of the waiting time.

It can be seen in Fig. 6.7-(d) that, with adaptation strategy, α immediately rises once the controller knows the actual waiting time is longer, which forces the controller to penalize more for the charging time. Note that the values of $t_{chg,req}$ in (**??**) are 35 and 30 min, respectively, before and after the vehicle's arrival. This case study illustrates that the adaptive weight scheduling strategy has the ability to handle the uncertainty of waiting time for the MPC-based iPTM framework.

6.4 Summary

In this chapter, a multi-objective model predictive control (MPC) strategy was proposed to minimize charging time and energy consumption for battery thermal management of a commercial electric vehicle (EV). The proposed method achieves a target battery state-of-charge (SOC) within the required time while enforcing the power, and thermal constraints of the battery system. The simulation results showed that the proposed MPC-based strategy, by leveraging the preview information, reduces the charging time via pre-cooling the battery before the start of the charging

event. Moreover, an adaptive strategy was proposed for adjusting the weight on the charging time in the MPC stage cost to manage the trade-off between charging time and battery thermal management (BTM) energy consumption. The case study with uncertainty in the waiting time at the charging station indicated that the adaptive strategy enhances the robustness of the algorithm while meeting the operational requirements.

CHAPTER VII

Conclusions and Future Work

7.1 Conclusions

In this dissertation, a novel multi-horizon model predictive control (MH-MPC) strategy was proposed for integrated systems with dynamics responding over different timescales. The MH-MPC exploits multi-range prediction and optimization over a short receding horizon and a long shrinking horizon with different accuracies and resolutions. The MH-MPC estimates the "cost-to-go" over the long shrinking horizon, beyond the conventional receding horizon. This approach is appealing for use in mission-based problems where the objective is accomplishing a mission with limited onboard energy and computational resources. For such systems, the MH-MPC relaxes the requirement for including a terminal penalty term in the receding horizon optimization cost function, allowing to incorporate an economic cost function over the entire prediction horizon. The economic cost function of MH-MPC and long shrinking horizon until the end of the mission enable the energy states to operate on or close to their admissible boundary to improve performance.

This proposed MH-MPC was demonstrated for integrated power and thermal management (iPTM) of hybrid electric vehicles (HEVs) operating in a connected traffic environment. In such an environment, short- and long-term predictions of the vehicle speed may be obtained using advanced V2V and V2I telematics and incorpo-

rated over the receding and shrinking horizons of the MH-MPC. Simulation results of applying MH-MPC to a power-split HEV demonstrated improved performance of the MH-MPC as compared to conventional MPC with a battery charge sustaining terminal penalty. Furthermore, in the absence of uncertainties in the vehicle speed forecast, MH-MPC performance was close to that of Dynamic Programming with a deviation of 1% for the case study considered. The MH-MPC performance also surpassed that of the long-horizon conventional MPC approach, while requiring less computational resources. The sensitivity and robustness of the iPTM strategy to uncertainties in long-term vehicle speed forecasts were also studied. The results suggested that, for city driving scenarios, the prediction of the vehicle stop events at signalized intersections and the average cruise speed between intersections are key information that can be leveraged for fuel-saving, even if the prediction is subject to moderate uncertainties.

Moreover, a novel data-driven multi-range vehicle speed prediction strategy was proposed for urban corridors with signalized intersections. The proposed strategy exploits historical traffic data collected from connected vehicles to provide a prediction of vehicle speed over short, medium, and long range. Over the short-range horizon, the vehicle speed prediction is obtained based on V2V/I communication, which is assumed of high accuracy. Over the long-range horizon, a Bayesian Network (BN) provides the vehicle speed prediction and estimates the most probable driving scenario until the end of the trip. The medium-range prediction (from the end of the short-range to the next intersection) exploits a Neural Network (NN) that is able to forecast the passing/stopping event at the next intersection with 90 % accuracy based on the validation data. Then the medium-range vehicle speed trajectory forecast is informed by exploiting the prediction of passing/stopping events and estimates of the queue length and stop/arrival time.

The effectiveness of the proposed vehicle speed prediction framework was demon-

strated by exploiting it for vehicle speed preview in an MH-MPC scheme used for HEV iPTM. The MH-MPC exploits a short receding horizon and longer shrinking horizon that extends to the end of the trip. The vehicle speed preview over the receding horizon is informed by V2V/V2I- based short-range vehicle speed prediction, while NN and BN-based approaches are used to inform the vehicle speed preview over the shrinking horizon. The simulation results show that, by incorporating the medium- and long-range speed preview, the MH-MPC achieves a fuel consumption within 1 % deviation from the offline Dynamic Programming solution for the case study considered. Furthermore, the sensitivity analysis revealed that by enhancing the accuracy of predicting the passing/stopping events, the performance of MH-MPC can be improved. Compared with constant vehicle speed preview, the proposed multi-range vehicle speed prediction reduces fuel consumption by around 1.28 % for the case study considered.

The other theme of the dissertation is to apply the MPC-based iPTM to electric vehicles (EVs) to increase the driving range of EVs and enhance energy efficiency. The relatively slow dynamics of thermal systems call for a long prediction horizon over which the vehicle speed and vehicle traction power forecast may not be accurate. In this paper, we showed that accurately predicting certain key features in vehicle speed and vehicle traction power such as the timing and magnitude of large changes can have a significant impact on the MPC-based iPTM performance. The MPC-based thermal management strategy was evaluated using real-world drive cycles and a location-dependent thermal constraint handling strategy was proposed to improve the robustness of the controller in presence of uncertainties.

Lastly, a multi-objective MPC was proposed in this research to minimize fast-charging time and energy consumption for battery thermal management of an EV. The proposed method achieves a target battery SOC within the required time while enforcing the power, and thermal constraints of the battery system. The simulation

results showed that the proposed MPC-based strategy, by leveraging the preview information, reduces the charging time via pre-cooling the battery before the start of the charging event. Moreover, an adaptive strategy was proposed for scheduling the gain of charging time in the MPC stage cost to leverage the trade-off between charging time and BTM energy consumption. The case study with uncertainty in the waiting time at the charging station demonstrated that the adaptive strategy ensures the robustness of the algorithm while meeting the operational requirements.

7.2 Ongoing and Future Research

Potential future research directions include:

1. Extending the applicability of the proposed MH-MPC strategy to other applications. Although in this study, the MH-MPC is particularly developed for the iPTM, such a framework can be generalized for other applications with multi-time scale systems, or there is a requirement of enforcing terminal conditions, such as spacecraft/vehicle trajectory planning[108, 109], microgrid power scheduling[110], chemical processes regulation[111], optimizing renewable energy storage[112] or generation[113].

2. Extending the vehicle speed prediction to load prediction. In this dissertation, we focus on vehicle speed prediction, which enables a preview of traction power and some other thermal loads. Such load prediction will be the input of the proposed MPC-based iPTM framework. However, there are other factors that could influence vehicle traction and thermal loads, such as road grade, door-opening events. Such factors need to be properly considered for a better prediction of vehicle loads.

3. Extending MH-MPC approach by using different fidelity models over different prediction horizons. Over the short-range horizon, a high fidelity model can be

used to more accurately predict the state dynamics, and over the long-range horizon, a less accurate model can be used to estimate the cost-to-go. The impact of the model mis-match caused by the reduce model fidelity needs to be investigated.

4. Studying the scalability of the BN-based and NN models for traffic networks with a large number of intersections. The branches of the BN and the number of the NN needed to be trained increase as the number of intersections increases. Therefore, for a long corridor, vehicle speed prediction will be more complicated and time-consuming.

5. Taking into account the variation in the driver behavior and aggressiveness level. In this dissertation, it is assumed that the vehicle models on the road are the same and the difference caused by the driver's behavior has not been considered. This can be studied by adapting the long-term speed predictions with respect to individual vehicles' speeds in real time and assessing the robustness of the speed prediction.

6. Identifying the important events based on the vehicle speed preview. In Chapter V, the events of large traction power associated with aggressive acceleration/deceleration are identified from the MPC simulation results with a short prediction horizon. Therefore, a more comprehensive analysis to mathematically identify the events directly using speed preview needs to be conducted in our future work for saving the efforts to run MPC simulation.

7. Incorporating more auxiliary power into the power and thermal management framework. In Chapter VI, the only auxiliary power considered in this study is the BTM power, and considerable power demands are also needed for other systems, e.g., climate control system. Particularly, when the refrigerant system needs to provide power for battery and cabin cooling simultaneously, the restric-

tion of battery cooling power will be more notable, and the battery charging time can be increased. The coupling of battery and cabin thermal management for charging optimization will be studied in our future work.

8. Develop statistical approach for iPTM application. In this dissertation, both preview information incorporated in the optimization and the optimization formulation are deterministic. However, the preview information are often of statistical nature. Therefore, developing statistical approach to leverage the preview information could be beneficial for iPTM application.

APPENDICES

APPENDIX A

The Correction Multiplier on the Actual Engine Fuel Consumption at Low Temperatures

The fuel consumption rate is a function of many variables, among which we consider engine speed, engine torque, and engine coolant temperature:

$$\dot{Q}_{fuel} = LHV \cdot \dot{m}_{fuel}(\omega_e, \tau_e, T_{cl}) \tag{A.1}$$

$$\dot{m}_{fuel}(\omega_e, \tau_e, T_{cl}) = \alpha(T_{cl}) \cdot f_{fuel}(\omega_e, \tau_e) \tag{A.2}$$

where $\dot{m}_{fuel}$ is the fuel consumption rate, $f_{fuel}(\omega_e, \tau_e)$ is the nominal fuel consumption rate calculated according to the BSFC map and $\alpha(T_{cl})$ is a correction multiplier introduced to reflect the impact of T_{cl}. The function of $\alpha(T_{cl})$, shown in Fig. A.1, can be found in Autonomie[1] software's thermal HEV model.

[1] Autonomie® is a MATLAB®/Simulink®-based system simulation tool for vehicle energy consumption and performance analysis developed by Argonne National Laboratory (ANL) [45]

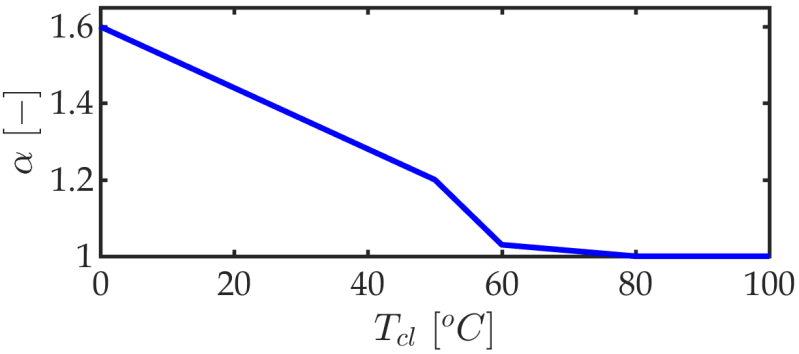

Figure A.1: The correction multiplier reflecting the impact of coolant temperature on the actual engine fuel consumption at low temperatures

APPENDIX B

Validation of Vehicle Traction Power Model

Figure B.1 shows the validation results of T_{cl} model (Eq. (2.10)) using experimental data collected from the test HEV over highway (Figure B.1-($a_{1,2}$)) and city (Figure B.1-($b_{1,2}$)) driving routes in Ann Arbor, MI.

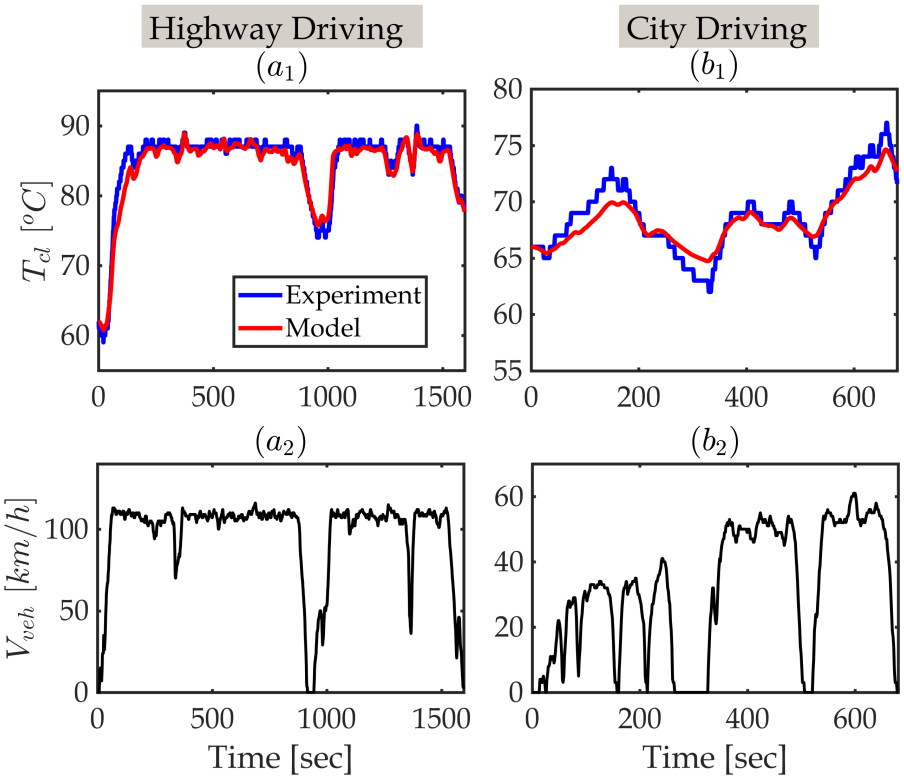

Figure B.1: The results of coolant temperature (T_{cl}) model validation.

BIBLIOGRAPHY

BIBLIOGRAPHY

[1] L. Paoli and T. Gül. Electric cars fend off supply challenges to more than double global sales. In *IEA: International Energy Agency*, 2022. Paris, French.

[2] K. Palmer, J. E. Tate, Z. Wadud, and J. Nellthorp. Total cost of ownership and market share for hybrid and electric vehicles in the uk, us and japan. *Applied energy*, 209:108–119, 2018.

[3] Georgios Fontaras, Panayotis Pistikopoulos, and Zissis Samaras. Experimental evaluation of hybrid vehicle fuel economy and pollutant emissions over real-world simulation driving cycles. *Atmospheric environment*, 42(18):4023–4035, 2008.

[4] A. R. Salisa, N. Zhang, and J. Zhu. A comparative analysis of fuel economy and emissions between a conventional hev and the uts phev. *IEEE Transactions on Vehicular Technology*, 60(1):44–54, 2010.

[5] W. J. Requia, M. Mohamed, C. D. Higgins, A. Arain, and M. Ferguson. How clean are electric vehicles? evidence-based review of the effects of electric mobility on air pollutants, greenhouse gas emissions and human health. *Atmospheric Environment*, 185:64–77, 2018.

[6] J. A. Sanguesa, V. Torres-Sanz, P. Garrido, F. J. Martinez, and J. M. Marquez-Barja. A review on electric vehicles: Technologies and challenges. *Smart Cities*, 4(1):372–404, 2021.

[7] M. Ehsani, Y. Gao, and J. M. Miller. Hybrid electric vehicles: Architecture and motor drives. *Proceedings of the IEEE*, 95(4):719–728, 2007.

[8] A. Sciarretta and L. Guzzella. Control of Hybrid Electric Vehicles. *IEEE Control Systems Magazine*, 27(2):60–70, 2007.

[9] L. Guzzella and A. Sciarretta. *Vehicle propulsion systems*, volume 1. Springer, 2007.

[10] J. Liu, H. Peng, and Z. Filipi. Modeling and Analysis of the Toyota Hybrid System. In *Int. Conference on Advanced Intelligent Mechatronics*, 2005. Monterey, CA, USA.

[11] A. Brahma, Y. Guezennec, and G. Rizzoni. Optimal Energy Management in Series Hybrid Electric Vehicles. In *ACC*, 2000. Chicago, IL, USA.

[12] C. Lin, H. Peng, J. Grizzle, and J. Kang. Power Management Strategy for a Parallel Hybrid Electric Truck. *IEEE Transactions on Control Systems Technology*, 11(6):839–849, 2003.

[13] N. Kim, S. Cha, and H. Peng. Optimal Control of Hybrid Electric Vehicles based on Pontryagin's Minimum Principle. *IEEE Transactions on Control Systems Technology*, 19(5):1279–1287, 2010.

[14] L. Serrao, S. Onori, and G. Rizzoni. ECMS as a Realization of Pontryagin's Minimum Pprinciple for HEV Control. In *2009*, 2009. St. Louis, MO, USA.

[15] H. Borhan, C. Zhang, A. Vahidi, A. Phillips, M. Kuang, and Di C. Nonlinear Model Predictive Control for Power-Split Hybrid Electric Vehicles. In *49th CDC*, 2010. Atlanta, GA, USA.

[16] S. Di Cairano, D. Bernardini, A. Bemporad, and I. Kolmanovsky. Stochastic MPC With Learning for Driver-predictive Vehicle Control and its Application to HEV Energy Management. *IEEE Transactions on Control Systems Technology*, 22(3):1018–1031, 2013.

[17] M. Bichi, G. Ripaccioli, S. Di Cairano, D. Bernardini, A. Bemporad, and I. Kolmanovsky. Stochastic Model Predictive Control with Driver Behavior Learning for Improved Powertrain Control. In *49th CDC*, 2010. Atlanta, GA, USA.

[18] H. Borhan, A. Vahidi, A. Phillips, M. Kuang, I. Kolmanovsky, and S. Di Cairano. MPC-based Energy Management of a Power-Split Hybrid Electric Vehicle. *IEEE Transactions on Control Systems Technology*, 20(3):593–603, 2011.

[19] A. Vahidi and A. Sciarretta. Energy Saving Potentials of Connected and Automated Vehicles. *Transportation Research Part C: Emerging Technologies*, 95:822–843, 2018.

[20] C. Wei, T. Hofman, E. Ilhan Caarls, and R. van Iperen. A Review of the Integrated Design and Control of Electrified Vehicles. *Energies*, 13(20):5454, 2020.

[21] J. Zhao, Chang C.F., R. Rajkumar, and J. Gonder. Corroborative Evaluation of the Real-World Energy Saving Potentials of InfoRich Eco-Autonomous Driving (iREAD) System. 2020. SAE Technical Paper 2020-01-0588.

[22] P. Zhang, F. Yan, and C. Du. A Comprehensive Analysis of Energy Management Strategies for Hybrid Electric Vehicles based on Bibliometrics. *Renewable and Sustainable Energy Reviews*, 48:88–104, 2015.

[23] J. Rios-Torres and A.A. Malikopoulos. A Survey on the Coordination of Connected and Automated Vehicles at Intersections and Merging at Highway On-ramps. *IEEE Transactions on Intelligent Transportation Systems*, 18(5):1066–1077, 2016.

[24] J. Guanetti, Y. Kim, and F. Borrelli. Control of Connected and Automated Vehicles: State of the Art and Future Challenges. *Annual Reviews in Control*, 45:18–40, 2018.

[25] S. Li, Y. Zheng, K. Li, Y. Wu, J.K. Hedrick, F. Gao, and H. Zhang. Dynamical Modeling and Distributed Control of Connected and Automated vehicles: Challenges and Opportunities. *IEEE Intelligent Transportation Systems Magazine*, 9(3):46–58, 2017.

[26] H. Wang, M. R. Amini, Q. Hu, I. Kolmanovsky, and J. Sun. Eco-cooling control strategy for automotive air-conditioning system: Design and experimental validation. *IEEE Transactions on Control Systems Technology*, 29(6):2339–2350, 2020.

[27] M.R. Amini, Q. Hu, H. Wang, Y. Feng, I. Kolmanovsky, and J. Sun. Experimental Validation of Eco-Driving and Eco-Heating Strategies for Connected and Automated HEVs. 2021. SAE Technical Paper 2021-01-0435.

[28] C. Sun, S. Moura, X. Hu, J.K. Hedrick, and F.n Sun. Dynamic Traffic Feedback Data Enabled Energy Management in Plug-in Hybrid Electric Vehicles. *IEEE Transactions on Control Systems Technology*, 23(3):1075–1086, 2014.

[29] X. Wu and H. X. Liu. A Shockwave Profile Model for Traffic Flow on Congested Urban Arterials. *Transportation Research Part B: Methodological*, 45(10):1768–1786, 2011.

[30] M.R. Amini, Y. Feng, Z. Yang, I. Kolmanovsky, and J. Sun. Long-Term Vehicle Speed Prediction via Historical Traffic Data Analysis for Improved Energy Efficiency of Connected Electric Vehicles. *Transportation Research Record*, 2674(11):17–29, 2020.

[31] Z. Yang, Y. Feng, X. Gong, D. Zhao, and J. Sun. Eco-Trajectory Planning with Consideration of Queue along Congested Corridor for Hybrid Electric Vehicles. *Transportation Research Record*, 2019. in press, doi:10.1177/0361198119845363.

[32] Zang, D. and Ling, J. and Wei, Z. and Tang, K. and Cheng, J. Long-term Traffic Speed Prediction based on Multiscale Spatio-temporal Feature Learning Network. *IEEE Transactions on Intelligent Transportation Systems*, 20(10):3700–3709, 2018.

[33] J. Herrera, D. Work, R. Herring, X. Ban, Q. Jacobson, and A. Bayen. Evaluation of Traffic Data Obtained via GPS-Enabled Mobile Phones: The Mobile Century field experiment. *Transportation Research Part C: Emerging Technologies*, 18(4):568–583, 2010.

[34] Kim, Y. and Wang, P. and Mihaylova, L. Structural Recurrent Neural Network for Traffic Speed Prediction. In *ICASSP 2019-2019 IEEE International Conference on Acoustics, Speech and Signal Processing (ICASSP)*, pages 5207–5211. IEEE, 2019. Brighton, United Kingdom.

[35] B. Jiang and Y. Fei. Vehicle Speed Prediction by Two-level Data Driven Models in Vehicular Networks. *IEEE Transactions on Intelligent Transportation Systems*, 18(7):1793–1801, 2016.

[36] J. Park, Y. L. Murphey, R. McGee, J. Kristinsson, M. L. Kuang, and A. M. Phillips. Intelligent Trip Modeling for the Prediction of an Origin–Destination Traveling Speed Profile. *IEEE Transactions on Intelligent Transportation Systems*, 15(3):1039–1053, 2014.

[37] Niu, K. and Zhang, H. and Zhou, T. and Cheng, C. and Wang, C. A Novel Spatio-temporal Model for City-scale Traffic Speed Prediction. *IEEE Access*, 7:30050–30057, 2019.

[38] X. Ma, Z. Tao, Y. Wang, H. Yu, and Y. Wang. Long Short-term Memory Neural Network for Traffic Speed Prediction using Remote Microwave Sensor Data. *Transportation Research Part C: Emerging Technologies*, 54:187–197, 2015.

[39] Huang, Y. and Xiao, Z. and Wang, D. and Jiang, H. and Wu, D. Exploring Individual Travel Patterns across Private Car Trajectory Data. *IEEE Transactions on Intelligent Transportation Systems*, 21(12):5036–5050, 2019.

[40] C. Atkinson. Energy and the New Mobility – How Disruptive (to Energy) will AVs be? In *ARPA-E Energy Innovation Summit*, 2019. Denver, CO, USA.

[41] S. Lin, Y. Zhang, C. Hsu, M. Skach, M. Haque, L. Tang, and J. Mars. The Architectural Implications of Autonomous Driving: Constraints and Acceleration. In *Proceedings of the Twenty-Third International Conference on Architectural Support for Programming Languages and Operating Systems*, 2018. Williamsburg, VA, USA.

[42] A. Alleyne. Power Density as the Key Enabler for Electrified Mobility. *Polytechnica*, 1(1–2):10–18, 2018.

[43] X. Gong, H. Wang, M. Amini, I. Kolmanovsky, and J. Sun. Integrated Optimization of Power Split, Engine Thermal Management, and Cabin Heating for Hybrid Electric Vehicles. In *3rd CCTA*, 2019. Hong Kong, China.

[44] M.R. Amini, Y. Yiheng, H. Wang, I. Kolmanovsky, and J. Sun. Thermal Responses of Connected HEVs Engine and Aftertreatment Systems to Eco-Driving. In *3rd CCTA*, 2019. Hong Kong, China.

[45] N. Kim, A. Rousseau, D. Lee, and H. Lohse-Busch. Thermal Model Development and Validation for 2010 Toyota Prius. 2014. SAE Technical Paper 2014-01-1784.

[46] H. Lohse-Busch, M. Duoba, E. Rask, K. Stutenberg, V. Gowri, L. Slezak, and D. Anderson. Ambient Temperature (20 F, 72 F and 95 F) impact on Fuel

and Energy Consumption for Several Conventional Vehicles, Hybrid and Plug-in Hybrid Electric Vehicles and Battery Electric Vehicle. 2013. SAE Technical Paper 2013-01-1462.

[47] N. Kim and A. Rousseau. Thermal Impact on the Control and the Efficiency of the 2010 Toyota Prius Hybrid Electric Vehicle. *Proceedings of the Institution of Mechanical Engineers, Part D: Journal of Automobile Engineering*, 230(1):82–92, 2016.

[48] N. Kheir, M. Salman, and N. Schouten. Emissions and Fuel Economy Trade-off for Hybrid Vehicles using Fuzzy Logic. *Mathematics and Computers in Simulation*, 66(2-3):155–172, 2004.

[49] C. Fiori, K. Ahn, and H. A. Rakha. Power-based electric vehicle energy consumption model: Model development and validation. *Applied Energy*, 168:257–268, 2016.

[50] E. E. Michaelides. Thermodynamics and energy usage of electric vehicles. *Energy Conversion and Management*, 203:112246, 2020.

[51] S. Chowdhury, L. Leitzel, M. Zima, M. Santacesaria, G. Titov, J. Lustbader, J. Rugh, J. Winkler, A. Khawaja, and M. Govindarajalu. Total thermal management of battery electric vehicles. *SAE Technical Paper Series*, 2018. MAHLE, Lockport, NY.

[52] L. Horrein, A. Bouscayrol, W. Lhomme, and C. Depature. Impact of heating system on the range of an electric vehicle. *IEEE transactions on Vehicular Technology*, 66(6):4668–4677, 2016.

[53] M. A. Jeffers, L. Chaney, and J. P. Rugh. Climate control load reduction strategies for electric drive vehicles in warm weather. Technical report, National Renewable Energy Lab.(NREL), Golden, CO, 2015.

[54] C. Wei, T. Hofman, E. Caarls, and R. van Iperen. Optimal control of an integrated energy and thermal management system for electrified powertrains. In *ACC*, 2019. Philadelphia, PA, USA.

[55] N. Doshi, D. Hanover, S. Hemmati, C. Morgan, and M. Shahbakhti. Modeling of thermal dynamics of a connected hybrid electric vehicle for integrated hvac and powertrain optimal operation. In *DSCC*, 2019. Park City, UT, USA.

[56] M. Shams-Zahraei, A. Kouzani, S. Kutter, and B. Bäker. Integrated Thermal and Energy Management of Plug-in Hybrid Electric Vehicles. *Journal of Power Sources*, 216:237–248, 2012.

[57] D. Maamria, A. Sciarretta, F. Chaplais, and N. Petit. Online Energy Management System (EMS) Including Engine and Catalyst Temperatures for a Parallel HEV. In *20th IFAC World Congress*, 2017. Toulouse, France.

[58] J. Zhao and J. Wang. Integrated Model Predictive Control of Hybrid Electric Vehicles Coupled with Aftertreatment Systems. *IEEE Transactions on Vehicular Technology*, 65(3):1199–1211, 2015.

[59] B. L. Chen, X. F. Li, S. Evangelou, and R. Lot. Joint propulsion and cooling energy management of hybrid electric vehicles by optimal control. *IEEE Transactions on Vehicular Technology*, 2020.

[60] J. Lescot, A. Sciarretta, Y. Chamaillard, and A. Charlet. On the integration of optimal energy management and thermal management of hybrid electric vehicles. In *IEEE Vehicle Power and Propulsion Conference*, 2010. Lille, France.

[61] A. Rashid, T. Hofman, and B. Rosca. Enhanced battery thermal management systems with optimal charge control for electric vehicles. In *Annual American Control Conference (ACC)*, pages 1849–1854, 2018.

[62] A. Hamednia, N. Murgovski, J. Fredriksson, J. Forsman, M. Pourabdollah, and V. Larsson. Optimal thermal management, charging, and eco-driving of battery electric vehicles. *arXiv preprint arXiv:2205.01560*, 2022.

[63] Y. Dahmane, R. Chenouard, M. Ghanes, and M. Alvarado-Ruiz. Optimized time step for electric vehicle charging optimization considering cost and temperature. *Sustainable Energy, Grids and Networks*, 26:100468, 2021.

[64] S. Park and C. Ahn. Model predictive control with stochastically approximated cost-to-go for battery cooling system of electric vehicles. *IEEE Transactions on Vehicular Technology*, 70(5):4312–4323, 2021.

[65] S. Park and C. Ahn. Computationally efficient stochastic model predictive controller for battery thermal management of electric vehicle. *IEEE Transactions on Vehicular Technology*, 69(8):8407–8419, 2020.

[66] M. R. Amini, J. Sun, and I. Kolmanovsky. Two-layer model predictive battery thermal and energy management optimization for connected and automated electric vehicles. In *IEEE Conference on Decision and Control (CDC)*, pages 6976–6981, 2018.

[67] M.R. Amini, I. Kolmanovsky, and J. Sun. Hierarchical MPC for Robust Eco-Cooling of Connected and Automated Vehicles and Its Application to Electric Vehicle Battery Thermal Management. *IEEE Transactions on Control Systems Technology*, 29(1):316–328, 2020.

[68] H. Wang, I. Kolmanovsky, M. Amini, and J. Sun. Model Predictive Climate Control of Connected and Automated Vehicles for Improved Energy Efficiency. In *ACC*, 2018. Milwaukee, WI, USA.

[69] H. Wang, Y. Meng, Q. Zhang, M. R. Amini, I. Kolmanovsky, J. Sun, and Jennings M. MPC-Based Precision Cooling Strategy (PCS) for Efficient Thermal

Management of Automotive Air Conditioning System. In *3rd CCTA*, 2019. Hong Kong, China.

[70] P. Kokotović, H.K. Khalil, and J. O'reilly. *Singular Perturbation Methods in Control: Analysis and Design*. SIAM, 1999.

[71] X. Chen, M. Heidarinejad, J. Liu, D.M. de la Peña, and P.D. Christofides. Model Predictive Control of Nonlinear Singularly Perturbed Systems: Application to a Large-scale Process Network. *Journal of Process Control*, 21(9):1296–1305, 2011.

[72] X. Chen, M. Heidarinejad, J. Liu, and P.D. Christofides. Composite Fast-slow MPC Design for Nonlinear Singularly Perturbed Systems. *AIChE Journal*, 58(6):1802–1811, 2012.

[73] M. Ellis, M. Heidarinejad, and P.D. Christofides. Economic Model Predictive Control of Nonlinear Singularly Perturbed Systems. *Journal of Process Control*, 23(5):743–754, 2013.

[74] M. Baldea, P. Daoutidis, and Z.K. Nagy. Nonlinear Model Predictive Control of Integrated Process Systems. *IFAC Proceedings Volumes*, 43(14):1040–1045, 2010.

[75] M. R. Amini, H. Wang, X. Gong, D. Liao-McPherson, I. Kolmanovsky, and J. Sun. Cabin and battery thermal management of connected and automated hevs for improved energy efficiency using hierarchical model predictive control. *IEEE Transactions on Control Systems Technology*, 28(5):1711–1726, 2019.

[76] J. Koeln, H. Pangborn, M. Williams, M. Kawamura, and A. Alleyne. Hierarchical Control of Aircraft Electro-Thermal Systems. *IEEE Transactions on Control Systems Technology*, 28(4):1218 – 1232, 2020.

[77] M. Brdys, M. Grochowski, T. Gminski, K. Konarczak, and M. Drewa. Hierarchical Predictive Control of Integrated Wastewater Treatment Systems. *Control Engineering Practice*, 16(6):751–767, 2008.

[78] E. Van Henten and J. Bontsema. Time-scale Decomposition of an Optimal Control Problem in Greenhouse Climate Management. *Control Engineering Practice*, 17(1):88–96, 2009.

[79] M. Farina, X. Zhang, and R. Scattolini. A Hierarchical Multi-Rate MPC Scheme for Interconnected Systems. *Automatica*, 90:38–46, 2018.

[80] M. Debert, G. Yhamaillard, and G.A. Ketfi-herifellicaud. Predictive Energy Management for Hybrid Electric Vehicles-Prediction Horizon and Battery Capacity Sensitivity. *IFAC Proceedings Volumes*, 43(7):270–275, 2010.

[81] Q. Hu, M.R. Amini, H. Wang, I. Kolmanovsky, and J. Sun. Integrated Power and Thermal Management of Connected HEVs via Multi-Horizon MPC,. In *ACC*, 2020. Denver, CO, USA.

[82] M. A. Fayazbakhsh and M. Bahrami. Comprehensive modeling of vehicle air conditioning loads using heat balance method. *SAE technical paper*, 2013:1507, 2013.

[83] X. Zhang. *Design of Power Split Hybrid Powertrains with Multiple Planetary Gears and Clutches.* PhD thesis, 2015.

[84] M.R. Amini, X. Gong, H. Wang, Y. Feng, I. Kolmanovsky, and J. Sun. Sequential Optimization of Speed, Thermal Load, and Power Split in Connected HEVs. In *ACC*, 2019. Philadelphia, PA, USA.

[85] M. Lee, H. Lee, and H. Won. Characteristic evaluation on the cooling performance of an electrical air conditioning system using r744 for a fuel cell electric vehicle. *Energies*, 5(5):1371–1383, 2012.

[86] Effects of Coolant Temperature on the Performance and Emissions of a Diesel Engine.

[87] G. Khoury and D. Clodic. Method of Test and Measurements of Fuel Consumption due to Air Conditioning Operation on the New Prius II Hybrid Vehicle. *SAE transactions*, 114(6):2563–2571, 2005.

[88] H. Wang, Y. Huang, A. Khajepour, and Q. Song. Model Predictive Control-based Energy Management Strategy for a Series Hybrid Electric Tracked Vehicle. *Applied Energy*, 182:105–114, 2016.

[89] M. Risbeck and J. Rawlings. MPCTools: Nonlinear Model Predictive Control Tools for CasADi. 2016. [online] Available: https://bitbucket.org/rawlings-group/octave-mpctools.

[90] J. Andersson, J. Gillis, G. Horn, J. Rawlings, and M. Diehl. CasADi: a Software Framework for Nonlinear Optimization and Optimal Control. *Mathematical Programming Computation*, 11(1):1–36, 2019.

[91] M. Morari and J.H. Lee. Model Predictive Control: Past, Present and Future. *Computers & Chemical Engineering*, 23(4-5):667–682, 1999.

[92] D. Moser, H. Waschl, R. Schmied, H. Efendic, and Luigi Del Re. Short Term Prediction of a Vehicle's Velocity Trajectory Using ITS. *SAE International Journal of Passenger Cars: Electronic and Electrical Systems*, 8(2015-01-0295):364–370, 2015.

[93] T. Molnár, X. A Ji, S. Oh, D. Takács, M. Hopka, D. Upadhyay, M. Van Nieuwstadt, and G. Orosz. On-board traffic prediction for connected vehicles: Implementation and experiments on highways. In *2022 American Control Conference (ACC)*, pages 1036–1041. IEEE, 2022.

[94] L. Jiang, T. G. Molnár, and G. Orosz. On the deployment of v2x roadside units for traffic prediction. *Transportation Research Part C: Emerging Technologies*, 129:103238, 2021.

[95] PTV Group. PTV Vissim 9.0 User Manual. *PTV AG, Karlsruhe, Germany*, 2016.

[96] Z. Yang, Y. Feng, X. Gong, D. Zhao, and J. Sun. Eco-trajectory Planning with Consideration of Queue Along Congested Corridor for Hybrid Electric Vehicles. *Transportation Research Record*, 2673(9):277–286, 2019.

[97] T. Zeng, C. Zhang, D. Hao, D. Cao, J. Chen, J. Chen, and J. Li. Data-driven Approach for Short-term Power Demand Prediction of Fuel Cell Hybrid Vehicles. *Energy*, 208:118319, 2020.

[98] X. Tang, T. Jia, X. Hu, Y. Huang, Z. Deng, and H. Pu. Naturalistic Data-driven Predictive Energy Management for plug-in Hybrid Electric Vehicles. *IEEE Transactions on Transportation Electrification*, 7(2):497–508, 2020.

[99] F. Zhang, J. Xi, and R. Langari. Real-time Energy Management Strategy based on Velocity Forecasts using V2V and V2I Communications. *IEEE Transactions on Intelligent Transportation Systems*, 18(2):416–430, 2016.

[100] S. Sun, C. Zhang, and G. Yu. A Bayesian Network Approach to Traffic Flow Forecasting. *IEEE Transactions on Intelligent Transportation Systems*, 7(1):124–132, 2006.

[101] M.I. Jordan. *Learning in Graphical Models*. Springer, Dordrecht, 1998.

[102] R. Zidek, I. Kolmanovsky, and A. Bemporad. Model Predictive Control for Drift Counteraction of Stochastic Constrained Linear Systems. *Automatica*, 123:109304, 2021.

[103] P. Wang, H. Deng, J. Zhang, L. Wang, M. Zhang, and Y. Li. Model Predictive Control for Connected Vehicle Platoon under Switching Communication Topology. *IEEE Transactions on Intelligent Transportation Systems*, 2021. doi: 10.1109/TITS.2021.3073012.

[104] Lodaya, D. and Zeman, J. and Okarmus, M. and Mohon, S. and Keller, P. and Shutty, J. and Kondipati, N. Optimization of fuel economy using optimal controls on regulatory and real-world driving cycles. *SAE International Journal of Advances and Current Practices in Mobility*, 2(2020-01-1007):1705–1716, 2020.

[105] P.D. Hill. Kernel Estimation of a Distribution Function. *Communications in Statistics-Theory and Methods*, 14(3):605–620, 1985.

[106] A. A. Pesaran. *Tools for designing thermal management of batteries in electric drive vehicles*. National Renewable Energy Laboratory, 2013.

[107] J. Kim, J. Oh, and H. Lee. Review on battery thermal management system for electric vehicles. *Applied thermal engineering*, 149:192–212, 2019.

[108] A. Shirazi, J. Ceberio, and J. A. Lozano. Spacecraft trajectory optimization: A review of models, objectives, approaches and solutions. *Progress in Aerospace Sciences*, 102:76–98, 2018.

[109] F. Mensing, R. Trigui, and E. Bideaux. Vehicle trajectory optimization for application in eco-driving. In *2011 IEEE vehicle power and propulsion conference*, pages 1–6. IEEE, 2011.

[110] S. Li, C. Gu, X. Zeng, P. Zhao, X. Pei, and S. Cheng. Vehicle-to-grid management for multi-time scale grid power balancing. *Energy*, 234:121201, 2021.

[111] R. Bertram and J. E. Rubin. Multi-timescale systems and fast-slow analysis. *Mathematical biosciences*, 287:105–121, 2017.

[112] A. Kargarian, G. Hug, and J. Mohammadi. A multi-time scale co-optimization method for sizing of energy storage and fast-ramping generation. *IEEE Transactions on Sustainable Energy*, 7(4):1351–1361, 2016.

[113] H. Li, D. Chen, X. Gao, X. Wang, Q. Han, and C. Wu. Fast-slow dynamics of a hydropower generation system with multi-time scales. *Mechanical Systems and Signal Processing*, 110:458–468, 2018.